MASTERARBEIT / MASTER'S THESIS

Titel der Masterarbeit / Title of the Master's Thesis

„Self-Energy Diagrammatic Quantum Monte Carlo Methods for the Fröhlich Polaron“

verfasst von / submitted by

Samuel Recker, BSc

angestrebter akademischer Grad / in partial fulfilment of the requirements for the degree of

Master of Science (MSc)

Wien, 2022 / Vienna, 2022

Studienkennzahl lt. Studienblatt / degree programme code as it appears on the student record sheet:	UA 066 876
Studienrichtung lt. Studienblatt / degree programme as it appears on the student record sheet:	Masterstudium Physik
Betreut von / Supervisor:	Univ.-Prof. Dr.techn. Cesare Franchini
Mitbetreut von / Co-Supervisor:	

Abstract

In this thesis, the harmonic Fröhlich polaron is investigated using a computational algorithm called Diagrammatic (Quantum) Monte Carlo (DQMC/DMC). We develop an algorithm that is mostly based on work by [30], [24] and [29], in which A. S. Mishenko, N.S. Prokof'ev, A. Sakamoto and B. V. Svistunov demonstrate the ability to calculate properties of the three-dimensional Fröhlich polaron within the DMC framework. The goal of this thesis is to reproduce these results and provide additional input for the self-energy DMC approach.

The reader is not presumed to be an expert in polaron physics and quantum field theory. Therefore, the first chapter introduces the Fröhlich Hamiltonian with its approximations. Furthermore, the Green's function formalism and Wick's theorem are provided as effective tools for calculating the diagrammatic expansion of the Green's function. The theory behind MC and DMC is studied, where the focus is primarily on detailed derivations. We then perform the sampling of the series of Feynman diagrams for the proper one-electron self-energy with a self-written `C++` program. The results obtained from the calculations are presented and discussed before an outlook on future work is provided.

The results reveal the practicality of DMC calculations and coincide with previous work for the most part. The limitations of the shown work manifest in particular at high coupling strengths. Future work may build upon a more general theory of the Hamiltonian or improve the algorithm in terms of performance. This includes considering anharmonic terms in the Fröhlich Hamiltonian, simulating the one-electron-N-phonon Green's function or implementing bold DMC.

Zusammenfassung

In dieser Arbeit wird das harmonische Fröhlich-Polaron mit einer Methode namens Diagrammatic (Quantum) Monte Carlo (DQMC/DMC) untersucht. Der entwickelte Algorithmus baut hauptsächlich auf Arbeiten von [30], [24] und [29] auf, in denen A. S. Mishenko, N. S. Prokof'ev, A. Sakamoto und B. V. Svistunov die Fähigkeit demonstrieren, Eigenschaften des dreidimensionalen Fröhlich-Polaron innerhalb des DMC-Frameworks zu berechnen. Das Ziel dieser Arbeit ist es, diese Ergebnisse zu reproduzieren und zusätzlichen Ideen für den Selbstenergie-DMC-Ansatz zu liefern.

Es wird nicht vorausgesetzt, dass der Leser ein Experte in Polaronenphysik und Quantenfeldtheorie ist. Daher stellt das erste Kapitel Fröhlich's Hamilton-Operator mit seinen Näherungen vor. Darüber hinaus werden der Formalismus der Greenschen Funktion und das Wick-Theorem als effektive Werkzeuge zur Berechnung der diagrammatischen Entwicklung der Greenschen Funktion bereitgestellt. Die Theorie hinter MC und DMC wird dargelegt, wobei der Fokus vor allem auf detaillierten Herleitungen liegt. Anschließend führen wir die Berechnung der Ein-Elektronen-Selbstenergie mit einem selbstgeschriebenen `C++`-Programm durch. Wir präsentieren und diskutieren die Ergebnisse der Berechnungen, bevor wir einen Ausblick über etwaige zukünftige Arbeit geben.

Die Ergebnisse zeigen die Praktikabilität von DMC-Berechnungen und stimmen größtenteils mit früheren Arbeiten überein. Die Limitationen der gezeigten Arbeit—insbesondere im harmonischen Bereich und ohne Berücksichtigung externer Phononen—manifestieren sich insbesondere in hohen Kopplungsstärken. Zukünftige Arbeiten können auf einer allgemeineren Theorie anharmonischer Versionen des Hamilton-Operators aufbauen, um diese Annäherungen zu überwinden und genauere Ergebnisse zu liefern.

Acknowledgements

Foremost, I would like to thank Univ.-Prof. Dr.techn. Cesare Franchini for the opportunity to take on this project and giving me enough time and resources to see it through until completion.

Furthermore, I want to express my immense gratitude to my co-supervisor Thomas Hahn for the patience, guidence and hours of remote debugging sessions. Without his expertise in the subject, this thesis would have taken much longer to complete. He always motivated me, was very supportive and helped me out when I lost track of the path I was on.

Contents

List of Figures

List of Algorithms

Chapter 1

Polaron Physics

1.1 Quantum Field Theory

1.1.1 First Quantization

Through the first quantization, the classical treatment of physical systems is translated into the language of quantum mechanics. Albeit, the framework is semiclassical, as the environment around the object of interest is still viewed in a classical sense. Physical observables, such as position and momentum, are converted into operator observables. Operators act upon the state of a system $|\psi\rangle$ which can be projected onto the position basis $|\mathbf{x}\rangle$ and be represented as a wave function $\psi(\mathbf{x}, t)$. Born linked the probability density of the state $|\psi\rangle$ to the integral of the absolute squared value of the complex wavefunction [6]

$$\int \mathrm{d}\mathbf{x}\, \psi^*(\mathbf{x}, t)\psi(\mathbf{x}, t) = 1\,. \tag{1.1}$$

With this interpretation, we can calculate the time-dependent mean value of a physical quantity $O(t)$

$$\begin{aligned}
\langle \hat{O}(t)\rangle &= \int \mathrm{d}\mathbf{x}\, \psi^*(\mathbf{x}, t)\hat{O}\psi(\mathbf{x}, t) && (1.2)\\
&= \int \mathrm{d}\mathbf{x}\, \langle\psi(t)|\mathbf{x}\rangle\, \hat{O}\, \langle\mathbf{x}|\psi(t)\rangle && (1.3)\\
&= \langle\psi(t)|\hat{O}|\psi(t)\rangle \left(\int \mathrm{d}\mathbf{x}\, |\mathbf{x}\rangle\, \langle\mathbf{x}|\right) && (1.4)\\
&= \langle\psi(t)|\hat{O}|\psi(t)\rangle && (1.5)
\end{aligned}$$

where we have used the completeness relation of the position basis set $\int \mathrm{d}\mathbf{x}\, |\mathbf{x}\rangle\, \langle\mathbf{x}| = \hat{1}$. Writing out the variance of the observable $\hat{O}$

$$\langle \hat{O}^2\rangle - \langle \hat{O}\rangle^2 = \int \mathrm{d}\mathbf{x}\, \psi^*(\mathbf{x}, t)\hat{O}\hat{O}\psi(\mathbf{x}, t) - \left(\int \mathrm{d}\mathbf{x}\, \psi^*(\mathbf{x}, t)\hat{O}\psi(\mathbf{x}, t)\right)^2 \tag{1.6}$$

and assuming that ψ are eigenfunctions of $\hat{O}$, the two terms cancel and we find that there actually exists a unique value for $\langle O \rangle$ [25]. Another way to evaluate the expectation value of $\langle \hat{O} \rangle$ is by means of a density matrix $\hat{\rho} = \sum_i p_i \left| i \right\rangle \left\langle i \right|$

$$\langle \hat{O} \rangle = \sum_i p_i \left\langle i | \hat{O} | i \right\rangle \tag{1.7}$$

$$= \mathrm{Tr} \left[\hat{O} \hat{\rho} \right] \tag{1.8}$$

Let's look at the thermodynamic equilibrium. We have an atomic Hamiltonian $\hat{H}$ with energies ε_i at temperature T. With the probabilities

$$p_i = \frac{\exp\left(-\varepsilon_i / k_B T\right)}{Z} \tag{1.9}$$

acting as the Boltzmann factors the grand canonical ensemble can be expressed as

$$\hat{\rho} = \frac{\exp\left(-\hat{H}/k_B T\right)}{\mathrm{Tr}\left[\exp\left(-\hat{H}/k_B T\right)\right]} \,. \tag{1.10}$$

When working with a many-body system one needs to pay attention to the indistinguishability of particles. We must keep in mind the symmetric/anti-symmetric nature of bosonic/fermionic wavefunctions. Considering a one-particle Hamiltonian

$$\hat{H}_0 \left| \psi_i \right\rangle = \varepsilon_i \left| \psi_i \right\rangle \tag{1.11}$$

and N indistinguishable particles we have

$$\Psi = \sqrt{\frac{1}{N! \prod_{i=0}^{\infty} n_i!}} \sum_P \zeta^{(1-P)/2} \left| \psi_{P[1]} \right\rangle \otimes \left| \psi_{P[2]} \right\rangle \otimes \ldots \otimes \left| \psi_{P[N]} \right\rangle \tag{1.12}$$

where

$$\zeta = \begin{cases} -1 & \text{for fermions} \\ 1 & \text{for bosons} \end{cases} \tag{1.13}$$

and n_i refers to the number of particles in state i. Readers familiar with condensed matter physics might notice the connection between Eq. 1.12 and Slater's determinant [3] [7]. This framework has essentially one huge limitation. We are not allowed to change N. It would be much less cumbersome to work in a grand canonical picture where N is a free parameter.

1.1.2 Second Quantization

Escaping from the limitations of this language we introduce the *occupation number representation*. We go from explicitly writing all permutations of the states to a more readable notation

$$\left| \{n_k\} \right\rangle \equiv \left| n_1, n_2, \ldots \right\rangle \tag{1.14}$$

where n_k represents the occupation number of state k. For example $|1,3,3\rangle$ translates to $|1,0,2\rangle$. To free ourselves from the limitation of a fixed number of particles, we switch to Fock space

$$\mathcal{F} = \bigoplus_{N=0}^{\infty} \mathcal{F}^N = \mathbb{C} \oplus H \oplus (H \otimes H) \oplus \dots \tag{1.15}$$

where we also for the first time have a *vacuum* space $\mathcal{F}^0$ [2]. Fock space is the direct sum of tensor products of single-particle Hilbert spaces. This means that we are able to combine and connect all possible states of a varying number of particles into one space.

To traverse between products of Hilbert spaces we define creation $\hat{a}_i^\dagger$ and annihilation $\hat{a}_i$ operators, in which we "hide" the restrictions we have encountered. Here we must take care of the different natures of bosons and fermions. We cannot create one set of relations for both of them. For bosons, we have

$$[\hat{b}_i, \hat{b}_j^\dagger] = \delta_{ij} \tag{1.16}$$

$$[\hat{b}_i^\dagger, \hat{b}_j^\dagger] = [\hat{b}_i, \hat{b}_j] = 0 \tag{1.17}$$

$$\hat{b}_i \left|n_1, \dots, n_i, \dots\right\rangle = \sqrt{n_i} \left|n_1, \dots, n_i - 1, \dots\right\rangle \tag{1.18}$$

$$\hat{b}_i^\dagger \left|n_1, \dots, n_i, \dots\right\rangle = \sqrt{n_i + 1} \left|n_1, \dots, n_i + 1, \dots\right\rangle \tag{1.19}$$

Since fermionic systems must not violate the Pauli exclusion principle and interchanging the order of a fermionic wavefunction changes its sign, this leads to

$$\{\hat{a}_i, \hat{a}_j^\dagger\} = \delta_{ij} \tag{1.20}$$

$$\{\hat{a}_i^\dagger, \hat{a}_j^\dagger\} = \{\hat{a}_i, \hat{a}_j\} = 0 \tag{1.21}$$

$$\hat{a}_i \left|n_1, \dots, n_i, \dots\right\rangle = \begin{cases} (-1)^{n_1 + \dots + n_{i-1}} \left|n_1, \dots, n_i - 1, \dots\right\rangle & \text{if } n_i = 1 \\ 0 & \text{if } n_i = 0 \end{cases} \tag{1.22}$$

$$\hat{a}_i^\dagger \left|n_1, \dots, n_i, \dots\right\rangle = \begin{cases} (-1)^{n_1 + \dots + n_{i-1}} \left|n_1, \dots, n_i + 1, \dots\right\rangle & \text{if } n_i = 0 \\ 0 & \text{if } n_i = 1 \end{cases} \tag{1.23}$$

where we have used the anticommutator $\{a, b\} = ab + ba$ to satisfy the symmetry constraints of fermionic wavefunctions. The interested reader might notice that the commutation relations only hold for an orthonormal and complete basis of single-particle wavefunctions

$$[\hat{b}_j, \hat{b}_k^\dagger] = \hat{b}_j \hat{b}_k^\dagger - \hat{b}_k^\dagger \hat{b}_j = \langle \psi_j | \psi_k \rangle \ , \tag{1.24}$$

though this originates from how the N-particle wavefunction and Fock space were constructed, not from the occupation number representation or 2nd quantization itself [27]. Observe that by merely repeatedly using the creation operator on the vacuum state $|0\rangle$, we can essentially create every desirable state in $\mathcal{F}$

$$\left|n_1, n_2, \dots\right\rangle = \prod_i \frac{1}{\sqrt{n_i!}} (a_i^\dagger)^{n_i} \left|0\right\rangle \ . \tag{1.25}$$

Single-particle operator observables can directly be translated to their second quantized form [7]. If we take

$$\langle\psi|\hat{O}|\psi\rangle = \int \mathrm{d}\mathbf{x}\, \psi^*(\mathbf{x}) O(\mathbf{x}) \psi(\mathbf{x}) \tag{1.26}$$

and expand ψ in single-particle eigenstates

$$\psi(\mathbf{x}) = \sum_i \psi_i(\mathbf{x}) a_i^\dagger |0\rangle \tag{1.27}$$

we can rewrite the operator $\hat{O}$ in its second quantized form as

$$\hat{O} = \sum_{i,j} a_i^\dagger O_{i,j} a_j \tag{1.28}$$

where

$$O_{i,j} = \langle i|\hat{O}|j\rangle = \int \mathrm{d}\mathbf{x}\, \psi_i^*(\mathbf{x}) O(\mathbf{x}) \psi_j(\mathbf{x})\,. \tag{1.29}$$

is the first-quantized operator, $a_i^\dagger$ and a_j are the creation and annihilation operators of single-particle states described by the quantum numbers i and j. Analogously, two-particle interaction $\hat{V}$ [26] results in

$$\hat{V} = \sum_{i,j,k,l} a_i^\dagger a_j^\dagger V_{i,j,k,l} a_l a_k \tag{1.30}$$

$$V_{i,j,k,l} = \frac{1}{2} \int \mathrm{d}\mathbf{x} \int \mathrm{d}\mathbf{x}'\, \psi_i^*(\mathbf{x}) \psi_j^*(\mathbf{x}') V(|\mathbf{x} - \mathbf{x}'|) \psi_k(\mathbf{x}') \psi_l(\mathbf{x})\,. \tag{1.31}$$

Paying attention to the order of indices and coordinates of the wavefunctions is crucial.

One special operator that is still missing is the occupation number operator [26]

$$\hat{n}_i = \hat{a}_i^\dagger \hat{a}_i \tag{1.32}$$

which has eigenvalues n_i, the number of particles occupying state i,

$$\hat{n}_i |n_1, \ldots, n_i, \ldots\rangle = n_i |n_1, \ldots, n_i, \ldots\rangle\,. \tag{1.33}$$

Following the principles discussed above the system of interest is now represented as a quantum field, where the position is not an operator anymore as in the first quantization formalism, but rather a free parameter, similar to the time. As a final step in developing the second quantization technique, we introduce so-called *field operators*. One advantage of this is the removal of dependence upon the choice of basis. Assuming a complete set of single-particle quantum states ψ_k we define the field operators

$$\hat{\psi}(\mathbf{r}) = \sum_k \hat{a}_k \psi_k(\mathbf{r}) \tag{1.34}$$

$$\hat{\psi}^\dagger(\mathbf{r}) = \sum_k \hat{a}_k^\dagger \psi_k^*(\mathbf{r}) \tag{1.35}$$

which annihilate/create a particle at point $\mathbf{r}$, respectively [20] [18]. Analogously to ladder operators, field operators also obey certain commutation rules. For bosons we have

$$[\hat{\psi}(\mathbf{r}), \hat{\psi}^\dagger(\mathbf{r}')] = \delta(\mathbf{r} - \mathbf{r}') \tag{1.36}$$

$$[\hat{\psi}(\mathbf{r}), \hat{\psi}(\mathbf{r}')] = [\hat{\psi}^\dagger(\mathbf{r}), \hat{\psi}^\dagger(\mathbf{r}')] = 0 \tag{1.37}$$

while the fermionic commutation rules are

$$\{\hat{\psi}(\mathbf{r}), \hat{\psi}^\dagger(\mathbf{r}')\} = \delta(\mathbf{r} - \mathbf{r}') \tag{1.38}$$

$$\{\hat{\psi}(\mathbf{r}), \hat{\psi}(\mathbf{r}')\} = \{\hat{\psi}^\dagger(\mathbf{r}), \hat{\psi}^\dagger(\mathbf{r}')\} = 0 \tag{1.39}$$

1.2 Polarons

Polarons are quasiparticles that are used in condensed matter physics to describe the interaction between an electron (hole; hereafter, only electrons are mentioned, but holes may be implicitly substituted) and ions. In an ideal lattice, the ions of a crystal remain in their equilibrium positions denoted by the lattice points of the crystal as seen in Fig. 1.1a. In real systems, the ions never lie exactly on, but rather

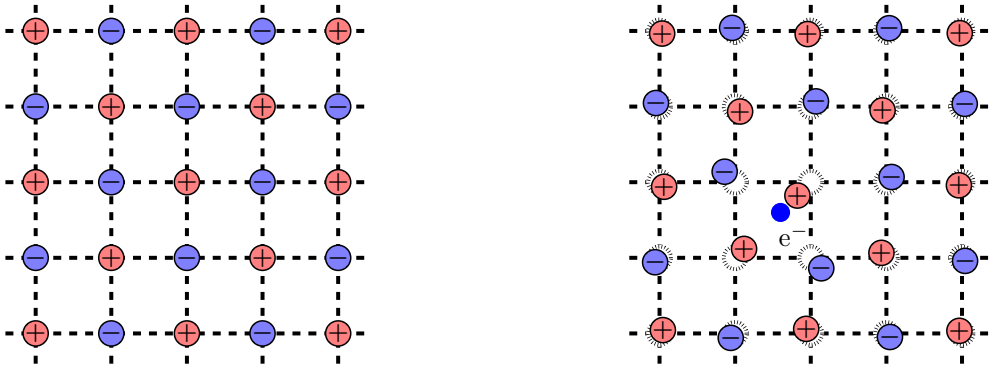

(a) Lattice equilibrium; all atoms reside on their respective lattice points.

(b) Artistic representation of lattice distortion due to the insertion of an electron.

Figure 1.1: Illustration of a polaron in an ionic crystal, e.g. Na^+Cl^-: The positive Na ions are attracted to the free electron while the negatively charged Cl ions are repelled.

oscillate around their designated lattice point. This is described by introducing the term *phonon* to refer to the ionic displacements inside the crystal. Electrons can couple to and interact with these phonons.

Adding a charge, e.g. an electron, to the system shifts the positions of the ions according to their charge, as can be seen in Fig. 1.1b. The deformation of the lattice around the electron can be viewed as a virtual phonon cloud by which the electron is dressed. Traveling through the medium, the electron is followed by these

virtual phonons. This collective effect is what is known as a polaron [14] [1]. The deformation of the lattice has two significant consequences:

- Electrons scatter due to their interaction with the surrounding system, which in turn causes electrical resistance.
- The electron's properties change.

The interaction between the electron and the ions is characterized by the type of phonons to which the electron is coupled, the coupling strength and the dimensionality of the observed system. Depending on the lattice constant and these parameters, lattice polarons may be classified as *small* or *large*. The size r_p of the polaron describes the spatial extent around the electron in which lattice distortion is *not* negligible. For small polarons, it holds that the lattice constant $a \approx r_p$, which means that the discreteness of the lattice has to be considered when deriving the Hamiltonian of the system, e.g. for the Holstein model [16]. Large polarons exhibit sizes far beyond the lattice constant $r_p \gg a$, which in turn enables the continuous treatment of the system. A prominent example, which is also the model of interest of this thesis, is the Fröhlich Hamiltonian [9].

If the coupling strength is so high that the electron is not able to move freely anymore, we speak of Landau's concept of self-trapping of electrons in a perfect lattice. [4].

1.3 Fröhlich Hamiltonian

The derivation of the Fröhlich Hamiltonian follows a similar ansatz to Pekar's polaron [28]. It describes a slow-moving, free electron in the lower edge of the conduction band placed in a three-dimensional, ionic, cubic crystal lattice, without any interaction with other electrons. The ionic crystal is approximated by a continuous, isotropic, dielectric medium. The polarization is – in contrast to Pekar's polaron – now treated in a completely quantum mechanical picture. Using second quantization we will make use of phonons to describe the ionic displacement. While considering the original derivation by Fröhlich [9], the following will also rely upon work by Haken [14].

The polaron radius of electrons is inversely proportional to their energy. The influence of electrons with sufficiently low energy therefore may span many lattice sites. In this limit, the electronic wavefunction only differs little between lattice points, which allows treating the polarization $\mathbf{P}(\mathbf{r})$ of the crystal in a continuous manner. Classical electrostatics (in cgs units) shows the dependence

$$\mathbf{D}(\mathbf{r}) = \mathbf{E}(\mathbf{r}) + 4\pi\mathbf{P}(\mathbf{r})\,, \tag{1.40}$$

$$\mathbf{D}(\mathbf{r}) = \varepsilon(\omega)\mathbf{E}(\mathbf{r}) \tag{1.41}$$

with the absolute permittivity ε. Since we assumed a linear, homogeneous, isotropic

medium we have the relation

$$\mathbf{P}(\mathbf{r}) = \frac{1}{4\pi}\left(1 - \frac{1}{\varepsilon(\omega)}\right)\mathbf{D}(\mathbf{r}) \tag{1.42}$$

between the electric field $\mathbf{E}$, the polarization field $\mathbf{P}(\mathbf{r})$ and the electric displacement field $\mathbf{D}$. In the static limit, the polarization has enough time to fully relax. Thus, we have

$$\mathbf{P}_t(\mathbf{r}) = \frac{1}{4\pi}\left(1 - \frac{1}{\varepsilon_0}\right)\mathbf{D}(\mathbf{r}) \tag{1.43}$$

where $\mathbf{P}_t(\mathbf{r})$ labels the total polarization. A more detailed treatment can be found in Haken [14]. Assuming a slow electron, the interaction of its magnetic field with the polarization field is negligible, such that we propose

$$(\nabla \times \mathbf{P})(\mathbf{r}) = 0 \tag{1.44}$$

and therefore, $\mathbf{D}$ is only dependent on the single free electron. The acoustic phonons coupling to the ions are moving in phase. For these phonon branches $\omega(\mathbf{q}) \to 0$ as $\mathbf{q} \to 0$, which corresponds to the equivalency of phonon motion and translation of the whole crystal. These phonons do not contribute to the polarization field and thus, only optical phonons are left to examine. The influence of the transverse optical (TO) modes upon the ions are negligible, since they are perpendicular to $\mathbf{q}$ and, thus, do not lead to any polarization along $\mathbf{q}$, which we will see in Eq. 1.72. This leaves longitudinal optical (LO) modes as the sole source of polarization in the Fröhlich polaron [19]. The total polarization

$$\mathbf{P}_t(\mathbf{r}) = \mathbf{P}_0(\mathbf{r}) + \mathbf{P}_{\text{ir}}(\mathbf{r}) \tag{1.45}$$

is composed of both the high-energy polarization of the electron cloud of the ions $\mathbf{P}_0(\mathbf{r})$ and the low-energy polarization due to the ionic displacement of the lattice $\mathbf{P}_{\text{ir}}(\mathbf{r})$. Though, we are only interested in the response from the lattice. Imagine turning on the electric field and letting the polarization develop almost statically. Now, after instantaneously switching off the field, only the electrons can respond quickly enough, which leaves us with the polarization of the electron cloud

$$\mathbf{P}_0(\mathbf{r}) = \frac{1}{4\pi}\left(1 - \frac{1}{\varepsilon_\infty}\right)\mathbf{D}(\mathbf{r}) \tag{1.46}$$

where ε_∞ is the high frequency dielectric constant. Now the polarization due to the ionic displacement can be expressed as

$$\mathbf{P}_{\text{ir}}(\mathbf{r}) = \frac{1}{4\pi}\left(\frac{1}{\varepsilon_\infty} - \frac{1}{\varepsilon_0}\right)\mathbf{D}(\mathbf{r}) = \frac{1}{4\pi\bar{\varepsilon}}\mathbf{D}(\mathbf{r})\,. \tag{1.47}$$

From here on we drop the subscript and write $\mathbf{P} = \mathbf{P}_{\text{ir}}$. First, before deriving the equations of motion, a recapitulation of the connection between polarization and

dipoles are in order. A dipole has a moment $\mathbf{q}$, mass m and an eigenfrequency ω. Its energy is therefore given by

$$\frac{m}{2}\left(\mathbf{q}^2 + \omega^2\mathbf{q}^2\right) . \tag{1.48}$$

Now we perform the transition from the real discrete system of a crystal to a continuous one while assuming that the dipoles themselves do not interact with each other. Furthermore, we substitute the dipole moment $\mathbf{q}$ with the polarization density $\mathbf{P}(\mathbf{r})$ and the discrete mass m with a mass density ρ:

$$e^*\mathbf{q}_k \to \mathbf{P}(\mathbf{r}) \tag{1.49}$$

$$m \to \rho \mathrm{d}\mathbf{r} \tag{1.50}$$

The total energy of the oscillating polarization field can now be expressed in terms of the kinetic energy T and potential energy V

$$E_{pol} = T_{pol} + V_{pol} = \int \mathrm{d}\mathbf{r}\, \frac{\gamma}{2}\dot{\mathbf{P}}^2(\mathbf{r}) + \int \mathrm{d}\mathbf{r}\, \frac{\gamma}{2}\omega^2\mathbf{P}^2(\mathbf{r}) \tag{1.51}$$

where we introduced a new constant γ defined by

$$\frac{m}{e^{*2}} = \gamma \mathrm{d}\mathbf{r} . \tag{1.52}$$

To investigate this new parameter, we look at the interaction energy between an electron with charge ρ at $\mathbf{r}$ and a dipole moment $\mathbf{P}$ at $\mathbf{r}'$

$$H_{e-d} = \rho\frac{(\mathbf{r}-\mathbf{r}')}{|\mathbf{r}-\mathbf{r}'|^3}\mathbf{P} \tag{1.53}$$

which converts to

$$H_{e-d} = \int \mathrm{d}\mathbf{r} \int \mathrm{d}\mathbf{r}'\, \rho(\mathbf{r})\frac{(\mathbf{r}-\mathbf{r}')}{|\mathbf{r}-\mathbf{r}'|^3}\mathbf{P}(\mathbf{r}') \tag{1.54}$$

for the continuous case of a polarization field $\mathbf{P}(\mathbf{r})$ and a charge density $\rho(\mathbf{r})$. To study the equations of motion of polarization oscillations, we assume the charge density to be static. The Lagrangian results in

$$\mathcal{L} = T_{pol} - V_{pol} - H_{e-d} . \tag{1.55}$$

To obtain the equations of motion we use the well-known Euler-Lagrange equation

$$\frac{\delta\mathcal{L}(\mathbf{P}(\mathbf{r}), \dot{\mathbf{P}}(\mathbf{r}), \mathbf{r})}{\delta\mathbf{P}(\mathbf{r}')} - \frac{\mathrm{d}}{\mathrm{d}t}\frac{\delta\mathcal{L}(\mathbf{P}(\mathbf{r}), \dot{\mathbf{P}}(\mathbf{r}), \mathbf{r})}{\delta\dot{\mathbf{P}}(\mathbf{r}')} = 0 \tag{1.56}$$

where $k \in \{x, y, z\}$. Carrying out the functional derivatives

$$\frac{\delta\mathcal{L}}{\delta\mathbf{P}(\mathbf{r}')} = \int \mathrm{d}\mathbf{r}\left[\frac{\gamma}{2}\left(\cancelto{0}{\frac{\delta\dot{\mathbf{P}}^2}{\delta\mathbf{P}}(\mathbf{r})} - \omega^2\frac{\delta\mathbf{P}^2}{\delta\mathbf{P}}(\mathbf{r})\right) - \rho(\mathbf{r})\int \mathrm{d}\mathbf{r}'\,\frac{\mathbf{r}-\mathbf{r}'}{|\mathbf{r}-\mathbf{r}'|^3}\frac{\delta\mathbf{P}}{\delta\mathbf{P}}(\mathbf{r}')\right] \tag{1.57}$$

$$= -\gamma\omega^2\mathbf{P}(\mathbf{r}') - \int \mathrm{d}\mathbf{r}\,\rho(\mathbf{r})\frac{\mathbf{r}-\mathbf{r}'}{|\mathbf{r}-\mathbf{r}'|^3} \tag{1.58}$$

$$= -\gamma\omega^2\mathbf{P}(\mathbf{r}') + \mathbf{D}(\mathbf{r}') \tag{1.59}$$

$$\frac{\mathrm{d}}{\mathrm{d}t}\frac{\delta\mathcal{L}}{\delta\dot{\mathbf{P}}(\mathbf{r}')} = \frac{\mathrm{d}}{\mathrm{d}t}\left(\int \mathrm{d}\mathbf{r}\left[\frac{\gamma}{2}\left(\frac{\delta\dot{\mathbf{P}}^2}{\delta\dot{\mathbf{P}}}(\mathbf{r}) - \omega^2\cancelto{0}{\frac{\delta\mathbf{P}^2}{\delta\mathbf{P}}(\mathbf{r})}\right) - \right.\right. \tag{1.60}$$

$$\left.\left. - \rho(\mathbf{r})\int \mathrm{d}\mathbf{r}'\,\frac{\mathbf{r}-\mathbf{r}'}{|\mathbf{r}-\mathbf{r}'|^3}\cancelto{0}{\frac{\delta\mathbf{P}}{\delta\dot{\mathbf{P}}}(\mathbf{r}')}\right]\right)$$

$$= \gamma\frac{\mathrm{d}}{\mathrm{d}t}\dot{\mathbf{P}}(\mathbf{r}') \tag{1.61}$$

$$= \gamma\ddot{\mathbf{P}}(\mathbf{r}') \tag{1.62}$$

one arrives at

$$\gamma\left(\ddot{\mathbf{P}}(\mathbf{r}') + \omega^2\mathbf{P}(\mathbf{r}')\right) = \mathbf{D}(\mathbf{r}') \tag{1.63}$$

To find γ we specialize Eq. 1.63 for the static case where $\ddot{\mathbf{P}} = 0$:

$$\gamma\omega^2\mathbf{P}(\mathbf{r}') = \mathbf{D}(\mathbf{r}')\,. \tag{1.64}$$

Comparing Eq. 1.47 and Eq. 1.64 we can finalize the derivation of the equations of motion for the polarization field since the constant

$$\gamma = \frac{4\pi}{\omega^2}\left(\frac{1}{\varepsilon_\infty} - \frac{1}{\varepsilon_0}\right)^{-1} = \frac{4\pi}{\omega^2}\bar{\varepsilon} \tag{1.65}$$

is now defined. To gain the full Hamiltonian, we will also need to include the kinetic energy of the electrons. As previously mentioned, the electrons are at the lower edge of the conduction band and only the infrared (low-energy) interaction with the ions is of importance. This allows the application of the *bare effective mass approximation*. *Bare* because it is only the effective mass m^* of the electron caused by the interaction with core electrons, not the effective mass of the polaron [19]. Now, we will be splitting from Fröhlich's original derivation in the sense that we will not depend on the electron's position, but rather handle the kinetic energy term using its wavefunction $\psi(\mathbf{r})$. The kinetic energy term of the electron then becomes

$$T_{el} = \int \mathrm{d}\mathbf{r}\,\psi^\dagger(\mathbf{r})\left(-\frac{\hbar^2}{2m^*}\nabla\right)\psi(\mathbf{r}) \tag{1.66}$$

While it is not valid to put the charge density and the wavefunction into a relationship of equivalency, the former can be expressed by the latter in an operational way – i.e. as an *entity that acts on other objects* –

$$\rho(\mathbf{r}) = e\,|\psi(\mathbf{r})|^2\,, \tag{1.67}$$

so that for the interaction term we have

$$H_{e-d} = \int \mathrm{d}\mathbf{r}\, e\,|\psi(\mathbf{r})|^2 \int \mathrm{d}\mathbf{r}'\, \frac{\mathbf{r}-\mathbf{r}'}{|\mathbf{r}-\mathbf{r}'|^3}\mathbf{P}(\mathbf{r}') \tag{1.68}$$

$$= \int \mathrm{d}\mathbf{r}\, e\,|\psi(\mathbf{r})|^2 \int \mathrm{d}\mathbf{r}'\, \mathbf{P}(\mathbf{r}')\nabla_{\mathbf{r}'}\,|\mathbf{r}-\mathbf{r}'|^{-1} \tag{1.69}$$

$$= -\int \mathrm{d}\mathbf{r} \int \mathrm{d}\mathbf{r}'\, |\psi(\mathbf{r})|^2 \frac{e}{|\mathbf{r}-\mathbf{r}'|}\boldsymbol{\nabla}_{\mathbf{r}'}\cdot\mathbf{P}(\mathbf{r}') \tag{1.70}$$

where we have rewritten the potential in terms of a gradient and then performed integration by parts. Now if we calculate the conjugate momentum

$$\Pi(\mathbf{r}) = \frac{\delta\mathcal{L}\left(\mathbf{P}(\mathbf{r}),\dot{\mathbf{P}}(\mathbf{r}),\mathbf{r}\right)}{\delta\dot{\mathbf{P}}} = \gamma\dot{\mathbf{P}}(\mathbf{r}) \tag{1.71}$$

we can express the Hamiltonian as a sum of the electronic kinetic energy Eq. 1.66, the energy of the oscillating polarization field Eq. 1.51 and the interaction term Eq. 1.70:

$$\begin{aligned} H = &\int \mathrm{d}\mathbf{r}\,\psi^\dagger(\mathbf{r})\left(-\frac{\hbar^2}{2m^*}\nabla\right)\psi(\mathbf{r}) + \int \mathrm{d}\mathbf{r}\,\left(\frac{1}{2\gamma}\mathbf{\Pi}^2(\mathbf{r}) + \frac{\gamma\omega^2}{2}\mathbf{P}^2(\mathbf{r})\right) - \\ &- \int \mathrm{d}\mathbf{r} \int \mathrm{d}\mathbf{r}'\, |\psi(\mathbf{r})|^2 \frac{e}{|\mathbf{r}-\mathbf{r}'|}\boldsymbol{\nabla}_{\mathbf{r}'}\cdot\mathbf{P}(\mathbf{r}') \end{aligned} \tag{1.72}$$

As pointed out at the beginning of the derivation, we now see that only longitudinal phonons factor into the Hamiltonian since the rotation of the divergence of a vector field is null. Now, by expanding $\mathbf{P}(\mathbf{r}')$ and ψ in terms of plane waves

$$\mathbf{P}(\mathbf{r}') = \frac{1}{\sqrt{V}}\sum_{\mathbf{q}}\sqrt{\frac{\hbar}{2\gamma\omega}}\frac{\mathbf{q}}{q}e^{i\mathbf{q}\mathbf{r}'}\left(b_{\mathbf{q}} - b^\dagger_{-\mathbf{q}}\right) \tag{1.73}$$

$$\psi(\mathbf{r}) = \frac{1}{\sqrt{V}}\sum_{\mathbf{k}} a_{\mathbf{k}}e^{i\mathbf{k}\mathbf{r}} \tag{1.74}$$

the final version of the Hamiltonian is established as

$$\begin{aligned} H = &\sum_{\mathbf{k}}\frac{\hbar^2k^2}{2m^*}a^\dagger_{\mathbf{k}}a_{\mathbf{k}} + \sum_{\mathbf{q}}\hbar\omega b^\dagger_{\mathbf{q}}b_{\mathbf{q}} + \\ &+ \hbar\sum_{\mathbf{q},\mathbf{k}}\left(g_{\mathbf{q}}b_{\mathbf{q}}a^\dagger_{\mathbf{k}+\mathbf{q}}a_{\mathbf{k}} - g^*_{\mathbf{q}}b^\dagger_{-\mathbf{q}}a^\dagger_{\mathbf{k}-\mathbf{q}}a_{\mathbf{k}}\right) \end{aligned} \tag{1.75}$$

with the coupling constant $g_{\mathbf{q}}$

$$g_{\mathbf{q}} = -\frac{4\pi i}{\hbar q}\sqrt{\frac{e^2\hbar}{2\gamma\omega V}}\,. \tag{1.76}$$

To get to Eq. 1.75 from Eq. 1.72 the plane wave expansions were inserted, the integral evaluated and – since they commute – creation and annihilation operators of bosons and fermions rearranged. Until Eq. 1.74 the derivation only contains classical terms. It has to be noted that the representation of $g_{\mathbf{q}}$ is specific to this case.

1.4 Interaction Picture

Besides the Schrödinger and the Heisenberg picture, there is also the interaction picture that is heavily used in quantum field theory. While the former two rely upon putting the time dependence solely into either the states or the operators, the interaction picture combines these views and lets both the state vector and the operators carry part of the time dependence [7]. This is done by splitting the full Hamiltonian into two parts

$$\hat{H} = \hat{H}_0 + \hat{H}_1 \tag{1.77}$$

$$\hat{H}_0 = \sum_{\mathbf{k}} (\varepsilon(\mathbf{k}) - \mu) a^\dagger_{\mathbf{k}} a_{\mathbf{k}} + \sum_{\mathbf{q}} \omega(\mathbf{q}) b^\dagger_{\mathbf{q}} b_{\mathbf{q}} \tag{1.78}$$

$$\hat{H}_1 = \sum_{\mathbf{q},\mathbf{k}} \frac{g(\mathbf{k},\mathbf{q})}{\sqrt{N}} \left(b_{\mathbf{q}} + b^\dagger_{-\mathbf{q}} \right) a^\dagger_{\mathbf{k}+\mathbf{q}} a_{\mathbf{k}} \tag{1.79}$$

where $\hat{H}_0$ is usually chosen to be analytically solvable and all complicated and temporal aspects of the full Hamiltonian are put into $\hat{H}_1$. The chemical potential μ is inserted into the Hamiltonian as a renormalization constant. In Section 1.7 we will see the benefits it brings. From here on forth we will be working in atomic units and therefore set $\hbar = e = 1$. The state vector and operators in the interaction picture are now defined as

$$|\psi_I(\tau)\rangle \equiv e^{\hat{H}_0 \tau} |\psi_S(\tau)\rangle = \hat{U}_0(0,\tau) |\psi_S(\tau)\rangle \tag{1.80}$$

$$\hat{O}_I(\tau) = U_0(0,\tau) \hat{O} U_0(\tau,0) \tag{1.81}$$

where

$$\hat{U}_0(\tau,0) = \hat{U}_0(\tau) \equiv e^{-\hat{H}_0 \tau} \tag{1.82}$$

describes the time evolution operator for the time-independent part of the Hamiltonian $\hat{H}_0$ and we changed to imaginary time $\tau = it$ due to reasons that will be discussed in the next section. The equations of motion in the interaction picture, therefore, take on the following form:

$$-\frac{\partial}{\partial\tau} |\psi_I(\tau)\rangle = -\frac{\partial}{\partial\tau} \hat{U}_0 |\psi_S(\tau)\rangle - \hat{U}_0(\tau) \frac{\partial}{\partial\tau} |\psi_S(\tau)\rangle \tag{1.83}$$

$$= \hat{U}_0(-\hat{H}_0 + \hat{H}) |\psi_S(\tau)\rangle \tag{1.84}$$

$$= \hat{H}_1(\tau) |\psi_I(\tau)\rangle \tag{1.85}$$

where

$$\hat{H}_1(\tau) \equiv U_0(-\tau) \hat{H}_1 U_0(\tau)\,, \tag{1.86}$$

$$\hat{H}_0(\tau) \equiv \hat{H}_0\,. \tag{1.87}$$

Naturally, the time evolution operator takes on the form

$$|\psi_I(\tau)\rangle = \hat{U}(\tau,\tau_0) |\psi_I(\tau_0)\rangle \tag{1.88}$$

which implies that

$$\hat{U}(\tau,\tau) = 1\,. \tag{1.89}$$

As an example we evaluate the interaction picture representation of the ladder operators:

$$\begin{aligned} a_{I,\mathbf{k}}(\tau) &= e^{\hat{H}_0\tau} a_k e^{-\hat{H}_0\tau} \\ &= a_{\mathbf{k}} + [\hat{H}_0, a_{\mathbf{k}}]\tau + \frac{1}{2}[\hat{H}_0,[\hat{H}_0,a_{\mathbf{k}}]]\tau + \dots \\ &= a_{\mathbf{k}} \sum_{n=0}^{\infty} \frac{(-\varepsilon(\mathbf{k})\tau)^n}{n!} \\ &= a_{\mathbf{k}} e^{-\varepsilon(\mathbf{k})\tau} \end{aligned} \tag{1.90}$$

$$a^\dagger_{I,\mathbf{k}}(\tau) = a^\dagger_{\mathbf{k}} e^{\varepsilon(\mathbf{k})\tau} \tag{1.91}$$

$$b_{I,\mathbf{q}}(\tau) = b_{\mathbf{q}} e^{-\omega(q)\tau} \tag{1.92}$$

$$b^\dagger_{I,\mathbf{q}}(\tau) = b^\dagger_{\mathbf{q}} e^{\omega(q)\tau} \tag{1.93}$$

From here on the subscript I—to indicate the interaction picture representation—will be dropped, as we will perform most of the calculation within this picture. Occurrences of operators or state vectors that live in other pictures will be marked as such by explicitly providing the subscript for the Schrödinger (S) or Heisenberg (H) picture.

1.5 Green's function

In quantum field theory, one of the main objects of interest is the single particle *Green's function* $G(\mathbf{x}_2,t_2;\mathbf{x}_1,t_1)$. In simplified terms, it describes the propagation of a particle from one point in space and time $(\mathbf{x}_1,t_1)$ to another $(\mathbf{x}_2,t_2)$. Hence, it is also often referred to as the *propagator* of a particle. Only for few systems analytical solutions exist for the Green's function. However, numerically exact algorithms have been developed. One of them is the diagrammatic Monte Carlo method. Generally speaking, Green's functions are expectation values of time-dependent Heisenberg operators. The single-particle Green's function is defined as

$$iG(\mathbf{x},t;\mathbf{x}',t') = \langle T[\hat{\psi}(\mathbf{x},t)\hat{\psi}^\dagger(\mathbf{x}',t')]\rangle\ , \tag{1.94}$$

where $\langle ...\rangle$ describes averaging over the grand canonical ensemble, i.e. taking the trace of the observable and the density operator. $\hat{T}$ is the time ordering operator, which is defined as

$$\hat{T}\left[\prod_n \hat{\psi}(\mathbf{x}_n,t_n)\right] = (-1)^P \hat{\psi}(\mathbf{x}_1,t_1)\hat{\psi}(\mathbf{x}_2,t_2)\dots\hat{\psi}(\mathbf{x}_N,t_N) \tag{1.95}$$

where P describes the number of commutations of non-commuting states needed to have the times $t_1,\dots t_N$ in descending order – that is $t_1 > t_2 > t_3 \dots > t_N$. Bosonic

ladder/field operators satisfy Eq. 1.17 and Eq. 1.37, which implies $P = 0$. At zero temperature

$$\langle ... \rangle \equiv \frac{\langle \psi_{\mathrm{GS}} | \, ... \, | \psi_{\mathrm{GS}} \rangle}{\langle \psi_{\mathrm{GS}} | \psi_{\mathrm{GS}} \rangle} \,, \tag{1.96}$$

where $|\psi_{\mathrm{GS}}\rangle$ is the Heisenberg ground state – the lowest energy eigenstate – of the interacting system. At non-zero temperature, thermodynamic averages need to be evaluated. Though, we are only interested in the case where $T = 0$ and $t > 0$. In spatio-temporal invariant systems only the differences of the positions and times $(\mathbf{x}_2 - \mathbf{x}_1; t_2 - t_1)$ are relevant. This simplifies 1.94 to

$$iG(\mathbf{x}, t) = \frac{\langle \psi_{\mathrm{GS}} | \, \hat{\psi}(\mathbf{x}, t) \hat{\psi}^\dagger(\mathbf{0}, 0) \, | \psi_{\mathrm{GS}} \rangle}{\langle \psi_{\mathrm{GS}} | \psi_{\mathrm{GS}} \rangle} \,. \tag{1.97}$$

Analogously to 1.94 we can also use

$$iG_{\mathbf{k}}(t) = \frac{\langle \psi_{\mathrm{GS}} | \, \hat{a}_{\mathbf{k}}(t) \hat{a}^\dagger_{\mathbf{k}}(0) \, | \psi_{\mathrm{GS}} \rangle}{\langle \psi_{\mathrm{GS}} | \psi_{\mathrm{GS}} \rangle} \tag{1.98}$$

to describe the Fourier components of 1.94 in momentum space [14, 21]. Working in real-time t brings certain difficulties such as complex-valued terms for the diagrammatic expansion of the Green's function, which – as a consequence – also introduces the sign problem. It describes the problem where the weighted sum of values with non-positive weights results in a worse or even no convergence of the series. A general strategy to combat this problem is to develop the analytic continuation of the Green's function to imaginary time $\tau = it$ and imaginary frequency $\xi = -i\omega$. Defining a more readable notation

$$\hat{H} \, |n, \mathbf{k}\rangle = E_n(\mathbf{k}) \, |n, \mathbf{k}\rangle \tag{1.99}$$

enables us to rewrite

$$\begin{aligned} G^i(\tau, \mathbf{k}) &= - \langle \psi_{\mathrm{GS}} | a_{\mathbf{k}}(\tau) a^\dagger_{\mathbf{k}}(0) | \psi_{\mathrm{GS}} \rangle \\ &= - \sum_{|n,\mathbf{k}\rangle} \langle \psi_{\mathrm{GS}} | e^{\hat{H}\tau} a_{\mathbf{k}} e^{-\hat{H}\tau} | n, \mathbf{k} \rangle \, \langle n, \mathbf{k} | a^\dagger_{\mathbf{k}} | \psi_{\mathrm{GS}} \rangle \\ &= - \sum_{|n,\mathbf{k}\rangle} e^{-E_n(\mathbf{k})\tau} e^{E_{\mathrm{vac}}\tau} \, \langle \mathbf{k} | n, \mathbf{k} \rangle \, \langle n, \mathbf{k} | \mathbf{k} \rangle \\ &= - \sum_n Z_n(\mathbf{k}) e^{-E_n(\mathbf{k})\tau} \end{aligned} \tag{1.100}$$

where we have shifted the energy scale such that $E_{\mathrm{vac}} = 0$ and introduce the *Z-factor*, *quasiparticle residue* or *quasiparticle weight*

$$Z_n(\mathbf{k}) = | \, \langle n, \mathbf{k} | \mathbf{k} \rangle^2 \, | \,, \tag{1.101}$$

a number on $[0, 1]$ which describes the similarity of the bare electron state to the eigenstate of the interacting system [19, 7, 12].

1.6 Wick's Theorem

Before diving into the diagrammatics and sketching all kinds of diagrams for the imaginary time Green's function, we must introduce some useful mechanisms that will aid in exploring higher-order diagrams. The normal order of a sequence of operators is defined in such a way that all creation operators are to the left side. Looking at arbitrary creation/annihilation operators $a, a^\dagger, b, c^\dagger \ldots$ the normal order might look like

$$\hat{N}[aa^\dagger bc^\dagger \ldots] = (-1)^P a^\dagger c^\dagger \ldots ab \ldots , \tag{1.102}$$

where P is the number of fermionic permutations of operators that do not commute. Thus, the ordering of the bosonic/fermionic ladder operators are not relevant, *except* that all the creation operators need to be on the left.

The contraction of operators is defined as the difference between the imaginary time ordered and the normal ordered products of two operators [21]:

$$\overbracket{AB} = \hat{T}[AB] - \hat{N}[AB] \tag{1.103}$$

As an example, we take the contraction of an electron annihilation operator evolved to time τ_1 and an electron creation operator evolved to time τ_2 and set $\tau_1 > \tau_2$ to get

$$\begin{aligned} \overbracket{a_{\mathbf{k}_2}(\tau_1)a^\dagger_{\mathbf{k}_1}(\tau_2)} &= a_{\mathbf{k}_2}(\tau_1)a^\dagger_{\mathbf{k}_1}(\tau_2) - (-1)a^\dagger_{\mathbf{k}_1}(\tau_2)a_{\mathbf{k}_2}(\tau_1) \\ &= (a_{\mathbf{k}_2}a^\dagger_{\mathbf{k}_1} + a^\dagger_{\mathbf{k}_1}a_{\mathbf{k}_2})e^{-(\varepsilon(\mathbf{k}_2)\tau_1 - \varepsilon(\mathbf{k}_1)\tau_2)} \\ &= \delta_{\mathbf{k}_1,\mathbf{k}_2}e^{-\varepsilon(\mathbf{k}_2)(\tau_1-\tau_2)} \end{aligned} \tag{1.104}$$

where we have used Eq. 1.90 and Eq. 1.91 to evaluate the time evolution of the operators. Analogously, we evaluate and list all other possible combinations of contractions of operators:

$$\begin{aligned} \overbracket{a_{\mathbf{k}_2}(\tau_1)a^\dagger_{\mathbf{k}_1}(\tau_2)} &= \theta(\tau_1-\tau_2)\delta_{\mathbf{k}_1,\mathbf{k}_2}e^{-\varepsilon(\mathbf{k}_2)(\tau_1-\tau_2)} \\ &= -\theta(\tau_1-\tau_2)\delta_{\mathbf{k}_1,\mathbf{k}_2}G_0(\tau_1-\tau_2,k_1)\,, \end{aligned} \tag{1.105}$$

$$\overbracket{a_{\mathbf{k}_2}(\tau_1)a_{\mathbf{k}_1}(\tau_2)} = 0\,, \tag{1.106}$$

$$\overbracket{a^\dagger_{\mathbf{k}_2}(\tau_1)a^\dagger_{\mathbf{k}_1}(\tau_2)} = 0\,, \tag{1.107}$$

$$\begin{aligned} \overbracket{b_{\mathbf{q}_2}(\tau_1)b^\dagger_{\mathbf{q}_1}(\tau_2)} &= \theta(\tau_1-\tau_2)\delta_{\mathbf{q}_1,\mathbf{q}_2}e^{\omega(\mathbf{q})(\tau_1-\tau_2)} \\ &= -\theta(\tau_1-\tau_2)\delta_{\mathbf{q}_1,\mathbf{q}_2}D_0(\tau_1-\tau_2,\mathbf{q})\,, \end{aligned} \tag{1.108}$$

$$\overbracket{b_{\mathbf{q}_2}(\tau_1)b_{\mathbf{q}_1}(\tau_2)} = 0\,, \tag{1.109}$$

$$\overbracket{b^\dagger_{\mathbf{q}_2}(\tau_1)b^\dagger_{\mathbf{q}_1}(\tau_2)} = 0\,. \tag{1.110}$$

The meaning of $G_0(\tau, \mathbf{k})$ and $D_0(\tau, \mathbf{q})$ will be explained in the next section. For now, we just define these quantities to simplify the notation. In the first two equations we have included the additional factor $\theta(\tau_1 - \tau_2)$ to signalize the necessity $\tau_1 > \tau_2$.

Otherwise, the time ordering operator would swap the two operators, causing a change in sign and effectively rendering the sum of time-independent operators zero:

$$\overbrace{a_{\mathbf{k}_2}(\tau_1)a^\dagger_{\mathbf{k}_1}}(\tau_2) = (-a^\dagger_{\mathbf{k}_1}a_{\mathbf{k}_2} + a^\dagger_{\mathbf{k}_1}a_{\mathbf{k}_2})e^{-(\varepsilon(\mathbf{k}_2)\tau_1 - \varepsilon(\mathbf{k}_1)\tau_2)} = 0 \tag{1.111}$$

The contraction of operators belonging to different species is of course null as the operators commute with each other and consequently can be permutated effortlessly. As implied by Eq. 1.103 contraction is only defined between two arguments. Thus, contraction pairs are commonly placed adjacent to each other and can be factored out of the normal order operator as the result of a contraction between operators is simply a c-number, i.e.

$$\hat{N}[\overbrace{a_k(\tau_1)b_q(\tau_2)a_k(\tau_3)}a^\dagger_k(\tau_4)\ldots] = -\hat{N}[\overbrace{a_k(\tau_1)b_q(\tau_2)}a^\dagger_k(\tau_4)a_k(\tau_3)\ldots] \tag{1.112}$$

$$= -\hat{N}[\overbrace{a_k(\tau_1)}a^\dagger_k(\tau_4)b_q(\tau_2)a_k(\tau_3)\ldots] \tag{1.113}$$

Wick's theorem states that a product of creation and annihilation operators $\hat{T}[A_1A_2A_3\ldots A_{2n}]$ can be rewritten as the sum over all sums with increasing number of normal ordered contraction pairs [21], i.e.

$$\hat{T}[A_1A_2A_3\ldots A_{2n}] = \sum_{i=0}^{n} \sum_{\substack{\text{all}\\ \text{permutations}\\ \text{of } i\\ \text{contractions}}} \hat{N}[A_1A_2A_3\ldots A_{2n}] \tag{1.114}$$

or more explicitly

$$\begin{aligned} A_1A_2A_3\ldots A_{2n} = {} & \hat{N}[A_1A_2A_3\ldots A_{2n}] \\ & + \sum_{(i,j)} \hat{N}[\ldots \overbrace{A_i\ldots A_j}\ldots] \\ & + \sum_{(i_1,j_1),(i_2,j_2)} \hat{N}[\ldots \overbrace{A_{i_1}\ldots \overbrace{A_{i_2}\ldots A_{j_1}}\ldots A_{j_2}}\ldots] \\ & + \ldots \\ & + \sum_{(i_1,j_1),\ldots,(i_n,j_n)} \hat{N}[\overbrace{A_{i_n}\ldots \overbrace{A_{i_1}\ldots \overbrace{A_{i_2}\ldots A_{j_n}}\ldots A_{j_2}}\ldots A_{j_1}}]\,. \end{aligned} \tag{1.115}$$

We will call the last line in Eq. 1.115 the total pairing. The interesting property of this operator identity manifests itself by averaging over the ground state ψ_0, when all normal ordered products disappear [26] (since an annihilation operator acting upon ψ_0 vanishes) and only the total pairing survives:

$$\langle\psi_0|T[A_1A_2\ldots A_{2n}|\psi_0\rangle = \sum_{(i_1,j_1),\ldots,(i_n,j_n)} \hat{N}[\overbrace{A_{i_n}\ldots \overbrace{A_{i_1}\ldots \overbrace{A_{i_2}\ldots A_{j_n}}\ldots A_{j_2}}\ldots A_{j_1}}]\,. \tag{1.116}$$

To make this crystal clear let's take $a_1 a_2 a_1^\dagger a_2^\dagger$ as an example ($k_1 \neq k_2, 0 < \tau_1 < \tau$):

$$\begin{aligned} a_{k_1}(\tau)a_{k_2}(\tau_1)a_{k_1}^\dagger(\tau_1)a_{k_2}^\dagger(0) &= a_{k_1}^\dagger(\tau_1)a_{k_2}^\dagger(0)a_{k_1}(\tau)a_{k_2}(\tau_1) \\ &+ \hat{N}[\overbracket{a_{k_1}(\tau)a_{k_2}(\tau_1)a_{k_1}^\dagger(\tau_1)}a_{k_2}^\dagger(0)] + \hat{N}[\overbracket{a_{k_1}(\tau)a_{k_2}(\tau_1)a_{k_1}^\dagger(\tau_1)a_{k_2}^\dagger}(0)] \\ &+ \hat{N}[\overbracket{a_{k_1}(\tau)a_{k_2}(\tau_1)a_{k_1}^\dagger(\tau_1)}a_{k_2}^\dagger(0)] + \hat{N}[a_{k_1}(\tau)\overbracket{a_{k_2}(\tau_1)a_{k_1}^\dagger(\tau_1)a_{k_2}^\dagger}(0)] \\ &+ \hat{N}[a_{k_1}(\tau)\overbracket{a_{k_2}(\tau_1)a_{k_1}^\dagger(\tau_1)}a_{k_2}^\dagger(0)] + \hat{N}[a_{k_1}(\tau)a_{k_2}(\tau_1)\overbracket{a_{k_1}^\dagger(\tau_1)a_{k_2}^\dagger}(0)] \\ &+ \hat{N}[\overbracket{a_{k_1}(\tau)a_{k_2}(\tau_1)a_{k_1}^\dagger(\tau_1)a_{k_2}^\dagger}(0)] + \hat{N}[\overbracket{a_{k_1}(\tau)a_{k_2}(\tau_1)a_{k_1}^\dagger(\tau_1)a_{k_2}^\dagger}(0)] \\ &+ \hat{N}[\overbracket{a_{k_1}(\tau)\overbracket{a_{k_2}(\tau_1)a_{k_1}^\dagger(\tau_1)}a_{k_2}^\dagger}(0)] \,. \end{aligned} \tag{1.117}$$

As stated before contractions between operators of the same type (annihilation/creation) don't contribute to the sum, and neither do contractions between operators with different momenta. Using Eq. 1.105–Eq. 1.110 we get

$$\begin{aligned} a_{k_1}(\tau)a_{k_2}(\tau_1)a_{k_1}^\dagger(\tau_1)a_{k_2}^\dagger(0) &= a_{k_1}^\dagger(\tau_1)a_{k_2}^\dagger(0)a_{k_1}(\tau)a_{k_2}(\tau_1) \\ &+ G_0(\tau-\tau_1,k_1)a_{k_2}^\dagger(0)a_{k_2}(\tau_1) \\ &+ G_0(\tau_1,k_2)a_{k_1}^\dagger(\tau_1)a_{k_1}(\tau) \\ &+ G_0(\tau-\tau_1,k_1)G_0(\tau_1,k_2)\,. \end{aligned} \tag{1.118}$$

If this entity occurs in a perturbative expansion of the Green's function only the last term survives the averaging over the ground state

$$\langle\psi_0|a_{k_1}(\tau)a_{k_2}(\tau_1)a_{k_1}^\dagger(\tau_1)a_{k_2}^\dagger(0)|\psi_0\rangle = G_0(\tau-\tau_1,k_1)G_0(\tau_1,k_2) \tag{1.119}$$

1.7 From Green's Functions to Diagrams

Reading Green's functions and multi-dimensional integrals can prove to be a difficult and tedious task. Circumventing this problem, we now show that it is possible to express the imaginary time Green's function as an infinite sum of so-called *Feynman diagrams*. In doing so we will be able to combat some problems more efficiently and keep track of each term more easily. The term *diagrammatics* comprises all rules necessary to translate from and to the diagrammatic representation.

From Eq. 1.88 and Eq. 1.85 it follows that the time evolution operator must satisfy the differential equation

$$-\frac{\partial}{\partial\tau}\hat{U}_1(\tau) = \hat{H}_1(\tau)\hat{U}_1(\tau) \tag{1.120}$$

which can be integrated to yield

$$\hat{U}_1(\tau) = 1 - \int_0^\tau \mathrm{d}\tau_1\, \hat{H}_1(\tau_1)\hat{U}_1(\tau_1) \tag{1.121}$$

where U_1 denotes the time evolution operator in the interaction picture. Similarly to solving Volterra integral equations – which take on a similar form to the equation above – we may try to solve this using an iterative approach [7]. Acknowledging the fact that we are purely interested in imaginary time differences and using iteration we rewrite the above equation to

$$\hat{U}_1(\tau) = 1 - \int_0^\tau \mathrm{d}\tau_1\, \hat{H}_1(\tau_1) + \int_0^\tau \mathrm{d}\tau_1\, \hat{H}_1(\tau_1) \int_0^{\tau_1} \mathrm{d}\tau_2\, \hat{H}_1(\tau_2) + \dots \tag{1.122}$$

$$= \sum_{j=0}^{\infty} \frac{(-1)^j}{j!} \int_0^\tau \mathrm{d}\tau_1 \dots \int_0^\tau \mathrm{d}\tau_j\, \hat{T}\left[\hat{H}_1(\tau_1) \dots \hat{H}_1(\tau_j)\right] . \tag{1.123}$$

From the first to the second line we utilized the shortcut provided by the time ordering operator $\hat{T}$. With some renaming of variables and changing the order of integrations one can arrive at this integral equation, which effectively defines the time ordering operator, manually. Using Eq. 1.123 together with the Gell-Mann and Low theorem [10], Eq. 1.98 and the inverse of Eq. 1.81 applied to the time evolution operator in the Schrödinger picture

$$\hat{U}_S(\tau) = \hat{U}_0(\tau)\hat{U}_1(\tau)\hat{U}_0(0) = \hat{U}_0(\tau)\hat{U}_1(\tau) \tag{1.124}$$

we get the full interacting, single-particle Green's function

$$G(\tau, \mathbf{k}, \mu) = -\,\theta(\tau) \sum_{n=0}^{\infty} \frac{(-1)^n}{n!} \int_0^\tau \mathrm{d}\tau_1 \dots \int_0^\tau \mathrm{d}\tau_n \underbrace{\langle 0|\, \hat{T}[\hat{H}_1(\tau_1) \dots \hat{H}_1(\tau_n) a_k(\tau) a_k^\dagger(0)]\, |0\rangle}_{\equiv \Gamma_n} . \tag{1.125}$$

Now, we will inspect each term Γ_n of the sum individually. It is already clear to see that all odd orders in the series disappear. Ignoring the electron ladder operators in Eq. 1.125, the operators inside the sandwich of ground states contain (for all uneven orders) an uneven number of bosonic ladder operators. Noting that states with different numbers of phonons are orthogonal to each other

$$\langle 0|b_k|0\rangle = \langle 0|b_k^\dagger|0\rangle = 0\,, \tag{1.126}$$

we conclude that all odd terms in the series vanish. This is equivalent to saying an odd number of ladder operators $b_{\mathbf{q}}, b_{\mathbf{q}}^\dagger$ cannot be arranged in any order without changing the number of phonons. Consequently, we will number the following contributions to the full Green's function not by the number of interactions (0, 2, 4, ...) but rather by the number of phonons (0, 1, 2, ...). The zeroth order term is readily obtained and consists simply of the bare electron propagator

$$G_0(\tau, \mathbf{k}) = -\theta(\tau) e^{-\tau(\varepsilon(\mathbf{k}))} \tag{1.127}$$

which is illustrated in Fig. 1.2.

For long times the disconnected diagrams—which we do not sample with DMC—can be neglected. For short times however, they cause a strong potential drop. This

affects the efficacy of the sampling for long and short time diagrams. To overcome this limitation, the guiding function (or fictitious potential renormalization) leads the Makov chain to preferred regions in parameter space. In the case of the Fröhlich polaron, we modify the free electron propagator

$$G_0(\mathbf{k},\tau) \to G_0(\mathbf{k},\tau,\mu) = -\theta(\tau)e^{-\tau(\varepsilon(\mathbf{k})-\mu)} \tag{1.128}$$

to include the term $e^{\mu\tau}$, where μ is the renormalization parameter. Its optimal value is slighly below the exact ground state energy. The effects of the introduced renormalization must also be inverted when evaluating the results.

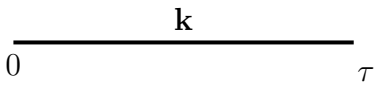

Figure 1.2: Zeroth order diagram $G_0(\tau,\mathbf{k})$ of the imaginary time Green's function.

For the first-order term we apply Wick's theorem from Section 1.6 to the following equation:

$$\begin{aligned}\Gamma_1(\tau,\mathbf{k},\mu) =& \hat{T}[\langle 0|\, \hat{H}_1(\tau_1)\hat{H}_1(\tau_2)a_k(\tau)a_k^\dagger(0)\,|0\rangle] \\ =& D_0(\tau_2-\tau_1,\mathbf{q})g(\mathbf{k}_1,\mathbf{q}_1)g(\mathbf{k}_2,\mathbf{q}_2) \\ & \hat{T}[\langle 0|\, a^\dagger_{k_1+q_1}(\tau_1)a_{k_1}(\tau_1)a^\dagger_{k_2+q_2}(\tau_2)a_{k_2}(\tau_2)a_k(\tau)a_k^\dagger(0)\,|0\rangle]\,.\end{aligned} \tag{1.129}$$

First, let's list all six variations of how to construct the full pairing of contractions. We will see that many of these vanish and we will analyze how to reduce these cumbersome steps effectively to see which combinations are of interest before writing them all down:

$$\hat{T}[\langle 0|\, a^\dagger_{k_1+q_1}(\tau_1)a_{k_1}(\tau_1)a^\dagger_{k_2+q_2}(\tau_2)a_{k_2}(\tau_2)a_k(\tau)a_k^\dagger(0)\,|0\rangle] = \tag{1.130}$$

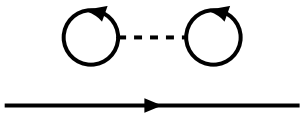

$$\overbrace{a^\dagger_{k_1+q_1}(\tau_1)}a_{k_1}(\tau_1)\overbrace{a^\dagger_{k_2+q_2}(\tau_2)}a_{k_2}(\tau_2)\overbrace{a_k(\tau)a_k^\dagger(0)}+ \tag{1.131}$$

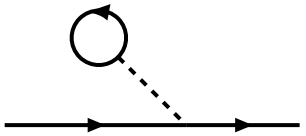

$$\overbrace{a^\dagger_{k_1+q_1}(\tau_1)}a_{k_1}(\tau_1)\overbrace{a^\dagger_{k_2+q_2}(\tau_2)a_{k_2}(\tau_2)a_k(\tau)a_k^\dagger(0)}+ \tag{1.132}$$

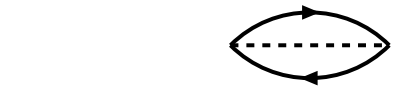

$$a^\dagger_{k_1+q_1}(\tau_1)a_{k_1}(\tau_1)a^\dagger_{k_2+q_2}(\tau_2)a_{k_2}(\tau_2)a_k(\tau)a^\dagger_k(0)+ \tag{1.133}$$

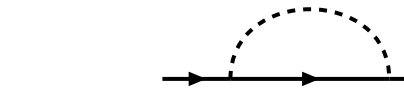

$$a^\dagger_{k_1+q_1}(\tau_1)a_{k_1}(\tau_1)a^\dagger_{k_2+q_2}(\tau_2)a_{k_2}(\tau_2)a_k(\tau)a^\dagger_k(0)+ \tag{1.134}$$

$$a^\dagger_{k_1+q_1}(\tau_1)a_{k_1}(\tau_1)a^\dagger_{k_2+q_2}(\tau_2)a_{k_2}(\tau_2)a_k(\tau)a^\dagger_k(0)+ \tag{1.135}$$

$$a^\dagger_{k_1+q_1}(\tau_1)a_{k_1}(\tau_1)a^\dagger_{k_2+q_2}(\tau_2)a_{k_2}(\tau_2)a_k(\tau)a^\dagger_k(0) \tag{1.136}$$

The terms have been visualized as diagrams which they lead to using rules we will introduce shortly. The linked cluster theorem affects Eq. 1.131 and Eq. 1.133, which tells us that those terms vanish [26, 21, 7]. If we switch and relabel the integration times $\tau_1 \leftrightarrow \tau_2$ then Eq. 1.132 and Eq. 1.136 (tadpole diagrams) are equal – so are Eq. 1.134 and Eq. 1.135. This cancels out the factor 1/2! in Eq. 1.125. The tadpoles are zero for the reason that the momentum $\mathbf{q}$ of the phonon line connecting it to the rest of the diagram vanishes. Zero-momentum phonons do not exist for this Hamiltonian. They indicate either a permanent strain or a translation of the crystal [18, 7]. Given the above equation, we can introduce a strict time ordering

$$\tau > \tau_2 > \tau_1 > 0 \tag{1.137}$$

since we have never talked about how τ_i and τ are ordered. Collecting all non-

vanishing terms of Eq. 1.130 leaves us with

$$
\begin{aligned}
&\overbrace{a^\dagger_{k_1+q_1}(\tau_1)a_{k_1}(\tau_1)}\,\overbrace{a^\dagger_{k_2+q_2}(\tau_2)a_{k_2}(\tau_2)}\,a_k(\tau)a^\dagger_k(0)+\\
&\overbrace{a^\dagger_{k_1+q_1}(\tau_1)a_{k_1}(\tau_1)}\,a^\dagger_{k_2+q_2}(\tau_2)\overbrace{a_{k_2}(\tau_2)a_k(\tau)}\,a^\dagger_k(0) = \\
&\quad \theta(\tau-\tau_2)\theta(\tau_2-\tau_1)\theta(\tau_1)\\
&\quad \delta_{\mathbf{k}_1+\mathbf{q}_1,\mathbf{k}_2}\delta_{\mathbf{k}_2+\mathbf{q}_2,\mathbf{k}}\delta_{\mathbf{k}_1,\mathbf{k}}\\
&\quad G_0(\tau-\tau_2,\mathbf{k},\mu)G_0(\tau_2-\tau_1,\mathbf{k}+\mathbf{q},\mu)G_0(\tau_1,\mathbf{k},\mu)+\\
&\quad +\theta(\tau_1-\tau_2)\theta(\tau-\tau_1)\theta(\tau_2)\\
&\quad \delta_{\mathbf{k}_1+\mathbf{q}_1,\mathbf{k}}\delta_{\mathbf{k}_2+\mathbf{q}_2,\mathbf{k}_1}\delta_{\mathbf{k}_2,\mathbf{k}}\\
&\quad G_0(\tau-\tau_1,\mathbf{k},\mu)G_0(\tau_2-\tau_1,\mathbf{k}+\mathbf{q},\mu)G_0(\tau_1,\mathbf{k},\mu)
\end{aligned}
\tag{1.138}
$$

as the only contributing terms. The deltas in the above equation effectively create the constraint

$$\mathbf{k} = \mathbf{k}_1\,, \tag{1.139}$$
$$\mathbf{k}_2 = \mathbf{k}+\mathbf{q}\,, \tag{1.140}$$
$$\mathbf{q} = \mathbf{q}_1 = -\mathbf{q}_2\,. \tag{1.141}$$

for the first term and

$$\mathbf{k} = \mathbf{k}_2\,, \tag{1.142}$$
$$\mathbf{k}_1 = \mathbf{k}+\mathbf{q}\,, \tag{1.143}$$
$$\mathbf{q} = \mathbf{q}_2 = -\mathbf{q}_1\,. \tag{1.144}$$

for the second. With the help of the Heaviside step functions, the limits of the integrals are again written in the explicitly dependent form. This way it is clear that there is a certain time ordering acting upon the integrand. The phonon momentum $\mathbf{q}$ is still an external variable that is summed over. This enables us to perform the substitution $\mathbf{q} \to -\mathbf{q}'$ and then relabeling $\mathbf{q}' \to \mathbf{q}$. We will see that this helps figure out momentum conservation at vertices when drawing diagrams. Using these results, we conclude

$$G_1(\tau,\mathbf{k},\mu) = -\sum_{\mathbf{q}}\int_0^\tau \mathrm{d}\tau_2 \int_0^{\tau_2}\mathrm{d}\tau_1 \tag{1.145}$$
$$G_0(\tau-\tau_2,\mathbf{k},\mu) \tag{1.146}$$
$$\frac{1}{\sqrt{N}}g(\mathbf{k}-\mathbf{q},\mathbf{q}) \tag{1.147}$$
$$G_0(\tau_2-\tau_1,\mathbf{k}-\mathbf{q},\mu)D_0(\tau_2-\tau_1,\mathbf{q}) \tag{1.148}$$
$$\frac{1}{\sqrt{N}}g(\mathbf{k},-\mathbf{q}) \tag{1.149}$$
$$G_0(\tau_1,\mathbf{k},\mu)\,. \tag{1.150}$$

or again in the written out form:

$$G_1(\tau, \mathbf{k}, \mu) = -\sum_{\mathbf{q}} \int_0^{\tau} \mathrm{d}\tau_2 \int_0^{\tau_2} \mathrm{d}\tau_1 \tag{1.151}$$

$$e^{-(\tau-\tau_2)(\varepsilon(\mathbf{k})-\mu)} \tag{1.152}$$

$$\frac{1}{\sqrt{N}} g(\mathbf{k}-\mathbf{q}, \mathbf{q}) \tag{1.153}$$

$$e^{-(\tau_2-\tau_1)(\varepsilon(\mathbf{k}-\mathbf{q})-\mu)} e^{-(\tau_2-\tau_1)\omega(\mathbf{q})} \tag{1.154}$$

$$\frac{1}{\sqrt{N}} g(\mathbf{k}, -\mathbf{q}) \tag{1.155}$$

$$e^{-\tau_1(\varepsilon(\mathbf{k})-\mu)}\,. \tag{1.156}$$

The equation has been split into multiple lines and the electronic and phononic pieces in Eq. 1.154 have been separated. We have previously defined G_0 and D_0 to help with the notation but we have yet to give these quantities meaningful interpretation. For a second let's forget that we already introduced these symbols and pretend as if we carried out the calculations on the last few pages with the more cumbersome exponentials. With these preparations the rules to transcode equations into diagrams can now be defined:

1. Terms with an exponential factor are represented by lines or arcs.

2. A factor $\exp\{-(\tau_2 - \tau_1)(\varepsilon(\mathbf{k}) - \mu)\}$ reflects the creation of an electron with momentum $\mathbf{k}$ at time τ_1 and its annihilation at τ_2. It is represented by a straight (electron) line from time τ_1 to τ_2 indexed by the momentum $\mathbf{k}$.

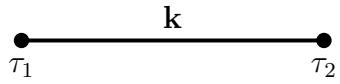

3. A factor $\exp\{-(\tau_2-\tau_1)\omega(\mathbf{q})\}$ reflects the creation of a phonon with momentum $\mathbf{q}$ at time τ_1 and its annihilation at τ_2. It is represented by a (phonon) arc from time τ_1 to τ_2 indexed by the momentum $\mathbf{q}$.

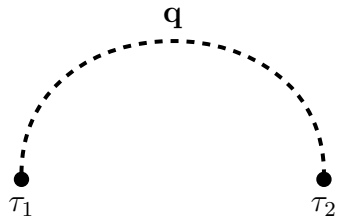

4. A vertex is a point that has an incoming and outgoing electron line and either an incoming or outgoing phonon arc, but not both. The value of a vertex is

given by $g(\mathbf{k}_{\text{in}}, \mathbf{k}_{\text{out}} - \mathbf{k}_{\text{in}})/\sqrt{N}$ with $\mathbf{k}_{\text{in}}$ being the momentum of the incoming electron and $\mathbf{k}_{\text{out}}$ being the momentum of the outgoing electron. Conservation of momenta therefore dictates the phonon momentum to be $\mathbf{q} = \mathbf{k}_{\text{out}} - \mathbf{k}_{\text{in}}$ for an incoming phonon and $\mathbf{q} = \mathbf{k}_{\text{in}} - \mathbf{k}_{\text{out}}$ for an outgoing phonon.

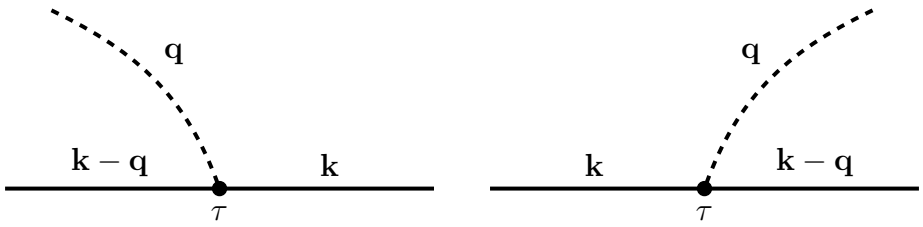

In the thermodynamic limit we can of course replace the sums over momenta with integrals so that the value of a vertex is now $g(\mathbf{k}_{\text{in}}, \mathbf{k}_{\text{out}} - \mathbf{k}_{\text{in}})/\sqrt{2\pi}$. Utilizing the above rules, we can now sketch the topology of the diagram of the first-order one-particle imaginary time Green's function, which can be seen in Fig. 1.3. It is clear to see that at the first/last vertex only the phonon creation/annihilation operator contributes. The third-order term in the number of interactions vanishes again and

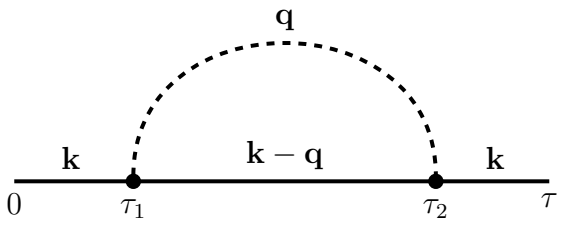

Figure 1.3: First order (in the number of phonons) diagram $G_1(\tau, \mathbf{k})$ of the imaginary time Green's function.

so the next non-null term in the series is the fourth-order term in the number of interactions, i.e. second order in the number of phonons. From now on when we talk about the order of a diagram, we will always mean the number of phonons. At this point, we stop writing down any higher-order terms for the Green's function as it would become impractical and incomprehensible. The second-order term could easily take up more than one page to visualize Wick's theorem.

Although, we can construct higher-order diagrams with just the graphical representations alone. With the aforementioned rules, we can then transcribe all diagrams to equations and vice versa since these rules constitute a one-to-one mapping. The generic algorithm for obtaining the n^{th} order term of the perturbation expansion is as follows:

1. Draw a horizontal line with $2n + 2$ nodes. This is the *electron backbone line* of the diagram.

2. Create all permutations of full time-ordered pairings of the inner vertices $\tau_1, \tau_2, \ldots, \tau_{2n}$:

   (a) $(\tau_1, \tau_2), (\tau_3, \tau_4), \ldots$

   (b) $(\tau_1, \tau_3), (\tau_2, \tau_4), \ldots$

   (c) $(\tau_1, \tau_4), (\tau_2, \tau_3), \ldots$

   (d) $\ldots$

3. One instance of such a pairing will translate to one diagram. Iterate over all pairs and draw a phonon propagator from the first to the second member of a pair. Repeat this for all other full pairings to get all the different topologies.

4. Label the phonon propagators by their momenta $q_1, q_2, \ldots, q_n$.

5. Calculate the momenta of all electron propagators. Start with $\mathbf{k}$ for the first propagator and then apply the vertex rule mentioned before recursively to all vertices to get the momenta.

The second order diagram has two phonon propagators from τ_1 to τ_2 and from τ_3 to τ_4, with the conditions (which follows from previous calculations) that each time is unique. This leaves us with three different possible configurations:

$$\tau_1 < \tau_2 < \tau_3 < \tau_4 \,, \tag{1.157}$$

$$\tau_1 < \tau_3 < \tau_2 < \tau_4 \,, \tag{1.158}$$

$$\tau_1 < \tau_3 < \tau_4 < \tau_2 \,. \tag{1.159}$$

To not get confused with the time ordering we decide on the time ordering convention $0 < \tau_1 < \tau_2 < \ldots < \tau$ for all diagrams by relabeling the vertices. Fig. 1.4 visualizes the topology of the second-order diagrams. We can easily get the number N of different topologies of an n^{th} order diagram by looking at the problem differently. Let's imagine we have $2n$ balls and we would like to get all variations on how the balls can be grouped into pairs of two. We could do this iteratively:

1. $n = 1$: $N_1 = 1$

2. $n = 2$: the first ball can be paired with three different balls, leaving N_1 pairings for the rest of the balls, i.e. $N_2 = 3 * N_1 = 3$

3. $n = 3$: the first ball can be paired with five different balls, leaving N_2 pairings for the rest of the balls, i.e. $N_3 = 5 * N_2 = 15$

4. $n = x$: the first ball can be paired with $2x - 1$ different balls, leaving N_{x-1} pairings for the rest of the balls, i.e. $N_x = (2x - 1) * N_{x-1}$

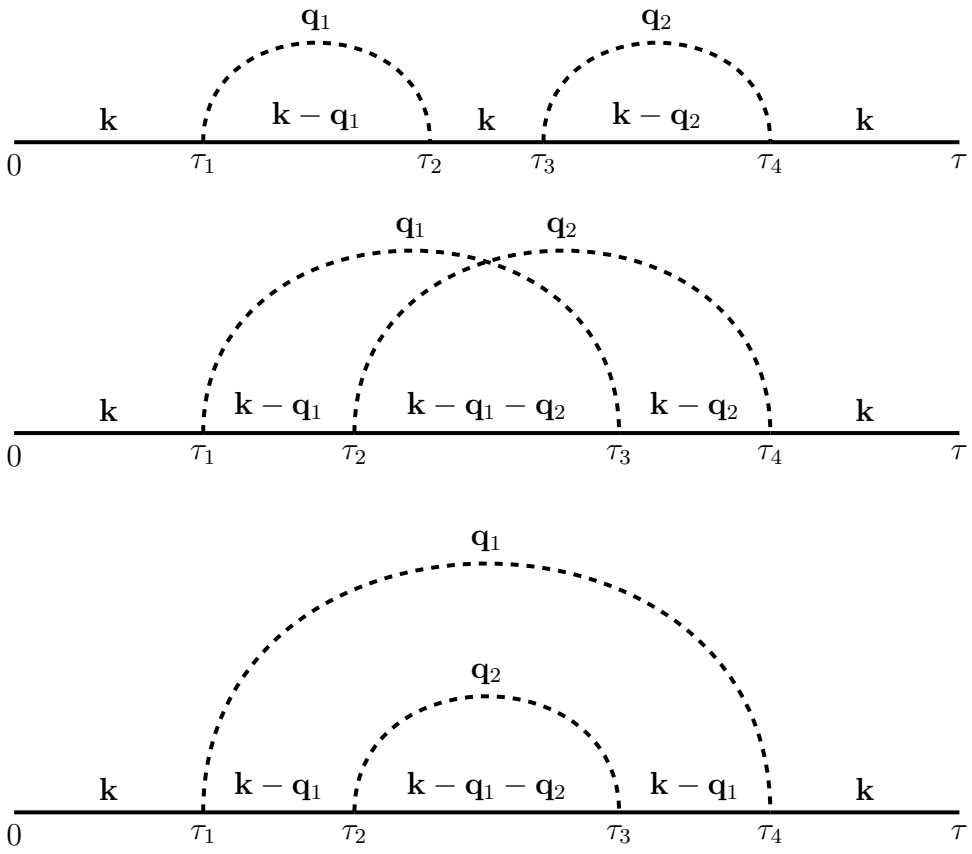

Figure 1.4: Topology of all second-order diagrams

To convert this into an explicit non-recursive formula let's tackle the problem with a different approach. Lay down the balls in a line and group the first two, then the second two, etc. The number of all permutations is $(2n)!$. However, we have now overcounted many configurations. Permuting the individual pairs gives a factor $n!$. Furthermore, we can also swap the members of $1, 2, \ldots, n$ pair(s) which gives 2^n. The total number of full pairings is therefore

$$N(n) = \frac{(2n)!}{n!\ 2^n} = (2n-1)!!\,. \tag{1.160}$$

To demonstrate how fast the diagram space grows with the diagram order we calculate e.g. $N(10) = 654729075$. One of these many 10^{th} order diagrams can be seen in Fig. 1.5. As we will see in later chapters we can calculate the full expansion of $G(\tau, \mathbf{k}, \mu)$ by *walking* through this diagram space and sampling every possible configuration. Obviously "every" is a strong word when talking about infinite state spaces, but the nature of the Green's function will enable collecting only lower order diagrams with a trick that has already been mentioned – the fictitious potential renormalization. First, it is important to examine what we can calculate from the Green's function.

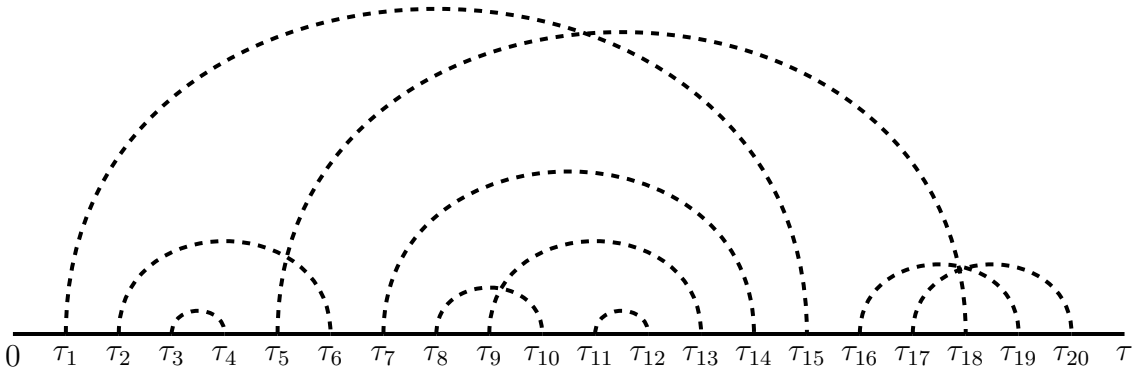

Figure 1.5: One of the many 10^{th} order diagram topologies.

1.8 Obtaining Metrics from Green's Functions

We have discussed how to acquire and expand the one-particle imaginary-time Green's function. A general form was given in Eq. 1.100. To conveniently evade having to deal with negative quantities, we define the positive-definite Green's function

$$\bar{G}(\tau, \mathbf{k}, \mu) = -G(\tau, \mathbf{k}, \mu) = \theta(\tau) \sum_n Z_n(\mathbf{k}) e^{-E_n(\mathbf{k})\tau} \tag{1.161}$$

with which we shall work from now on. Examining the long-time behavior of this equation, we note that all contributions other than the zeroth order term vanish exponentially faster. This enables us to extract quantities out of the high-τ range:

$$\lim_{\tau \to \infty} \bar{G}(\tau, \mathbf{k}, \mu) = \theta(\tau) Z_0(\mathbf{k}) e^{-E_0(\mathbf{k})\tau} \,. \tag{1.162}$$

By fitting the logarithm of Eq. 1.162 the resulting linear function has the ground state energy $E_0(\mathbf{k})$ as the slope and the quasi-particle weight $Z_0(\mathbf{k})$ can be recovered by exponentiating the offset from zero. Another metric contained in the Green's function is the effective mass. When dressed by phonons the electron positively shifts its mass. The stronger the interaction the heavier the electron appears compared to the bare particle. The effective mass $m^\star$ is defined as

$$m^\star = \left(\frac{\partial^2 E_0(\mathbf{k})}{\partial k^2} \right)^{-1}_{k=0} \tag{1.163}$$

Chapter 2

Classic Monte Carlo

As seen in the previous sections we often seek to calculate the expectation value of some observable $O(r^N)$. This may be accomplished by averaging over the configuration space $\mathcal{Q}$

$$\langle O \rangle = \frac{\int_{\mathcal{Q}} \mathrm{d}\mathbf{r}^N \, O(\mathbf{r}^N) e^{-\beta U(\mathbf{r}^N)}}{\int_{\mathcal{Q}} \mathrm{d}\mathbf{r}^N \, e^{-\beta U(\mathbf{r}^N)}} \,, \tag{2.1}$$

with $\beta = \frac{1}{k_B T}$ being the inverse temperature. These integrals are extremely hard — if not impossible — to calculate analytically. To circumvent this problem we take another approach, which could almost be described as a brute-force attack on the nature of the equation. If we came to know the shape of the probability distribution

$$f(\mathbf{r}^N) = \frac{e^{\beta U(\mathbf{r}^N)}}{\int_{\mathcal{Q}} \mathrm{d}\mathbf{r}^N \, e^{\beta U(\mathbf{r}^N)}} \tag{2.2}$$

then the canonical average $\langle O \rangle$ could be calculated by averaging over a sample $\left\{\mathbf{r}_i^N | i \in \{1, \ldots, M\}, r_i \in \mathcal{Q}\right\}$ that was drawn from $f(\mathbf{r}^N)$

$$\langle O \rangle \approx \frac{1}{M} \sum_{i=1}^{M} A(r_i^N) \tag{2.3}$$

It becomes clear that the underlying difficulty is generating a sample of such a probability distribution. Metropolis et al. [23] proposed a solution to this problem in 1953, known as the *Metropolis algorithm*. The core idea is to generate a Markov chain of states $r_1^N, r_2^N, \ldots, r_M^N$, see Fig. 2.1. An important attribute is the *memoryless* Markov property: The probability of state r_i^N transitioning to a future state r_{i+1}^N depends solely on the current configuration, i.e.

$$p(\mathbf{r}_{i+1}^N | \mathbf{r}_i^N) = p(\mathbf{r}_{i+1}^N | \mathbf{r}_i^N, \mathbf{r}_{i-1}^N, \ldots, \mathbf{r}_1^N) \,. \tag{2.4}$$

We label this conditional property

$$p(\mathbf{r}_{i+1}^N | \mathbf{r}_i^N) = p(\mathbf{r}_i^N \to \mathbf{r}_{i+1}^N) \tag{2.5}$$

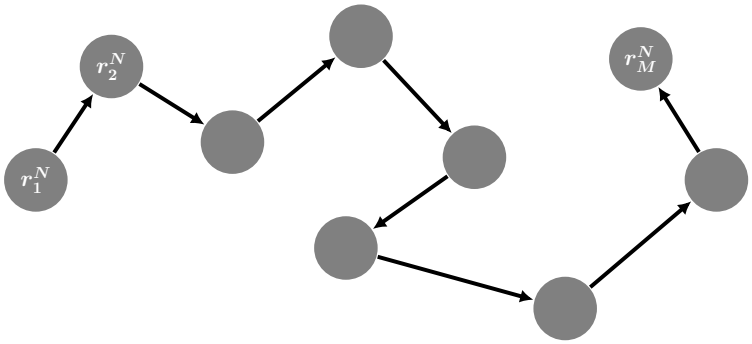

Figure 2.1: Markov Chain of configurations $\mathbf{r}_i^N$ in state space

the *transition probability*. To simplify reading the following it is easier to define $x \equiv \mathbf{r}^N \in \mathcal{Q}$. How to propose and accept/reject a new state will be explained shortly. First, we need to discuss necessary conditions needed for the MC method to be applicable.

2.1 Global vs detailed balance

In creating a Markov chain, we walk the configuration space and draw samples/measure quantities at every node. The new distribution is given by

$$f^{(n+1)}(x) = \sum_y f^{(n)}(y) p(y \to x) \tag{2.6}$$

which means that the new value of the $f(x)$ is the sum of the PDF of all other states y times the probability of transitioning to the state x. In the limit $n \to \infty$ we would like for $f^{(n)}(x)$ to be stationary; another step should not change $f^{(n)}(x)$. This requires that we imply *global balance* at all times, i.e.

$$\sum_y f(x) p(x \to y) = \sum_y f(y) p(y \to x) \qquad \forall y\,. \tag{2.7}$$

It describes that the net flow of probabilities by moving *away* from state x should equal the flow of probabilities by moving *into* state x. This is, of course, not feasible for every problem and is often impractical. A more strict but simpler restriction is that of *detailed balance*, where we just remove the sum from the above equation:

$$f(x) p(x \to y) = f(y) p(y \to x) \qquad \forall x, y\,. \tag{2.8}$$

Instead of requiring that all transitions (in and out) balance each other, we force that being in state x and moving to another state y should be equally probable as being in state y and transitioning to state x. A schematic visualization can be seen in Fig. 2.2.

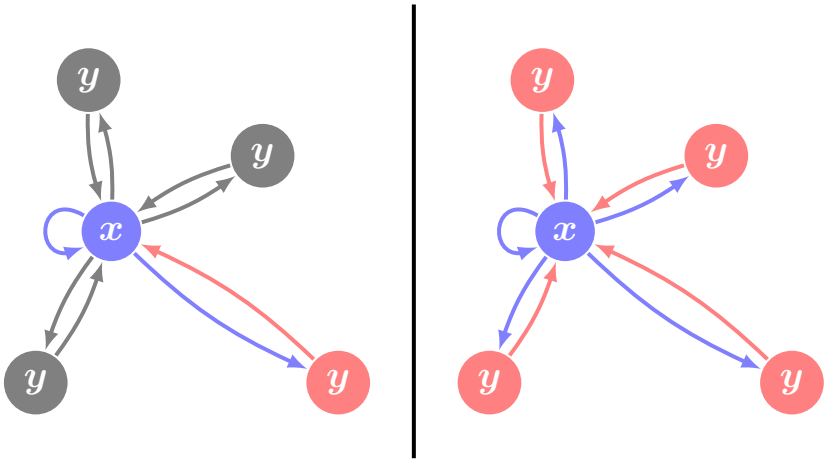

Figure 2.2: Illustration of detailed (left) vs global balance (right)

2.2 Markow Chain Monte Carlo

Now that we know the requirements of an MC algorithm we can elaborate on how to perform updates and how to decide whether to accept or reject them. The Markov Chain Monte Carlo (MCMC) technique—specifically the Metropolis-Hastings algorithm [15]—is used to sample from functions $f(x)$, which only need to be proportional to the density $P(x)$ we are interested in

$$f(x) \sim P(x) \tag{2.9}$$

$$\int_{\mathcal{Q}} \mathrm{d}x\, f(x) = c\,, \tag{2.10}$$

where $c \in \mathbb{R}$. Thus, we need not know the exact normalization factor of the PDF we are working with. At a given time t, the system under observation occupies a certain state/configuration x in the state/configuration space. It may transition to another state y for the time $t+1$ with the probability of $p(x \to y)$ or remain in the same state x. Knowing that we apply a two-step loop in a generate-accept/reject pattern gives us essential information already. First off, the transition probability $p(x \to y)$ from configuration x to y can be split into a product

$$p(x \to y) = p_{\text{gen}}(x \to y) p_{\text{acc}}(x \to y) \tag{2.11}$$

where $p_{\text{gen}}(x \to y)$ and $p_{\text{acc}}(x \to y)$ are the generation and acceptance probabilities, respectively. This is only possible because these probabilities are statistically independent. With detailed balance and the just obtained equation, we can obtain

$$f(x) p_{\text{gen}}(x \to y) p_{\text{acc}}(x \to y) = f(y) p_{\text{gen}}(y \to x) p_{\text{acc}}(y \to x) \tag{2.12}$$

Using symmetric generation probabilities[1] this equation can be rewritten and simplified to

$$\frac{p_{\text{acc}}(x \to y)}{p_{\text{acc}}(y \to x)} = \frac{f(y)}{f(x)} \,. \tag{2.13}$$

This is the detailed balance condition in its symmetric form. The Metropolis rule for accepting an update $x \to y$ is then

$$p_{\text{acc}}(x \to y) = \min\left[1, r \equiv \frac{f(y)}{f(x)}\right] \tag{2.14}$$

Now, it becomes evident that we do not care about whether the function f for proposing new states integrates to unity, since only ratios of the above form factor into the acceptance rate. The variable r, which we just defined as this ratio, will become a main object of interest for the various update procedures. The careful reader might now complain that the transition probability in Eq. 2.11 does not obey an important requirement for probability density—it is not normalized:

$$\sum_y p(x \to y) = \sum_y p_{\text{gen}}(x \to y) p_{\text{acc}}(x \to y) \leq 1 \,. \tag{2.15}$$

That is because even though the generation probabilities are normalized, the acceptance probabilities $p_{\text{acc}}(x \to y) \leq 1$ are not. Let's take a look at the total acceptance probability when the system is in state x

$$P_{\text{acc}}(x) \equiv \sum_y p_{\text{gen}}(x \to y) p_{\text{acc}}(x \to y) \tag{2.16}$$

and the total rejection probability

$$P_{\text{rej}}(x) \equiv 1 - P_{\text{acc}}(x) \,. \tag{2.17}$$

We notice that we have forgotten to count the rejected moves. To mitigate this issue we redefine the transition probability

$$p(x \to y) = \underbrace{p_{\text{gen}}(x \to y) p_{\text{acc}}(x \to y)}_{\text{accept}} + \underbrace{P_{\text{rej}}(x) \delta_{x,y}}_{\text{reject}} \tag{2.18}$$

This reveals the important knowledge that the rejected steps must not simply be discarded but a state has to be counted again if an update was rejected [33]. The structure of the Metropolis-Hastings algorithm is displayed in Algorithm 1. We perform a loop of elementary MC steps to walk through the configuration space. To collect meaningful data, e.g. an observable, or to produce a target distribution, additional actions may be inserted after every trial step, whether the update was rejected or not.

[1] This just means that given a state x the update from $x \to y$ is selected from the pool of updates with a probability equal to that of being in state y and choosing the update $y \to x$.

Data: proposal PDF f_0
target PDF π
initial configuration x_0

$t \leftarrow 0$;
perform warmup;
while $t <$ *number of samples* **do**
  generate a new proposal configuration x' from $f_t(x'|x_t)$;
  $p_{\text{acc}} \leftarrow \min\left[1, \frac{f_t(x_t|x')}{f_t(x'|x_t)} \frac{\pi(x')}{\pi(x_t)}\right]$;
  if $p_{acc} \geq 1$ **then**
    $x_{t+1} \leftarrow x'$;
  else
    $r \leftarrow$ random number from $U(0,1)$;
    if $r \leq p_{acc}$ **then**
      $x_{t+1} \leftarrow x'$;
    else
      $x_{t+1} \leftarrow x_t$;
    end
  end
  $t \leftarrow t + 1$;
end

Algorithm 1: Metropolis-Hastings algorithm for symmetrical update probabilities.

2.3 Ergodicity

For uncountably infinite state spaces, such as the position and momentum space it is simply impossible to sample all states during a simulation run [27]. Therefore, we introduce another requirement for a usable MC algorithm. Ergodicity describes the property that the simulation must be able to propagate from an arbitrary configuration to any other configuration in a *finite* number of steps. This does not mean that we have to construct a full graph of all the states in the state space, but rather that the undirected graph must be connected, i.e. there has to be at least one path of non-zero transition probabilities from state x to state y for all $x, y \in \mathcal{Q}$. For the case of the one-particle Green's function, this means that we need to find updates, that enable us to reconstruct every possible topology that obeys the diagram rules presented in Section 1.7. The principle of ergodicity is illustrated in Fig. 2.3.

2.4 Warmup and the equilibration phase

In a naive MC algorithm, one would start measuring an observable O right from the start. This is not always a wise choice. The initial configuration of the system is

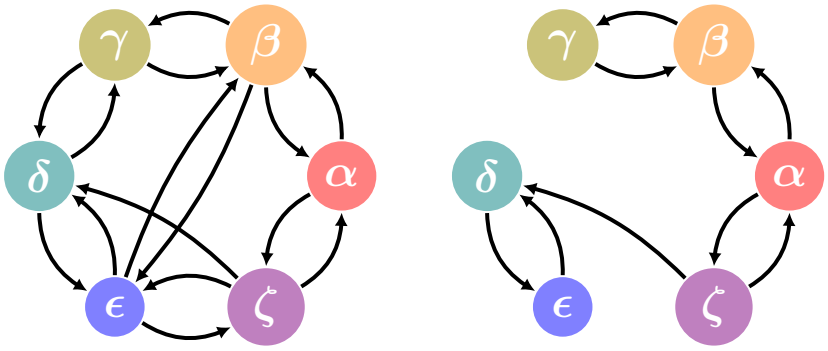

Figure 2.3: In a state space with only the configurations $\{\alpha, \beta, \gamma, \delta, \epsilon, \zeta\}$ the left graph obeys the condition of ergodicity, while in the right graph the states δ and ϵ do not permit a transition to any other configuration other than themselves, rendering the graph non-ergodic. The transitions that have non-zero probabilities are depicted with arrows.

often a very simple one. A prime example is the 2-dimensional Ising model. Imagine a simple cubic lattice in two dimensions. Every lattice point hosts an atom with a magnetic dipole moment. These spins can take on values $+1/-1$ and have a chance to flip, depending on the current energy of the system. The simulation might be started with all spins pointing upwards or downwards. Thus the energy is maximized (minimized) for an antiferromagnetic (ferromagnetic) system, which means it is its energetically least (most) favorable configuration. The antiferromagnetic system will therefore flip a lot of spins at the beginning of the simulation to get near its equilibrium state (half of the spins up, half of the spins down).

Since we are only interested in measuring quantities in the equilibrium it would distort our measurements greatly, if we were to start measuring right off the start. That is why every Monte Carlo simulation benefits from a warmup/equilibration phase in which the system is allowed to transition from its starting to a more "natural" configuration before measurements are performed.

Chapter 3

Diagrammatic Monte Carlo (DMC)

In their essence, Monto Carlo (MC) algorithms employ the application of random numbers for problems that are deterministic in their nature. Thus, MC methods belong to the category of numerical and stochastic methods and make up a tremendous class of unique algorithms. The principle of random sampling was first proposed in the late 1940s by Stanislaw Ulam who gave it its name inspired by the Monte Carlo Casino in Monaco [22]. At that time the method was severely limited by computational efficacy. Through several decades the MC idea has made its way into various fields, not limited to science alone: physics, computational biology, finance and even the game industry, just to name a few.

In the following sections we will first give a general – yet simplistic – introduction to the MC method in general and use the developed ideas to aid in constructing an algorithm for computing the Green's function. Among others, we will particularly rely on work from [19], [33], [34] and [27].

Now that we have a solid foundation of how MC simulations work in general, an introduction to *Diagrammatic Quantum Monte Carlo* (DQMC/DMC) methods can be given. In this thesis two slightly different approaches will be implemented and examined:

- A bare scheme for directly calculating the single-particle imaginary time Green's function G of the polaron.
- A bare scheme for simulating the proper self-energy Σ of G and feeding the obtained result into the Dyson equation to obtain G.

Given the Green's function we can then calculate the ground state energy E_0, the Z_0 factor, investigate convergence behavior with restrictions on minimum/maximum diagram order, analyze the ground state energy with respect to the total momentum $\mathbf{p}$ or the coupling strength α. It must be stressed, that DMC does more than just list all possible diagrams of order $n < n_{\max}$ and integrate every single one with conventional MC techniques. The integration happens implicitly in DMC by treating every point in the configuration space equally. Most of the following information has been collected from [34], [27], [19], [12], [5] and [11].

3.1 Foundations of a DMC Algorithm

One of the most important properties to note about DMC is that it is numerically exact—meaning it does not show systematic errors like for example a perturbative expansion where we disregard higher orders—but shares the behavior of statistical disturbances of other RNG-based methods. If a DMC algorithm were to run on a machine with unlimited computing potential and unlimited memory for an infinite amount of time we would get the exact one-particle imaginary time Green's function in return. Unfortunately, this machine has yet to be invented, which means that we have to think carefully about how to design an algorithm that

1. is computationally efficient,
2. is memory-efficient,
3. can take "big" steps in configuration space, so that we cover most of the space with low density instead of covering only part of it with high density, see Fig. 3.1, and
4. converges to a single value for each observable.

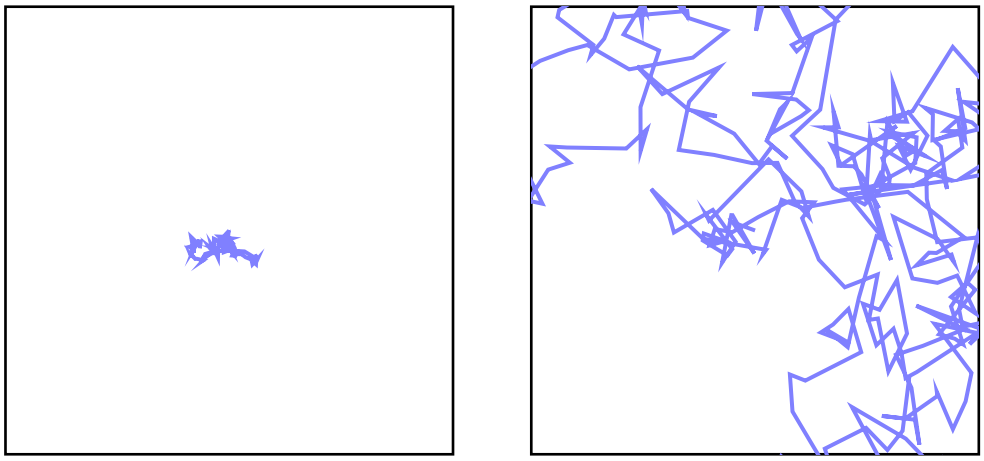

Figure 3.1: Schematic illustration of configuration space and the random walk. Our goal is to generate big steps (right) to reduce the number of steps needed before we can obtain meaningful data. Each point represents a measurement of the system in this state. We can emulate big step sizes by taking multiple steps in between measurements. This is especially important for calculations where we want to keep the number of measurements low, e.g. to visualize error bars.

The expansion of the Green's function that has been introduced in Section 1.7 and its visualization technique is applied in various fields of physics. The number of integration variables increases linearly with diagram order. Let's forget about the Green's function for a moment and think about the underlying, more generic problem

at hand. In general we seek a quantity $Q(\mathbf{y})$ that is dependent on some multi-dimensional set of external variables $\mathbf{y}$. Its diagrammatic expansion is expressed as

$$Q(\mathbf{y}) = \sum_{n=0}^{\infty} \sum_{\mathcal{T}} \int \dots \int \mathrm{d}\mathbf{x}_1 \dots \mathrm{d}\mathbf{x}_n \, \mathcal{D}(n, \mathcal{T}; \mathbf{x}_1, \dots, \mathbf{x}_n; \mathbf{y}) \tag{3.1}$$

where $\mathcal{D}$ refers to a known function—later we will see, that these functions can be expressed in terms of diagrams for the case of this thesis. The set $\mathbf{y}$ denotes external parameters that might influence the system. In the above representation, the diagram order n corresponds to the number of internal summations/integrations. Hence, the order limits the number of internal variables $\{\mathbf{x}_i\}$. We shall revert back to the convention that n describes the number of phonon propagators shortly. The sum over the *topology index* $\mathcal{T}$ incorporates and indexes terms of the same order. Combining all these internal and external parameters results in what has previously been mentioned as *configuration space* and one tuple of all parameters corresponds to exactly one point $\nu \equiv \{n, \mathcal{T}; \mathbf{x}_1, \dots, \mathbf{x}_n; \mathbf{y}\}$ in this space. For this thesis, the internal variables will be "local" quantities like the imaginary time τ of a vertex, the momentum $\mathbf{q}$ of a phonon propagator, etc. The global momentum $\mathbf{p}$ and the coupling strength α are, among others, examples of external variables. Recalling the MCMC method from Chapter 2 it appears that we will start with a specific point ν_0 in this state space and watch its evolution as it traverses vast distances in the configuration space due to various update procedures.

The most prominent examples for a function $\mathcal{D}$ are—as the name of the method suggests—Feynman diagrams. From now on we will specialize in this many-body problem. We can schematically write

$G(\mathbf{p}, \tau) =$ 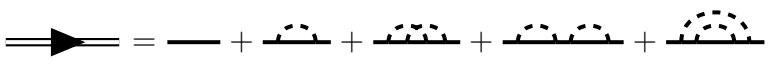 $+ \dots$ (3.2)

The single diagrams can (up to a phase factor c) also be rephrased as a product of propagators $\mathcal{D} = c \prod_{\text{lines}} F_{\text{line}}$, which can be taken directly from Section 1.7. The form of Eq. 3.1 is not limited to DMC alone. Various other methods, including but not limited to path integral MC or impurity solvers, build upon this representation of an ensemble mean [27].

3.1.1 Intepreting $Q(\mathbf{y})$ as a Probability Density

The general idea behind a DMC algorithm is to interpret Eq. 3.1 as a probability density function of the external variable $\mathbf{y}$. By performing an MCMC method the simulation walks through configuration space and can collect statistics for the desired quantities accordingly. For continuous functions such as Green's functions, this may be accomplished by generating a histogram. How to bypass the systematic errors introduced by a histogram approach will be elaborated on soon. Treating some quantity as a PDF might prove to be a problem when the observed $Q(\nu)$ does not tick all the boxes for a PDF. In Chapter 1 we have learned how to reformulate the

problem such that the Green function is real and positive-definite. From the last section about the generic MC method, we have taken away that for the Metropolis-Hastings algorithm it does not matter whether the quantity in question is correctly normalized, as the normalization factors cancel each other when calculating the acceptance probability.

We know that $Q(\nu)$ is a joint probability density of internal and external variables [12]. It makes sense that when binding and setting all external variables to a certain value, one is left with a scalar, for example, the ground state energy for $p = 0, \alpha = 0$. Omitting this constraint and letting the diagram change its external variables, e.g. the global momentum, results in an entity E_0 as a function of the free symbol. Following this idea, it is easily achieved to also generate a 2d map of $E_0(p, \alpha)$.

3.1.2 Difference to Classical MC

In contrast to the general MC procedure, it is noteworthy to point out that the DMC method has varying dimensionality in the state vector ν thanks to the order parameter n. This means that in addition to updates that change internal or external parameters, we will also utilize updates that change the diagram's order. When talking about the specific updates in more detail we will also conclude that there is a minimal set of updates required to fulfill ergodicity. Surprisingly, this set consists of only two updates for the simple case of restricting all external variables to a predefined value. For every external variable that we want to "unbind", we will have to introduce another update that uniquely modifies said variable.

In DMC, autocorrelation times are negligible, for most of the time ($> 99\%$) the diagram will remain in the zeroth-order. In fact for low orders, the diagram may be decorrelated in constant time and this is done in under 1 ms [27].

3.2 Warmup for DMC Simulations

Another important part of an MC algorithm—besides a list of update procedures and measurements—is the start configuration. For simplicity we will start the simulation from the 0^{th} order diagram, see Fig. 1.2. This simplification justifies that—as for every normal MC simulation—we will also introduce a warmup phase for DMC calculations. It might not be apparent as to why this is necessary as the system can transition very quickly from a basic configuration such as the 0^{th} order diagram to a higher-order one, but it is good practice to move away from a handpicked state in configuration space to avoid unnecessary systematic errors. For the simulations in this thesis a warmup time of 1 s corresponds to $\approx 1 \times 10^7$ updates (for $\alpha = 1, p = 0$), which is more than enough for the manual configuration to decay. It has to be noted that this depends heavily on the hardware used, see Appendix C.

3.3 Normalization

Revising the requirements of a PDF we argued that normalization is implicitly taken care of by the Metropolis-Hastings algorithm. But we have yet another unsolved normalization problem. When collecting statistics for a quantity Q during a simulation run, we will do this for example by applying the histogram method. That is, we separate a predefined interval $[0, \tau_{\max}]$ into N_{bins} and after every elementary MC step we measure our diagram and increment a certain bin by one. This leaves us with an unnormalized histogram at the end of the run, which we will call Q_{MC}. The normalization problem can be tackled by utilizing already known properties of the Green's function. We can analytically calculate the value of the integral of the zeroth order term of the expansion of G

$$I_0(k,\mu) = \int_0^{\tau_{\max}} \mathrm{d}\tau\, G_0(k,\tau,\mu) \tag{3.3}$$

$$= \int_0^{\tau_{\max}} \mathrm{d}\tau\, e^{-(\varepsilon(k)-\mu)\tau} \tag{3.4}$$

$$= \frac{1 - e^{-(k^2/2-\mu)\tau_{\max}}}{k^2/2 - \mu} \tag{3.5}$$

If we count how many times we have visited the zeroth order diagram while running the simulation N_0, then we get the normalization factor for the ith bin of the histogram

$$c_i(k,\mu) = \frac{\delta\tau_i I_0(k,\mu)}{N_0} \tag{3.6}$$

where $\delta\tau_i$ is the width of bin i and we can successfully recover the normalized quantity by multiplying

$$Q(\tau_i) = c_i(k,\mu) Q_{\text{MC}}(\tau_i). \tag{3.7}$$

It has to be noted that Eq. 3.3 prohibits a simulation run for the pole of the denominator where $k^2/2 - \mu = 0$. Defining $x \equiv k^2/2 - \mu$ and investigating the limit further with L'Hopital's rule we obtain

$$I_0(k,\mu) = \lim_{x\to 0} \frac{1 - e^{-x\tau_{\max}}}{x} = \lim_{x\to 0} \tau_{\max} e^{-x\tau_{\max}} = \tau_{\max} \tag{3.8}$$

for this special case.

3.4 Histogram method

The histogram method is straightforward. As explained in the previous section, a predefined interval $[0, \tau_{\max}]$ is split into M bins $b_i = [\tau_i, \tau_{i+1})$ of arbitrary width $\delta\tau_i = \tau_{i+1} - \tau_i$. Let's assume the simulation has run for N steps and we collect statistics after every step. When measuring the Green's function—or any other

continuous observable for that matter—the bin b_i is incremented by one if the current diagram length τ lies between its bounds

$$b_i^N = b_i^{N-1} + \delta(\min(b_i) \leq \tau < \max(b_i)). \tag{3.9}$$

For histograms, it is crucial to note that an increase in bin width reduces statistical fluctuations as more samples can be collected per bin. However, this comes not without cost. Histograms are distorted by systematic errors that arise from the finite width of each bin. Decreasing the number of bins causes an inherent increase in these systematic errors, see Fig. 3.2. An everlasting contest between minimizing statistical

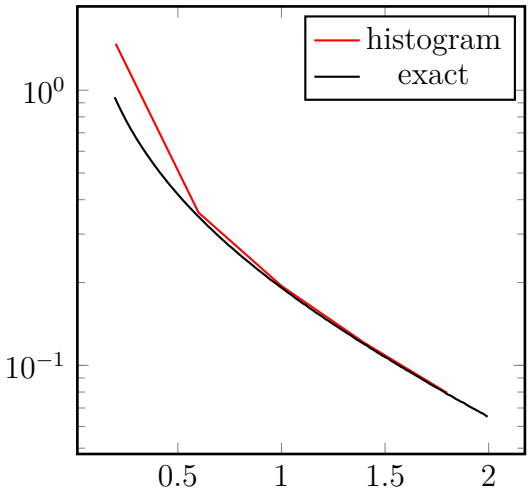

Figure 3.2: The effect of a low bin count for histograms must be considered, especially in regions where the second derivative of the measured entity has high absolute values.

and systematic errors is ensured. One can quickly demonstrate how critical this error is for the bin $[a, b)$ and a hypothetical function $f(x) = e^{-\alpha x}$ — the nature of the function allows us to *bend* the function to increase the systematic error. Since the area of the histogram and the area of the function on the domain $[a, b)$ must be equal it is readily given that the x-value where the histogram intersects the function x_0 and the height h of the bin is

$$\begin{aligned} x_0 &= \frac{1}{\alpha}\left(\ln(\alpha(b-a)) - \ln(e^{-\alpha a} - e^{-\alpha b})\right), \\ h &= \frac{e^{-\alpha a} - e^{-\alpha b}}{\alpha(b-a)}, \end{aligned} \tag{3.10}$$

from which we can plot the error $\Delta y = h - f(x)$ for the first bin in a DMC calculation e.g. $[0, 1)$, which is excessively big for demonstration purposes. The result is visualized in Fig. 3.3.

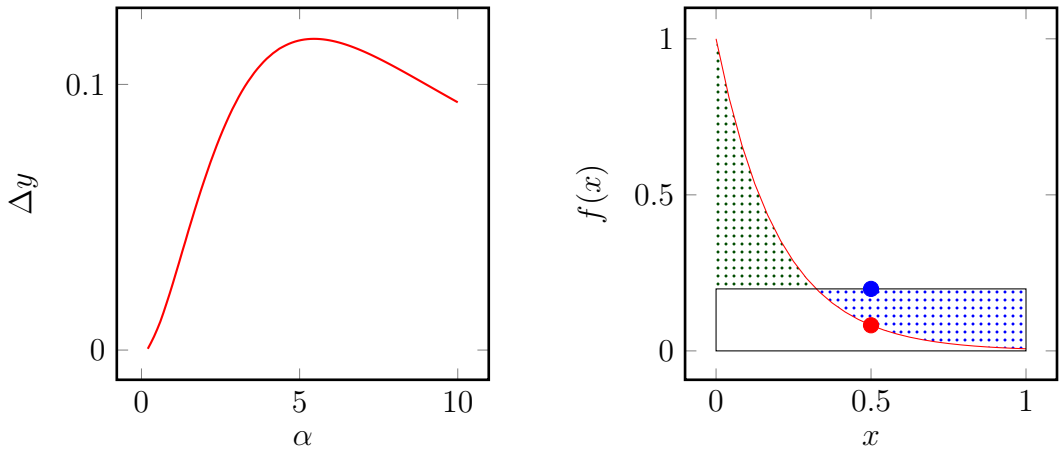

Figure 3.3: On the left the systematic error $\Delta y(\alpha)$ of the histogram can be seen for the bin $[0, 1)$. It might be surprising to see that the errors exhibit a global maximum. This is due to $f(x)$ getting increasingly *flat* for high α, resulting in the function value and the actual bin height at $x = 0.5$ both going to zero for $\alpha \to \infty$. Associating each bin with its middle value when plotting, results in the number of samples collected in the left half of the bin being greater if the measured function $f(x)$ has a positive second derivative $f''(x) > 0$ (right, $\alpha = 5$). This leads to the y-value of the histogram bin (blue dot) being *overestimated* as the bin value will be the average of its domain, while the actual value of the function (red) lies to the bottom. The blue and green areas must be equal (for an infinitely long sampling time).

3.5 Statistical Error Analysis

Each MC algorithm features pseudorandom number generators. Putting aside the fact that pseudo random number generators (PRNGs) are by construction, not actual random devices, there is another issue that arises when using random numbers. As with all statistical algorithms, the influence of statistical errors must be analyzed and interpreted accordingly. In the case of a (self-energy) DMC calculation of the Fröhlich polaron, we have to determine which quantities' error needs to—or rather, can be—approximated meaningfully. In one run the output is usually the following:

- ground state energy E_0 (scalar)
- quasi-particle weight Z_0 (scalar)
- effective mass m_* (scalar) or group velocity $\mathbf{v}(\mathbf{k})$ (vector)
- proper self-energy Σ (histogram)
- full one-particle Green's function $\mathbf{G}$ (histogram)

For scalar and vectorial quantities where the result is just the average $\overline{A}$ over the collected samples A_i

$$\overline{A} = \frac{1}{M} \sum_{i=1}^{M} A_i \tag{3.11}$$

or an average of a function of the data (an example represents the estimator of the quasi-particle weight Z_0 in Section 3.7.2) an estimation of the error can be given by prominent statistical tools like bootstrap or jackknife. The theory behind resampling methods exceeds the scope of this thesis and we refer the reader to [32]. They require that the input data is uncorrelated, which can be achieved by only measuring once every n_{steps} updates. The optimal value of this variable depends heavily on the specific simulation and the used parameters. A cautious guideline is to choose

$$n_{\text{steps}} \geq 2\tau_{\text{int}}, \tag{3.12}$$

where the integrated autocorrelation time τ_{int} describes the time it takes the system to reach a new independent and uncorrelated configuration. For DMC calculations it effectively suffices to reach the 0^{th} order diagram to decorrelate the samples. For higher α values we therefore have to use more elementary DMC steps between measurements. Histograms require additional attention in the sense that each bin must be treated as an isolated observable.

3.6 Bare Green's function DMC

3.6.1 Estimators

Some quantities which we are ultimately interested in are—among others—the ground state energy E_0, the Z-factor and the effective mass m_*. Normally, one would generate the Green's function via DMC and do an exponential fit for the high-τ region to get both E_0 and Z. While useful, if we are already collecting the Green's function, this is not entirely necessary. We can employ another method to directly collect statistics for these observables. Let's assume we seek some quantity A which is given by the diagrammatic expansion

$$A = \overline{\sum_{\nu}} \mathcal{D}_{\nu}^{(A)} \tag{3.13}$$

where the special sum $\overline{\sum_{\nu}}$ reflects that it incorporates summing over discrete as well as integrating over continuous internal variables that are grouped into a compound ν which indexes all diagrams $\mathcal{D}_{\nu}^{(A)}$ of A. The general idea is now that—given another function $B = \overline{\sum_{\nu}} \mathcal{D}_{\nu}^{(B)}$—one is able to express the ratio of these quantities via the

ratios of their diagrams

$$\frac{B}{A} = \frac{1}{M}\sum_{\{\nu\}} \mathcal{Q}_\nu \tag{3.14}$$

$$\mathcal{Q}_\nu = \frac{\mathcal{D}_\nu^{(B)}}{\mathcal{D}_\nu^{(A)}} \tag{3.15}$$

where M is the size of the accumulated set of ν's during the DMC run [24]. As we will see below, applying an infinitesimal perturbation to one of the external variables and using Eq. 3.15 we can derive direct estimators for a number of quantities. In a real DMC simulation we would only need to generate diagrams according to $\mathcal{D}_\nu^{(A)}$ while employing these direct estimators to collect statistics.

Direct estimator for the ground state energy E_0

We start off by calculating Eq. 3.15 for the usual diagrams

$$\mathcal{Q} = \frac{\mathcal{D}(n, \mathcal{T}; \{\mathbf{x}\}; \mathbf{k}, (1+\lambda)\tau)}{\mathcal{D}(n, \mathcal{T}; \{\mathbf{x}\}; \mathbf{k}, \tau)} \tag{3.16}$$

$$= (1+\lambda)^{2n}\left(\prod_j \exp(-\lambda\varepsilon(\boldsymbol{k}_j)\Delta\tau_j)\right)\left(\prod_l \exp(-\lambda\omega_0\Delta\tau_l)\right) \tag{3.17}$$

where $\prod_j$ goes over all electron lines with momenta $\boldsymbol{k}_j$, $\prod_l$ goes over all phonon lines, n stands for the diagram order and $\Delta\tau_j$ and $\Delta\tau_l$ are the imaginary time durations of the electron and phonon propagators, respectively. Beware that here $2n$ is equal to the number of interaction vertices, i.e. the number of integrations over internal times. By noting that

$$\lim_{\tau\to\infty} \frac{G(k, (1+\lambda)\tau)}{G(k,\tau)} = e^{-\lambda E(k)\tau} \tag{3.18}$$

and expanding Eq. 3.16 and Eq. 3.18 up to first order in the limit $\lambda \to 0$

$$\mathcal{Q} = e^{-\lambda E_0(k)\tau} \tag{3.19}$$

$$1 + \lambda\left(2n - \sum_j \varepsilon(\boldsymbol{k}_j)\Delta\tau_j - \sum_l \omega_0\Delta\tau_l\right) + \mathcal{O}(\lambda^2) = 1 - \lambda E_0(k)\tau + \mathcal{O}(\lambda^2) \tag{3.20}$$

it becomes lucid that an estimator for the ground state energy E_0 is given by

$$\langle E_0(\{\mathbf{y}\})\rangle_{\mathrm{MC}} = \lim_{\tau\to\infty} \frac{1}{M}\sum_m^M \frac{1}{\tau_m}\left(-2n_m + \sum_j \varepsilon(\boldsymbol{k}_j)\Delta\tau_j + \sum_l \omega_0\Delta\tau_l\right). \tag{3.21}$$

One must be careful not to mistake τ_m for the τ-value of an internal vertex [24].

Direct estimator for the effective mass and group velocity

The derivation of the effective mass estimator follows a similar pattern as the one for the ground state energy. The effective mass is defined as

$$m_*(\alpha) = \left[\frac{\mathrm{d}^2 E_0(k,\alpha)}{\mathrm{d}k^2}\right]^{-1}_{k=0}. \tag{3.22}$$

Perturbing the momentum instead of the imaginary time we get

$$\lim_{\substack{\tau\to\infty\\ \lambda\to 0}} \frac{G(k+\lambda\hat{\mathbf{e}},\tau)}{G(k,\tau)} = \begin{cases} \exp(-\lambda^2\tau/2m_*), & k=0 \\ \exp(-\lambda\hat{\mathbf{e}}\mathbf{v}(k)\tau), & k\neq 0 \end{cases} \tag{3.23}$$

whereas the diagram ratio is given by

$$\mathcal{Q} = \prod_j \exp\left(-\frac{1}{2}\left[(\boldsymbol{k}_j+\lambda\hat{\mathbf{e}})^2 - \boldsymbol{k}_j^2\right]\Delta\tau_j\right). \tag{3.24}$$

Expanding Eq. 3.24 in the limit $\lambda \to 0$ up to second order we get

$$\mathcal{Q} = 1 - \lambda\tau(\hat{\mathbf{e}}\overline{\boldsymbol{k}}) - \frac{\lambda^2}{2}\tau + \frac{\lambda^2}{2}\tau^2(\hat{\mathbf{e}}\overline{\boldsymbol{k}})^2 + \mathcal{O}(\lambda^3) \tag{3.25}$$

where

$$\overline{\boldsymbol{k}} = \frac{1}{\tau}\sum_j \boldsymbol{k}_j\Delta\tau_j \tag{3.26}$$

is the mean momentum of the electron propagators of the diagram. Expanding Eq. 3.23 as well and comparing leads to the estimators for the effective mass m_* and the group velocity $\mathbf{v}(\mathbf{k})$ [24]:

$$\langle \mathbf{v}(\mathbf{k})\rangle_{\mathrm{MC}} = \lim_{\tau\to\infty}\overline{\boldsymbol{k}} \tag{3.27}$$

$$\langle m_*^{-1}\rangle_{\mathrm{MC}} = \lim_{\tau\to\infty} 1 - \frac{\tau}{3}\overline{\boldsymbol{k}}^2 \tag{3.28}$$

Exact Estimators

For quantities that resemble functions, such as the Green function, we can apply the histogram approach. However, due to the substantial errors—inherent to the divergence in the $\tau \to 0$ region—we search for an exact estimator for the Green function. That is, an estimator free of systematic errors described in Fig. 3.3. In [24] such an estimator has been proposed. The Ansatz is the following. During a DMC run when collecting a sample of the current diagram, the diagram length might fall not exactly on the j^{th} bin's middle value $\tau_{j,0}$ but somewhere else inside the bin $[\tau_0 - \frac{\Delta\tau_0}{2}, \tau_0 + \frac{\Delta\tau_0}{2}]$. Instead of simply incrementing the bin counter, we then try to account for the fact that the collected value τ has an offset to the bin value. The

idea is to take the exact relation and multiply it by unity by appending an additional integral

$$Q(\tau_0) = \int \mathrm{d}\tau_1 \ldots \int \mathrm{d}\tau_{2n}\, \mathcal{D}(\tau_1, \ldots, \tau_{2n}; \tau_0) \underbrace{\int_0^{\tau_{\max}} \mathrm{d}\tau\, \frac{\mathcal{D}(\eta_1, \ldots, \eta_{2n}; \tau)}{\mathcal{D}(\eta_1, \ldots, \eta_{2n}; \tau)} \frac{1}{\Delta\tau_0} \xi_{\Gamma_0}(\tau)}_{=1} \tag{3.29}$$

where

$$\xi_{\Gamma_0}(\tau) = \begin{cases} 1, & \tau \in \Gamma_0 \\ 0, & \text{else} \end{cases} \tag{3.30}$$

is an indicator function whether τ lies inside the bin with width $\Delta\tau_0$ and we defined a rescaled quantity that represents the aforementioned offset

$$\eta_i(\tau_i) = \frac{\tau}{\tau_0}\tau_i \equiv s\tau_i. \tag{3.31}$$

We can rewrite

$$Q(\tau_0) = \int_0^{\tau_{\max}} \mathrm{d}\tau \int \mathrm{d}\eta_1 \ldots \int \mathrm{d}\eta_n\, s^{2n} \frac{\mathcal{D}(\frac{\eta_1}{s}, \ldots, \frac{\eta_{2n}}{s}; \tau_0)}{\mathcal{D}(\eta_1, \ldots, \eta_{2n}; \tau)} \mathcal{D}(\eta_1, \ldots, \eta_{2n}; \tau) \frac{1}{\Delta\tau_0} \xi_{\Gamma_0}(\tau) \tag{3.32}$$

Renaming the integration variables and introducing a normalization constant yields

$$Q(\tau_0) = C \int_0^{\tau_{\max}} \mathrm{d}\tau \int \mathrm{d}\tau_1 \ldots \int \mathrm{d}\tau_{2n}\, a_{\tau_0,\mathrm{MC}}(\tau, \tau_0, \{\tau_i\}) \frac{\mathcal{D}(\tau_1, \ldots, \tau_{2n}; \tau)}{C} \tag{3.33}$$

where we have defined the final *exact estimator*

$$a_{\tau_0,\mathrm{MC}}(\tau, \tau_0, \{\tau_i\}) = s^{2n} \frac{\mathcal{D}(\frac{\tau_1}{s}, \ldots, \frac{\tau_{2n}}{s}; \tau_0)}{\mathcal{D}(\tau_1, \ldots, \tau_{2n}; \tau)} \frac{1}{\Delta\tau_0} \xi_{\Gamma_0}(\tau). \tag{3.34}$$

The diagram ratios are given by

$$\frac{\mathcal{D}(\frac{\tau_1}{s}, \ldots, \frac{\tau_{2n}}{s}; \tau_0)}{\mathcal{D}(\tau_1, \ldots, \tau_{2n}; \tau)} = \exp\left[\left(1 - \frac{1}{s}\right)\left(\sum_j \varepsilon(\boldsymbol{k}_j)\Delta\tau_j + \sum_l \omega_0 \Delta\tau_l\right)\right] \tag{3.35}$$

Using this estimator allows us to increase the bin size without the systematic error that is inherent to the crude histogram approach.

3.6.2 Updates: Preparation

Updates are the heart and soul of every DMC algorithm. They enable the object of interest to walk through configuration space randomly. All updates have things in common. They select a certain property of the diagram, propose a change of the diagram based upon this choice, and finally return a positive definite number, which

determines the chances of adoption of the proposed changes. Generally for DMC, we distinguish between two kinds of updates.

Type-I updates leave the number of integration variables unchanged. There is no lack thereof since they are already deployed in numerous classical MC schemes. Changes in local parameters and topology fall into this category. With a low computational footprint in mind, these updates apply just the simplest possible changes to the diagram. Typical examples include altering the global length of the diagram τ, the direction or modulus of phonon momenta or the internal imaginary time τ_i of the i^{th} vertex. The values and the acceptance rate of these updates heavily depend upon the proposal distributions. For example, a change in diagram time might simply be drawn from an exponential distribution, which is quite simple to implement and achieves an acceptance ratio of unity. For more complicated updates computational efficiency must not be sacrificed for the sake of high acceptance rates. One has to find a compromise between simplicity and efficacy.

Updates of type-II either increase or decrease the diagram order by an integer m. The easiest to implement are the ones where $m \in \{-1, 1\}$. Type-II updates require that either additional variables are proposed (add phonon propagator) or that existing variables are deleted (remove phonon propagator).

How to set up the detailed balance equation and which proposal distributions are used will be discussed for each update separately. One might now ask why it is allowed to treat every point in configuration space with the same weight, despite them having a differing number of integrations. This question is answered by looking again at the integrals of $Q(\mathbf{y})$. When adding a phonon branch, the new variables $\mathbf{x}_{n+1}$ are drawn from a normalized probability density function $f_\nu(\mathbf{x}_{n+1})$. This function is arbitrary and influences the acceptance ratio of the update. If one now replaces the value of this function with unity in the acceptance ratio, we have to treat it explicitly in the integrals:

$$\int \mathrm{d}\mathbf{x}_1 \ldots \int \mathrm{d}\mathbf{x}_n \underbrace{\int \mathrm{d}\mathbf{x}_{n+1}\, f_\nu(\mathbf{x}_{n+1})}_{\mathcal{A}} \mathcal{D}_\nu. \tag{3.36}$$

If we now use that this normalization integral $\mathcal{A}$ equates to unity for other updates

$$\int \mathrm{d}\mathbf{x}_1 \ldots \int \mathrm{d}\mathbf{x}_n \underbrace{\int \mathrm{d}\mathbf{x}_{n+1}\, f_\nu(\mathbf{x}_{n+1})}_{\mathcal{A}} \mathcal{D}_\nu = \int \mathrm{d}\mathbf{x}_1 \ldots \int \mathrm{d}\mathbf{x}_n\, 1 \times D_\nu \tag{3.37}$$

we have shown that it is possible to reduce type-II to type-I updates, which is exactly why we can treat all diagrams—and thus, all points in configuration space—in the same way [27].

One of the most defining characteristics of the efficiency of updates is the acceptance ratio R. In the following sections, we will list the *eight* different types of updates that have been utilized in this thesis. To enable complete comprehension of how these updates work, we will show how to calculate/estimate the acceptance probabilities for each. Essentially, this involves two steps: First, one calculates the

ratio $\frac{\mathcal{D}_{\nu'}}{\mathcal{D}_\nu}$between the diagram before $\mathcal{D}_\nu$ and after $\mathcal{D}_{\nu'}$ the update. Secondly, we need to propose a probability density $P(\mathbf{x})$ from which we draw the (new) internal variables $\mathbf{x}$. Then we can write the acceptance rates for type-I updates as

$$R_{\nu\to\nu'} = \left|\frac{\mathcal{D}_{\nu'}}{\mathcal{D}_\nu}\right| \frac{P(\mathbf{x})}{P(\mathbf{x}')} \frac{\mathrm{d}\mathbf{x}'}{\mathrm{d}\mathbf{x}} \tag{3.38}$$

and for type-II updates as

$$R_{\nu\to\nu'} = \frac{u_{n\to n+m}}{u_{n+m\to n}} \left|\frac{\mathcal{D}_{\nu'}}{\mathcal{D}_\nu P(\nu; \mathbf{x}_{n+1}, \ldots, \mathbf{x}_{n+m})}\right| \tag{3.39}$$

where $u_{n\to n+m}$ and $u_{n+m\to n}$ are probabilities specific to the algorithms we will introduce, see Section 3.6.4. For the special case of the Fröhlich polaron the diagram weights are always positive definite, so we can omit the absolute value operator. As a result, the cumbrous sign problem is eliminated. All of the following updates have been extracted from [27] for their good performance, albeit some of them have been slightly modified.

3.6.3 Type-I Updates

Change global τ

For this update, we will be verbose when doing calculations so that the procedure can be understood easily. For the next updates, the basic steps will be skipped. This update is by far the easiest to implement and explain. Suppose we have a diagram with global length τ, we propose a new τ' from the probability density

$$P(\tau') = \frac{E e^{-E(\tau'-\tau_{2n})}}{1 - e^{-E(\tau_{\max}-\tau_{2n})}} \tag{3.40}$$

$$E = \begin{cases} \varepsilon(k) - \mu + \Omega & \text{if a phonon propagator is modified (self-energy DMC)} \\ \varepsilon(k) - \mu & \text{else (bare DMC)} \end{cases} \tag{3.41}$$

where we have distinguished whether a phonon propagator has also been stretched or shortened in the process. A visual illustration of the update can be seen in Fig. 3.4.

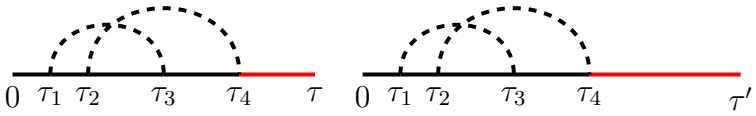

Figure 3.4: Diagram before (left) and after (right) the change-τ update.

Anticipating Section 3.7, we note that for self-energy DMC calculations the diagram has been stripped of the start and end electron propagators. This enters

into the above equation as there is another term Ω for the change in phonon energy to account for. Inverse transform sampling can be used to directly sample from the exponential $P(\tau')$ by generating a uniform, random number $r = U(0,1)$ and using

$$\tau' = \tau_{2n} - \frac{1}{E} \ln \Big\{ 1 - r \Big[1 - \exp\big(- E(\tau_{\max} - \tau_{2n}) \big) \Big] \Big\}. \tag{3.42}$$

The probability density resulting from this generation method is actually cut off at $\tau_{\max}$ so that we don't accidentally propose a diagram that has a length beyond the maximum allowed $\tau_{\max}$. Next, we calculate the diagram ratios. Since we only change one vertex they only depend on the changed τ value and the energy of the electron (and phonon) propagator—though, the phonon propagator is only relevant when doing self-energy DMC, when the first and last electron lines are missing. The diagram ratio evaluates to

$$\begin{aligned}
\frac{\mathcal{D}_{\nu'}}{\mathcal{D}_{\nu}} =& \frac{G_0(\tau_1, \boldsymbol{k}_1) G_0(\tau_2 - \tau_1, \boldsymbol{k}_2) G_0(\tau_3 - \tau_2, \boldsymbol{k}_3) G_0(\tau_4 - \tau_3, \boldsymbol{k}_4) G_0(\tau - \tau_4, \boldsymbol{k}_5)}{G_0(\tau_1, \boldsymbol{k}_1) G_0(\tau_2 - \tau_1, \boldsymbol{k}_2) G_0(\tau_3 - \tau_2, \boldsymbol{k}_3) G_0(\tau_4 - \tau_3, \boldsymbol{k}_4) G_0(\tau' - \tau_4, \boldsymbol{k}_5)} && (3.43) \\
& \frac{D_0(\tau_3 - \tau_1, q_1) D_0(\tau_4 - \tau_2, q_2)}{D_0(\tau_3 - \tau_1, q_1) D_0(\tau_4 - \tau_2, q_2)} && (3.44) \\
=& \frac{G_0(\tau - \tau_4, \boldsymbol{k}_5)}{G_0(\tau' - \tau_4, \boldsymbol{k}_5)} && (3.45) \\
=& \exp\big(- E\big[(\tau' - \tau_4') - (\tau - \tau_4) \big] \big) && (3.46) \\
=& \exp\big(- E(\tau' - \tau) \big) && (3.47)
\end{aligned}$$

where we can see that only the F-lines that had their properties changed contribute to the diagram ratios. For the upcoming updates, we can therefore simply omit the unchanged parts of the diagram and focus on the updated ones. The ratio of probability densities equates to

$$\frac{P(\tau')}{P(\tau)} = \exp\Big(- E(\tau' - \tau) \Big) \tag{3.48}$$

and thus the acceptance ratio is unity

$$R_{\nu \to \nu'} = \left| \frac{\mathcal{D}_{\nu'}}{\mathcal{D}_{\nu}} \right| \frac{P(\tau)}{P(\tau')} = 1. \tag{3.49}$$

An acceptance rate of one is the exception as we will see for most of the next updates. Theoretically, this and the two type-II updates are the only ones needed to satisfy ergodicity. However, we provide a handful of other type-I updates since they improve convergence speed, reduce autocorrelations and are fun to evaluate and program.

Change internal τ

Similar to the change-global-τ update we change the τ value of a vertex, but this time we select an internal one instead of the last one. Thus, the external variables of

the diagram are left unchanged. We propose an update where we select at random one of the $2n$ inner vertices τ_j and modify its time to lie in between (τ_{j-1}, τ_{j+1}) with the probability density

$$P(\tau_i') = \frac{E e^{-E(\tau_i' - \tau_{i-1})}}{1 - e^{-E(\tau_{i+1} - \tau_{i-1}}} \tag{3.50}$$

$$E = \frac{\boldsymbol{k}_{i-1}^2 - \boldsymbol{k}_i^2}{2M} \pm \Omega \tag{3.51}$$

where the sign of Ω depends on whether the selected vertex has an incoming $(+)$ or outgoing $(-)$ phonon propagator. The schematic process of the update is displayed in Fig. 3.5.

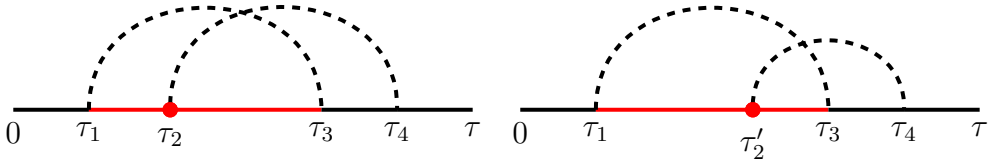

Figure 3.5: Diagram before (left) and after (right) the change-internal-τ update. Here we select the vertex at τ_2 and propose a new imaginary time $\tau_2' \in (\tau_1, \tau_3)$ (red line).

Analoguously, to the change-τ update, the ratio of acceptance is also unity here:

$$R_{\nu \to \nu'} = \left| \frac{\mathcal{D}_{\nu'}}{\mathcal{D}_\nu} \right| \frac{P(\tau_i)}{P(\tau_i')} = e^{-E(\tau_i' - \tau_i)} e^{-E(\tau_i - \tau_i')} = 1. \tag{3.52}$$

Rescale diagram

Since the electron propagators are independent and identically distributed (i.i.d.) random variables we can infer that the dependence of the diagram on the global time τ takes the form of the Poisson distribution

$$P(\tau') = \frac{E(E\tau')^{2n}}{(2n)!} e^{-E\tau'} \tag{3.53}$$

$$E = \sum_{j=1}^{2n+1} \Delta s_j E_j - \mu, \tag{3.54}$$

where we introduced dimensionless rescaled times with the scaling constant η

$$s_i = \frac{\tau_i}{\tau}, \tag{3.55}$$

$$\Delta s_i = s_{i+1} - s_i = \frac{\Delta \tau_i}{\tau}, \tag{3.56}$$

$$\eta = \frac{\tau'}{\tau} \tag{3.57}$$

and the energy per time interval E_i is composed of both all the phonon as well as the electron energies on that interval. Alas, inverse transform sampling cannot be applied to this distribution. Therefore we switch over to the easily usable Gaussian

$$P(\tau') = \frac{E}{\sqrt{4\pi n}} e^{-(E\tau'-2n)^2/4n}, \tag{3.58}$$

which resembles the Poisson distribution well for $E\tau \gg 1, n \gg 1$. For values that violate the rules of the simulation run, such as $\tau' > \tau_{\max}$, the update is rejected. An illustration of this update can be found in Fig. 3.6. The diagram ratio evaluates to

$$\frac{\mathcal{D}_{\nu'}}{\mathcal{D}_{\nu}} = \prod_{j=1}^{2n+1} \frac{G_0(\eta\Delta\tau_j)}{G_0(\Delta\tau_j)} \prod_{l=1}^{n} \frac{D_0(\eta\Delta\tau_l)}{D_0(\Delta\tau_l)} \prod_{r=1}^{2n} \frac{\mathrm{d}\tau'_r}{\mathrm{d}\tau_r} \tag{3.59}$$

$$= \frac{\tau'}{\tau}^{2n} \exp\left[-\sum_{j=1}^{2n+1} (\varepsilon(\boldsymbol{k}_j) - \mu)(\tau' - \tau)\Delta s_j - \omega_0 \sum_{l=1}^{n} (\tau' - \tau)\Delta s_l \right] \tag{3.60}$$

$$= \exp\left[2n \ln \frac{\tau'}{\tau} - E(\tau' - \tau) \right] \tag{3.61}$$

where

$$E = \sum_{j}^{2n+1} E_j \Delta s_j - \mu \tag{3.62}$$

is the full energy contribution and E_j is the part of the energy that is covered by each interval, both phononic and electronic. With this probability distribution, the acceptance ratio reads

$$R_{\nu\to\nu'} = \exp\left(2n \ln \frac{\tau'}{\tau} - E(\tau' - \tau) + \frac{(E\tau' - 2n)^2 - (E\tau - 2n)^2}{4n} \right). \tag{3.63}$$

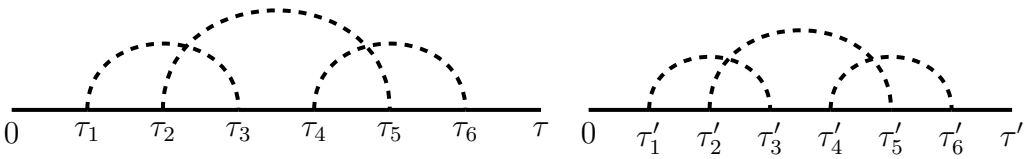

Figure 3.6: Diagram before (left) and after (right) the *rescale-diagram* update.

Change phonon momentum modulus

We select one of the n phonon propagators randomly whose momentum modulus is subject to change while its direction is being preserved. Suppose the phonon

propagator goes from τ_a to τ_b, for proposing a new value q' for $q = |\mathbf{q}|$ we use the Gaussian density

$$P(q') = \frac{1}{\sqrt{2\pi\sigma_q^2}} e^{-(q'-\mu_q)^2/2\sigma_q^2}, \tag{3.64}$$

$$\mu_q = \langle \boldsymbol{k} \rangle \cdot \hat{\mathbf{e}}_q, \tag{3.65}$$

$$\sigma_q = \frac{M}{\tau_b - \tau_a}, \tag{3.66}$$

$$\langle \boldsymbol{k} \rangle = \frac{1}{\tau_b - \tau_a} \int_{\tau_a}^{\tau_b} \mathrm{d}\tau \, (\boldsymbol{k}(\tau) + \mathbf{q}). \tag{3.67}$$

Here, $\langle \boldsymbol{k} \rangle$ is the average momentum of the electron propagator on the interval $[\tau_a, \tau_b]$ in the *absence* of the selected phonon propagator and $\hat{\mathbf{e}}_q$ is the unit vector of the phonon momentum. Luckily, the proposed density $P(q')$ is reproducing the exact diagram ratios and thus, this update has an acceptance ratio of unity. A visualization is given in Fig. 3.7.

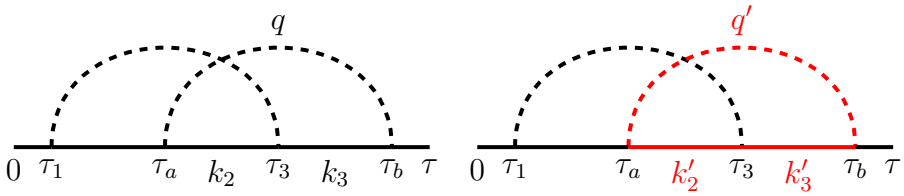

Figure 3.7: Diagram before (left) and after (right) the *change-q-modulus* update.

One must not forget to update the electron line momenta between τ_a and τ_b after accepting the update to preserve the global momentum. This update is subject to frequent numerical "errors" as the selected proposal distribution allows negative values for q' and might produce `NaN` values when the mean and/or the standard deviation of the distribution are unstable, e.g. too small time intervals between τ_b and τ_a so that *catastrophic cancellation* occurs.

Change phonon momentum direction

The change in phonon momentum direction, see Fig. 3.8, is similar to the change in modulus of the momentum.

We select at random one of the n phonon propagators that goes from τ_a to τ_b and propose a new direction of the vector while keeping its modulus fixed. The proposal distribution for the new direction is given by

$$P(\varphi, \theta) = \frac{A \sin(\theta)}{4\pi \sinh(A)} e^{A\cos(\theta)} \tag{3.68}$$

$$A = \frac{\tau_b - \tau_a}{M} q \, |\langle \boldsymbol{k} \rangle| \tag{3.69}$$

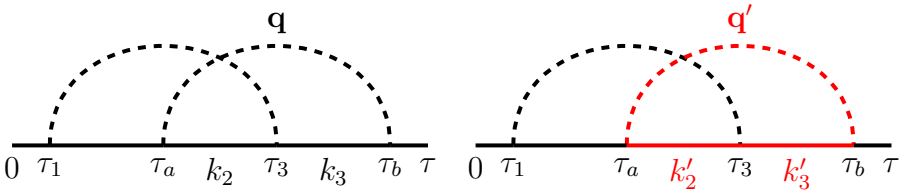

Figure 3.8: Diagram before (left) and after (right) the *change-q-direction* update.

The average electron momentum $\langle \boldsymbol{k} \rangle$ is defined equally as in the change phonon momentum modulus update. The azimuthal angle φ and the polar angle θ are both defined relative to the axis of $\langle \boldsymbol{k} \rangle$. The acceptance ratio of this update is also unity since the proposal density exactly mimics the diagram weights. The electron momenta must be taken care of like so

$$\boldsymbol{k}_i' = \boldsymbol{k}_i + \mathbf{q} - \mathbf{q}' \tag{3.70}$$

should the update be accepted.

Change topology

Here, a *topology change* refers to a simple switch of two nearest-neighboring vertices. With the help of this update, the diagram can easily travel and visit all the topology variations of a given order in a finite amount of time. To accomplish this we select at random any n.n.-pair of vertices τ_a and τ_b and swap them so that the phonon propagator of each vertex now points to the other vertex. The phonon momenta are kept fixed. If the two vertices connect to the same phonon line then—depending on the implementation details—either nothing happens or the phonon momentum changes sign. The update can be seen in Fig. 3.9.

Should the update be accepted then the momentum of the electron F-line connecting the two vertices changes to

$$\boldsymbol{k}' = \boldsymbol{k} + \mathbf{q}_a - \mathbf{q}_b. \tag{3.71}$$

As there are no probability densities involved in selecting new variables the acceptance ratio is equal to the diagram ratio

$$R_{\nu \to \nu'} = \exp\left\{ -(\tau_b - \tau_a) \Big[\varepsilon(\boldsymbol{k}') - \varepsilon(\boldsymbol{k}) \pm \chi \omega_0 \Big] \right\} \tag{3.72}$$

where

$$\chi = \begin{cases} 0, & \text{if both are incoming or outgoing} \\ 2, & \text{if } \tau_a \text{ is incoming and } \tau_b \text{ is outgoing} \\ -2, & \text{if } \tau_a \text{ is outgoing and } \tau_b \text{ is incoming} \end{cases} \tag{3.73}$$

is a function that handles the four possible configurations out-out, in-out, out-in and in-in of the phonon propagators, see Fig. 3.9. In comparison to other type-I updates,

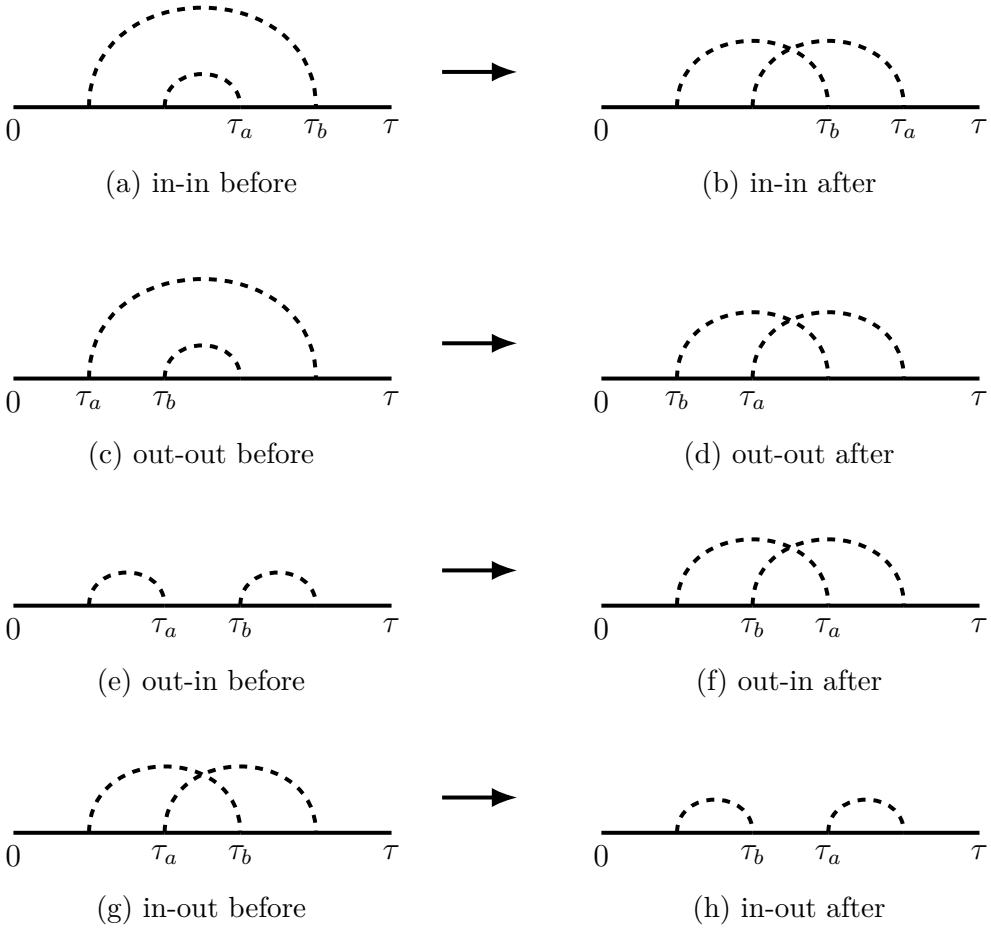

Figure 3.9: The four different possible configurations of the *change-topology* update.

the *change-topology* update is kept rather local, such that it can be executed in constant time, whereas e.g. for the *change-phonon-momentum-direction* update one needs to iterate over all F-lines in the worst case.

3.6.4 Type-II Updates

For the updates of type-II, we have previously noted that we change the order of the diagram and thus, introduce (remove) new (old) internal variables to the diagram. This is done in such a way that the diagram may grow as large as $n_{\max}$ or as low as $n = 0$. Together with the *change-τ* type-I update the following two updates would satisfy the requirement of ergodicity, as different topologies within one order can be generated simply by adding/removing phonon lines. This is only the case if the *add-phonon* update is applied so that the new phonon propagator does *not* necessarily start and end on the same electron line, though this might often be the case.

Add phonon

For a better overview of the following discussion please refer to Fig. 3.10 for visual guidance. When adding a phonon line we need two determine a few parameters: where does it start/end and what momentum $\mathbf{q}$ does it have? The latter one is fairly simple. We just need to propose a probability distribution

$$P(\varphi, \theta, q) = \frac{\sin(\theta)}{4\pi} \frac{1}{p_0(1+q/p_0)^2} \tag{3.74}$$

$$p_0 = \sqrt{2M\Omega} \tag{3.75}$$

and apply inverse transform sampling to obtain a new $\mathbf{q}'$. The density $P(\varphi, \theta, q)$ is uniform for the azimuthal angle φ.

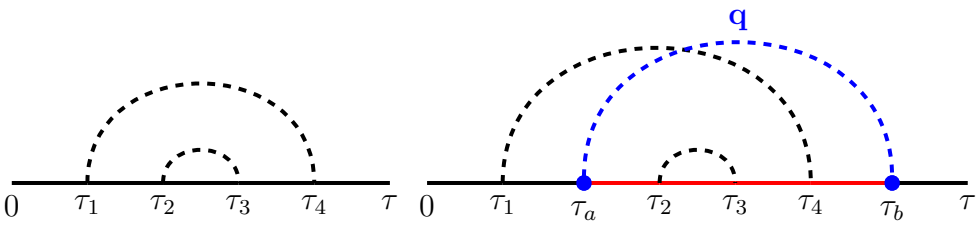

Figure 3.10: Diagrams before (left) and after (right) the *add phonon* update. The blue parts of the diagram mark newly generated variables, while red lines signify that some property has changed upon insertion of the phonon line.

Generating a new τ_a and τ_b involves a couple more steps. First, the algorithm randomly picks one of the phonon propagators with variables $(\tau_1, \tau_2, \boldsymbol{k})$. The first new vertex's imaginary time is generated uniformly

$$P(\tau_a) = \begin{cases} \frac{1}{\Delta\tau}, & \tau_1 < \tau_a < \tau_2 \\ 0 & \text{else} \end{cases} \tag{3.76}$$

$$\tau_a = \tau_1 + U(\Delta\tau) \tag{3.77}$$

where $\Delta\tau = \tau_2 - \tau_1$. The time of the second vertex is—again—drawn from an exponential density

$$P(\tau_b) = \Omega \left(1 + \frac{q}{p_0}\right)^2 \exp\left\{-\Omega \left(1 + \frac{q}{p_0}\right)^2 (\tau_b - \tau_a)\right\} \tag{3.78}$$

where illegal proposals—e.g. $\tau_b > \tau_{\max}$—have been again filtered out by using the truncated density. Albeit the joined proposal distribution is not a perfect match for the diagram ratio

$$\left|\frac{\mathcal{D}_{\nu'}}{\mathcal{D}_{\nu}}\right| = |g(q)|^2 \, e^{-\Delta E(\tau_b - \tau_a)} \frac{q^2 sin(\theta)}{(2\pi)^3} \propto e^{-\Delta E(\tau_b - \tau_a)} \sin(\theta) \tag{3.79}$$

it still delivers quite acceptable performance on average ($R \approx 25\,\% - 35\,\%$). In Eq. 3.79 the energy change and the average momentum are given by

$$\Delta E = \Omega + \frac{q^2 - 2\mathbf{q}\cdot\langle \boldsymbol{k}\rangle}{2M}, \tag{3.80}$$

$$\langle \boldsymbol{k}\rangle = \frac{1}{\tau_b - \tau_a}\int_{\tau_a}^{\tau_b} \mathrm{d}\tau\, \boldsymbol{k}(\tau). \tag{3.81}$$

With this knowledge we can write down the acceptance ratio

$$R_{n\to n+1} = \frac{u_{n\to n-1}}{u_{n-1\to n}}\frac{2\alpha\Omega\Delta\tau}{\pi}\exp\left\{\left(qp_0 + \mathbf{q}\cdot\langle\boldsymbol{k}\rangle\right)\frac{\tau_b - \tau_a}{M}\right\}, \tag{3.82}$$

$$\frac{u_{n\to n-1}}{u_{n-1\to n}} = \begin{cases} \frac{2n+1}{n+1}, & \text{for bare DMC} \\ \frac{2n-1}{n} & \text{for self-energy DMC} \end{cases}. \tag{3.83}$$

The difference between the bare and the self-energy DMC comes from the different number of vertices, which will be discussed in Section 3.7. At last, one needs to iterate over all electron propagators between τ_a and τ_b to readjust the electron momenta at each vertex

$$\boldsymbol{k}_i' = \boldsymbol{k}_i - \mathbf{q}. \tag{3.84}$$

Remove phonon

The inverse of the *add-phonon* update can be held very basic. Select at random one of the n phonon propagators and remove it. Here the diagram weights are exactly the inverse of the add update. The acceptance probability is

$$R_{n\to n-1} = \frac{u_{n\to n-1}}{u_{n-1\to n}}\frac{\pi}{2\alpha\Omega\Delta\tau}\exp\left\{-\left(qp_0 + \mathbf{q}\cdot\langle\boldsymbol{k}\rangle\right)\frac{\tau_b - \tau_a}{M}\right\}, \tag{3.85}$$

$$\frac{u_{n\to n-1}}{u_{n-1\to n}} = \begin{cases} \frac{n}{2n-1}, & \text{for bare DMC} \\ \frac{n-1}{2n-3} & \text{for self-energy DMC} \end{cases}. \tag{3.86}$$

Conceptually the *remove-phonon* update is pretty simple. However, here is where the tricky details can lead to completely wrong results. For example, $\Delta\tau$ is to be understood as the duration of the polaron interval *after* after the polaron line has been removed—the original interval before the polaron has been added, so to say. Another finicky detail is the average electron momentum $\langle\boldsymbol{k}\rangle$, which is also to be taken *after* the proposed phonon propagator has been removed. The difference in the algorithm-specific constants comes also from the fact that they are taken when the phonon was added, so the orders for the remove update are reduced by one compared to Eq. 3.82.

3.7 Self-energy DMC

Before we dive into the self-energy formalism we need to formally explain the difference between the bare and the self-energy scheme. For the bare DMC procedure, one simply implements the updates that are described in Section 3.6.3 and Section 3.6.4 and applies the exact estimator for the Green's function, see Section 3.6.1. This yields a Green's function free of systematic errors, which is already an impressive result in itself. However, the diagram space is huge and thus, convergence is subpar. A way to shrink the configuration space and speed up the algorithm is by calculating only the one-particle irreducible self-energy Σ first and then—after the run has completed—applying Dyson's equation to extract the Green's function from it. To avoid convolutions—which grow as

$$\mathcal{O}\left(\prod_i n_i^2\right), \tag{3.87}$$

where n_i is the size of the input on the i^{th} axis—we apply a fast Fourier transform (FFT) instead, which has a time-complexity of only

$$\mathcal{O}\left(\prod_i n_i \sum_i \log(n_i)\right). \tag{3.88}$$

In practice, this part of the simulation completes in a few seconds and can be neglected, since the actual simulation time is most often measured rather in minutes or hours.

From here on it is understood that we always talk about the *proper* one-particle irreducible energy. In other literature, there are also mentions of the *improper* self-energy. To initiate the derivation of the Dyson equation we introduce the proper self-energy, which consists of the same diagrams as the full Green's function but with the limitation that there must not be any improper diagrams and with the start and end electron propagator removed. Improper diagrams can be cut into two separate pieces by a single straight-lined stroke, see Fig. 3.11. In simulations, this can easily be realized by keeping the count of the number of phonon lines above each vertex.
When writing down the remaining diagrams

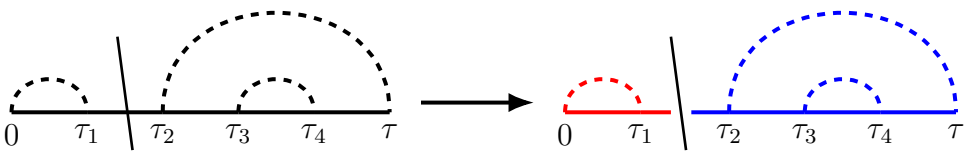

Figure 3.11: Example of an improper diagram that is excluded from the self-energy DMC calculation.

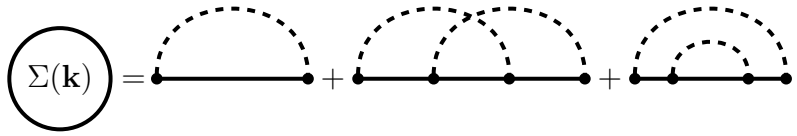

(3.89)

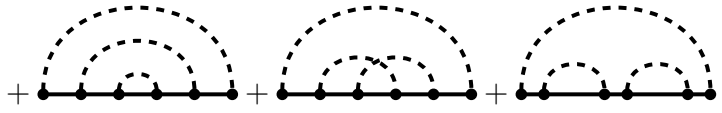

(3.90)

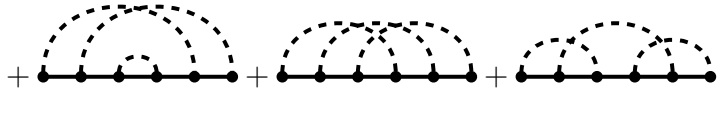

(3.91)

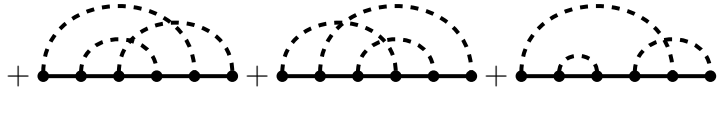

(3.92)

(3.93)

it becomes evident that the diagram space is vastly reduced, featuring now only 9 diagrams for $n = 3$ whereas for the bare case there are 15. Comparing the self-energy diagrams with the ones of the Green's function one may notice that the latter can be expressed in terms of the former by stringing multiple self-energies together:

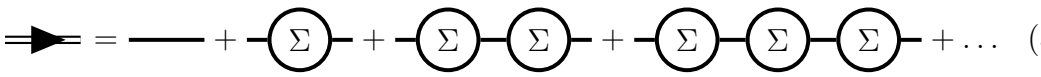

(3.94)

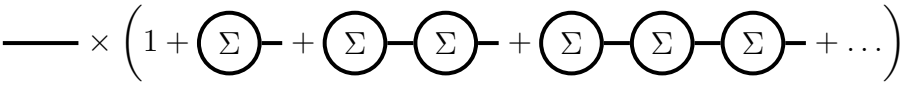

(3.95)

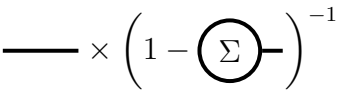

(3.96)

By inverting we arrive at the Dyson equation, the central object of this method:

$$G^{-1}(k, \omega_n, \mu) = G_0^{-1}(k, \omega_n, \mu) - \Sigma(k, \omega_n, \mu) \tag{3.97}$$

which yields the full single-particle Green's function G in terms of the bare Green's function G_0 and the self-energy Σ. It is expressed in Matsubara frequency space but the sampling during the DMC algorithm is done in imaginary time, which allows us to avoid poles that could cause numerical instabilities. It is presumed that the user is familiar with the Fourier transform. In this thesis the `fftw3` library [8] has been used for applying the numerical, discretized FFT.

The method of Fourier-transforming the self-energy into Matsubara frequency space, applying Dyson's equation and inverse-Fourier-transforming back to imaginary time still shows some problems. First, the singularity of the self-energy at $\tau = 0$

prohibits the direct application of the FT. However, since we know the singular part of the self-energy to be

$$\Sigma^{(1)}(k=0,\omega_n,\mu) = \frac{\alpha}{\sqrt{1-\mu+i\omega_j}} \tag{3.98}$$

we can do a Fourier transform of the higher-order self-energy and then add the missing first-order part back in:

$$\Sigma(k,\omega_n,\mu) = \mathcal{F}\left[\Sigma(k,\tau,\mu) - \Sigma^{(1)}(k,\tau,\mu)\right] + \Sigma^{(1)}(k,\omega_n,\mu) \tag{3.99}$$

In doing so one obtains the correct representation of $\Sigma(k,\omega_n,\mu)$. Before calculating the FT of the non-singular part of the self-energy it is beneficial to do spline interpolations—linear interpolation could cause low-frequency spikes—to boost the accuracy of the sampling. The sampling frequency can be additionally increased by setting an upper threshold β up to which the self-energy is padded with an extrapolation value of zero. In practice, the last bins of a calculation with $\tau_{\max} = 40$ will not even contain any samples, since the self-energy decays exponentially to zero. However, when doing high-α calculations one must be careful not to truncate the collection of statistics too low, as this would cause misrepresented results.

Secondly, restoring the Green's function by using the inverse Fourier transform $G(k,\omega_n) \to G(k,\tau)$ fails hopelessly. But analogously to the first problem, also here we can first deduct the zeroth-order term, perform the inverse FT and then add back the term in imaginary time-space:

$$G(k,\tau,\mu) = \mathcal{F}^{-1}\left[G(k,\omega_n,\mu) - G_0(k,\omega_n,\mu)\right] + G_0(k,\tau,\mu) \tag{3.100}$$

where the zeroth order terms are given by

$$G_0(k,\omega_n,\mu) = -\theta(\tau)e^{-(\varepsilon(k)-\mu)\tau}, \tag{3.101}$$

$$G_0(k,\omega_n,\mu) = \frac{1}{i\omega_n - \big(\varepsilon(k)-\mu\big)}. \tag{3.102}$$

In doing so, we take care of two problems: The leading singular frequencies are taken care of and the discontinuity in τ is handled correctly.

3.7.1 Exact Estimators (alternative)

Exact estimators effectively allow us to treat the $\sqrt{\tau}^{-1}$ divergence for $\tau \to 0$. However, there is another approach to this problem. Knowing that the exact first order self-energy is [11]

$$\Sigma^{(1)}(k=0,\tau) = -\frac{\alpha\sqrt{m}}{\sqrt{\pi\tau}}e^{-(\omega-\mu)\tau} \tag{3.103}$$

$$\Sigma^{(1)}(k\neq 0,\tau) = \sqrt{\frac{2}{\pi}}\frac{\alpha m}{p\tau}e^{-(\omega-\mu)\tau}F\left(p\sqrt{\frac{\tau}{2m}}\right) \tag{3.104}$$

where F is the Dawson function

$$F(x) = e^{-x^2} \int_0^x \mathrm{d}y\, e^{y^2} \tag{3.105}$$

one can run a DMC code to measure only the self-energy for higher-order diagrams and use these analytical equations to add the first-order term after the simulation has been completed. This has the disadvantage though that one needs to calculate the Dawson integral with common MC methods. For this work, only the approach with exact estimators has been implemented.

3.7.2 Direct estimators for E_0 and Z_0

The self-energy method requires quite a lot of steps. One has to evaluate the self-energy, perform an FFT, apply Dyson's equation and invert the FFT to obtain the Green's function, from which ground state energy E_0 and the quasi-particle weight Z_0 can be extracted. Instead of going the hard road, we will now show how to obtain direct estimators for E_0 and Z_0.

The fictitious potential μ enters the self-energy and the Green's function exclusively as an exponential factor, resulting in the relation

$$G(k, \omega, \mu) = G(k, \omega - i\mu) \tag{3.106}$$

$$\Sigma(k, \omega, \mu) = \Sigma(k, \omega - i\mu) \tag{3.107}$$

in Matsubara frequency space. We know that the Green's function has a pole at $\omega = i\mu - iE_0(k)$ and rewrite

$$G(k, \omega - i\mu) = \frac{Z_0(k)}{i\omega + \mu - E_0(k)} + G_r(k, \omega - i\mu) \tag{3.108}$$

where $G_r(k, \omega - i\mu)$ denotes the regular, non-singular part. In a real simulation we want to set μ very closely to (but slightly lower than) $E_0(k)$ such that we avoid divergences while still having sufficient convergence speeds. Thus, using Dyson's equation and setting $\mu = E_0(k)$ we obtain

$$\frac{i\omega}{Z_0(k)} = i\omega - \varepsilon(k) + E_0(k) - \Sigma(k, \omega - iE_0(k)) \tag{3.109}$$

and expand the self-energy in the limit $\omega \to 0$ to first order

$$\frac{i\omega}{Z_0(k)} = i\omega - \varepsilon(k) + E_0(k) - \Sigma(k, -iE_0(k)) - i\omega \left.\frac{\partial \Sigma(k, -i\mu)}{\partial \mu}\right|_{\mu = E_0}. \tag{3.110}$$

When separating the real and imaginary parts of the equation above one gets

$$E_0(k) = \varepsilon(k) + \Sigma(k, 0, E_0(k)) \tag{3.111}$$

$$Z_0(k) = \frac{1}{1 + A(k, E_0(k))} \tag{3.112}$$

where we have defined

$$A(k, E_0(k)) = -i\frac{\partial}{\partial\mu}\Sigma(k, -i\mu)\bigg|_{\mu=E_0(k)}. \tag{3.113}$$

Since both expressions depend only on the zeroth frequency we simply need to sample the average over time. Using these relations the estimators for $E_0(k)$ and $A(k, E_0)$ are

$$E_0(k) = \varepsilon(k) + \int_0^\infty \mathrm{d}\tau\, \Sigma(k, \tau, \mu) e^{(E_0(k)-\mu)\tau} \tag{3.114}$$

and

$$A(k, E_0(k)) = \int_0^\infty \mathrm{d}\tau\, \tau\Sigma(k, \tau, \mu) e^{(E_0(k)-\mu)\tau} \tag{3.115}$$

where we have used the derivative property of the Fourier transform to translate a derivative in the frequency domain to a multiplication of the time variable τ in the time domain [19].

3.7.3 Direct estimator for the polaron effective mass

The effective mass m_* describes the response of any kind of particle—here, the electron or polaron—to interactions. Estimating this value can be done straightforwardly by calculating the ground state energy for low values of k and then fitting the energies with the parabolic equation of a free particle

$$E_0(\mathbf{k}) = \frac{k^2}{2m_*}. \tag{3.116}$$

For low values of the coupling strength, this method can still be applied. However, for increasing coupling strength, the time it takes to converge one calculation rises significantly, rendering this method useless. Instead, we now derive a new direct estimator for the effective mass following the idea of [29]. Acting with $\nabla^2_{\mathbf{k}}$ on both sides of Eq. 3.114, taking the limit $k \to 0$ and considering the formal definition for the effective mass of the Fröhlich polaron

$$\left[\nabla^2_{\mathbf{k}} E\right]_{k=0} = \frac{3}{m_*} \tag{3.117}$$

we get

$$\left[\nabla_{\mathbf{k}}^2 E\right]_{k=0} = \left[\nabla_{\mathbf{k}}^2 \frac{k^2}{2m}\right]_{k=0} + \left[\int_0^\infty \mathrm{d}\tau\, \nabla_{\mathbf{k}}^2 \left(\Sigma(k,\tau,\mu) e^{(E_0-\mu)\tau}\right)\right]_{k=0} \tag{3.118}$$

$$\begin{aligned}\frac{3}{m_*} = \frac{3}{m} &+ \left[\int_0^\infty \mathrm{d}\tau\, \left(\nabla_{\mathbf{k}}^2 \Sigma(k,\tau,\mu)\right) e^{(E_0-\mu)\tau}\right]_{k=0} \\ &+ \left[\int_0^\infty \mathrm{d}\tau\, \Sigma(k,\tau,\mu) \nabla_{\mathbf{k}}^2 \left(e^{(E_0-\mu)\tau}\right)\right]_{k=0} \\ &+ \underbrace{2\left[\int_0^\infty \mathrm{d}\tau\, \nabla_{\mathbf{k}} \Sigma(k,\tau,\mu) \nabla_{\mathbf{k}} \left(e^{(E_0-\mu)\tau}\right)\right]_{k=0}}_{=0}\end{aligned} \tag{3.119}$$

$$\begin{aligned}\frac{3}{m_*} = \frac{3}{m} &+ \left[\int_0^\infty \mathrm{d}\tau\, \left(\nabla_{\mathbf{k}}^2 \Sigma(k,\tau,\mu)\right) e^{(E_0-\mu)\tau}\right]_{k=0} \\ &+ \left[\int_0^\infty \mathrm{d}\tau\, \Sigma(k,\tau,\mu) \nabla_{\mathbf{k}}^2 \left(e^{(E_0-\mu)\tau}\right)\right]_{k=0} \\ &+ \underbrace{2\left[\int_0^\infty \mathrm{d}\tau\, \nabla_{\mathbf{k}} \Sigma(k,\tau,\mu) \nabla_{\mathbf{k}} \left(e^{(E_0-\mu)\tau}\right)\right]_{k=0}}_{=0}\end{aligned} \tag{3.120}$$

$$\begin{aligned}\frac{3}{m_*} = \frac{3}{m} &+ \int_0^\infty \mathrm{d}\tau\, \left[\nabla_{\mathbf{k}}^2 \Sigma(k,\tau,\mu)\right]_{k=0} e^{(E_0(k=0)-\mu)\tau} \\ &+ \underbrace{\left(\nabla_{\mathbf{k}}^2 E_0\right)}_{=\frac{3}{m_*}} \underbrace{\left[\int_0^\infty \mathrm{d}\tau\, \Sigma(k,\tau,\mu) e^{(E_0-\mu)\tau}\right]_{k=0}}_{=A(k=0)}\end{aligned} \tag{3.121}$$

$$\Rightarrow \frac{1+A(k=0)}{m_*} = \frac{1}{m} + \underbrace{\frac{1}{3}\int_0^\infty \mathrm{d}\tau\, \left[\nabla_{\mathbf{k}}^2 \Sigma(k,\tau,\mu\right]_{k=0} e^{(E_0(k=0)-\mu)\tau}}_{=B_0} \tag{3.122}$$

where we have defined the new estimator B_0. The only term left to calculate analytically is the Laplace operator acting on the self-energy. Assuming a general self-energy diagram of the form

$$\mathcal{D}_\nu = c \prod_{i=1}^{2n-1} G_0(\Delta\tau_i, k_i, \mu) \tag{3.123}$$

$$= c e^{-\sum_{i=1}^{2n-1} \frac{\mathbf{k}_i^2}{2} \Delta\tau_i} \tag{3.124}$$

$$= c e^{f(\{\mathbf{k}_i(\mathbf{k})\})} \tag{3.125}$$

where c contains all terms that do not depend on $\mathbf{k}$. Taking the first and second derivatives of $f(\{\mathbf{k}_i(\mathbf{k})\})$ with respect to a general coordinate

$$\frac{\partial}{\partial k_\beta} f(\{\mathbf{k}_i(\mathbf{k})\}) = -\sum_{i=1}^{2n-1} \Delta\tau_i \underbrace{\frac{\partial \varepsilon(\mathbf{k}_i(\mathbf{k}))}{\partial k_\beta}}_{=\frac{k_{i,\beta}}{m}} \tag{3.126}$$

$$= -\frac{1}{m}\sum_{i=1}^{2n-1} \Delta\tau_i k_{i,\beta} \tag{3.127}$$

$$= -\frac{\tau}{m}\langle k_\beta \rangle \tag{3.128}$$

$$\frac{\partial^2}{\partial k_\beta^2} f(\{\mathbf{k}_i(\mathbf{k})\}) = -\frac{1}{m}\frac{\partial}{\partial k_\beta}\sum_{i=1}^{2n-1} \Delta\tau_i k_{i,\beta} \tag{3.129}$$

$$= -\frac{1}{m}\sum_{i=1}^{2n-1} \Delta\tau_i \frac{\partial}{\partial k_\beta} k_{i,\beta} \tag{3.130}$$

$$= -\frac{\tau}{m} \tag{3.131}$$

we can write

$$\frac{\partial^2}{\partial k_\beta^2}\mathcal{D}_\nu = c e^{f(\{\mathbf{k}_i(\mathbf{k})\})}\left[\left(\frac{\partial}{\partial k_\beta} f(\{\mathbf{k}_i(\mathbf{k})\})\right)^2 + \frac{\partial^2}{\partial k_\beta^2} f(\{\mathbf{k}_i(\mathbf{k})\})\right] \tag{3.132}$$

$$= \tag{3.133}$$

$$= \mathcal{D}_\nu\left[\left(\frac{\tau}{m}\langle k_\beta\rangle\right)^2 - \frac{\tau}{m}\right] \tag{3.134}$$

$$\nabla_{\mathbf{k}}^2 \mathcal{D}_\nu = \mathcal{D}_\nu\left(\frac{\tau^2}{m^2}\langle k\rangle^2 - 3\frac{\tau}{m}\right). \tag{3.135}$$

This enables the computation of the effective mass directly for just one $k = 0$ run. Compared to the fitting method this provides a significant performance boost since the number of MC steps required to acquire a meaningful result is only a fraction. Another positive side effect is the reliable error bars we get from the Jackknife resampling (see Section 3.5) with direct estimators.

3.7.4 Multi-energy estimation

The result from the direct estimators discussed in the previous section is heavily dependent on the chosen initial estimate of the energy. We cannot guarantee that the input lies anywhere near the exact energy. However, if we evaluate many estimates simultaneously, we can plot the input energies against the output energies. This renders every direct estimator as a function depending explicitly on the input energy

estimate, i.e. $E_0 = E_0(E_{\text{in}}), A = A(E_{\text{in}}), B_0 = B_0(E_{\text{in}})$. We can then interpolate the values and obtain a very good approximation of the ground state energy by finding the intersection of the plotted function with the identity line, as visualized in Fig. 3.12 [11]. The values of A and B_0 can then be estimated by analogously interpolating the values on the same dense grid as the energy and returning the value that corresponds to the same position on the dense grid. The same principle applies to the errors obtained from the statistical error analysis for every result. We

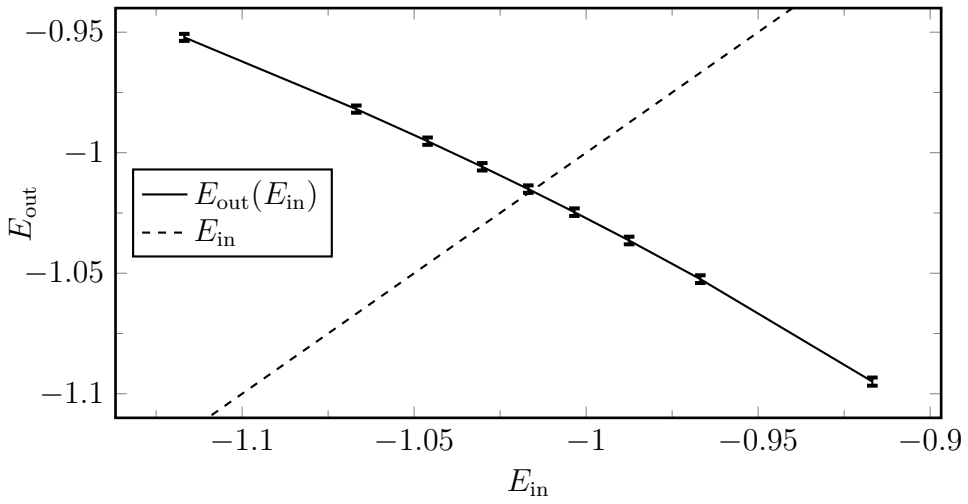

Figure 3.12: Energy estimation for the self-energy DMC in imaginary time with the multi-energy approach.

therefore construct input energies according to a symmetric power grid g_{pow} with scaling factor c and size N on $[a, b]$ defined by

$$g_{\text{pow}}(i) = \begin{cases} a + \Delta \left(\frac{N}{2}\right)^{-c} \cdot i^c & \text{if } i \leq \frac{N}{2} \\ b - \Delta \left(\frac{N}{2}\right)^{-c} \cdot (N - i - 1)^c & \text{else} \end{cases} \tag{3.136}$$

where Δ defines the midpoint E_{guess} of the grid such that $E_{\text{guess}} = a + \Delta = b - \Delta$. The energy spread is then described by Δ and defines the observed energy spectrum to be $[E_{\text{guess}} - \Delta, E_{\text{guess}} + \Delta]$.

3.8 Results

The self-energy DMC procedure that has been explained in the previous sections is now employed to calculate the dispersion relation $E_0(k)$ alongside $Z_0(k)$, the relations $E_0(\alpha)$ and $Z_0(\alpha)$, estimations of the critical wave vector $k_c(\alpha, p)$ and the effective mass m_* and various convergence experiments. In all calculations the self-energy DMC method and natural units are used, i.e. $m = \hbar = \omega = 1$. The initial estimates of the energy are extracted from the fit of the Green's function $G(\tau)$ according to Eq. 1.162. These *input* estimates are utilized by the direct estimators of E_0, Z_0 and

m_* as introduced in Eq. 3.114, Eq. 3.112, Eq. 3.115 and Eq. 3.122. Most plots are displayed without error bars since the statistical errors are too small to be visualized.

This thesis aims to reproduce results for the three-dimensional Fröhlich polaron as presented in [30] and [24]. The implementation follows Algorithm 1 of Metropolis and Hastings but with some modifications to account for the quantum nature of the object of interest, e.g. change of the dimension of configuration space by adding/removing phonons. Additional details about the data structure of the diagram and self-energy considerations can be found in Appendix A.

3.8.1 Extracting data from one simulation

Fig. 3.13 shows two examples of how the ground state energy E_0 and the quasiparticle weight Z_0 are extracted from the self-energy DMC calculation. First, the Green's function is evaluated using Dyson's equation and the result is then fitted with the exponential function Eq. 1.162. The graphs show the Green's function for zero momentum and coupling strengths of $\alpha = 1$ and $\alpha = 5$, respectively. It is clear to see that G is decaying more rapidly for higher coupling strengths in the low-τ region. Other interesting statistics have been observed, such as the distribution of the

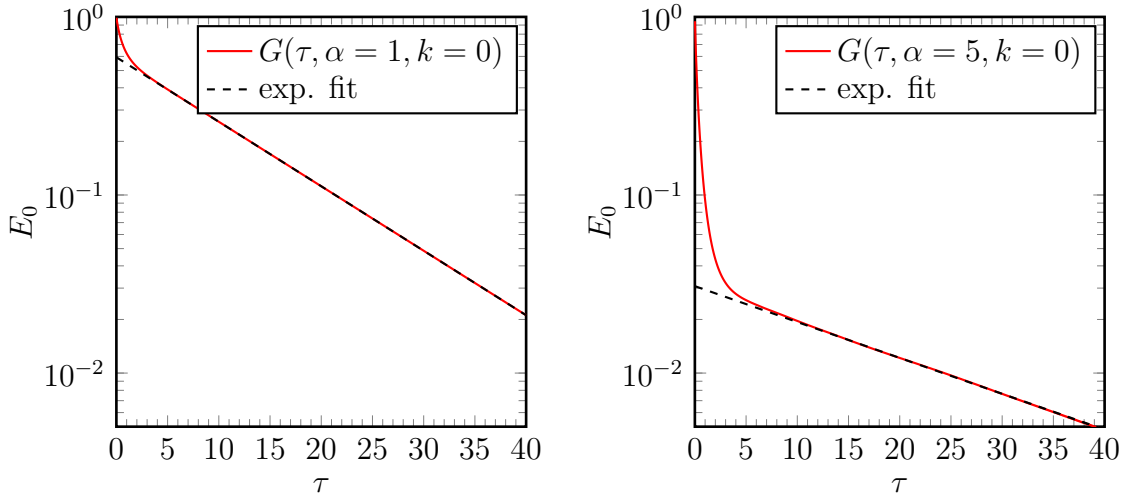

Figure 3.13: Green's function obtained from the self-energy employing the Dyson equation.

diagram order density. For higher coupling strengths, simulations tend to run slower. This is largely due to the increase in mean diagram order, which adds additional performance cost since most algorithms' time complexity grows with diagram order. The distributions for $\alpha = 1$ and $\alpha = 5$ are displayed in Fig. 3.14. For the $\alpha = 1$ run, the highest observed order is 30, while for $\alpha = 5$ it reached about 300.

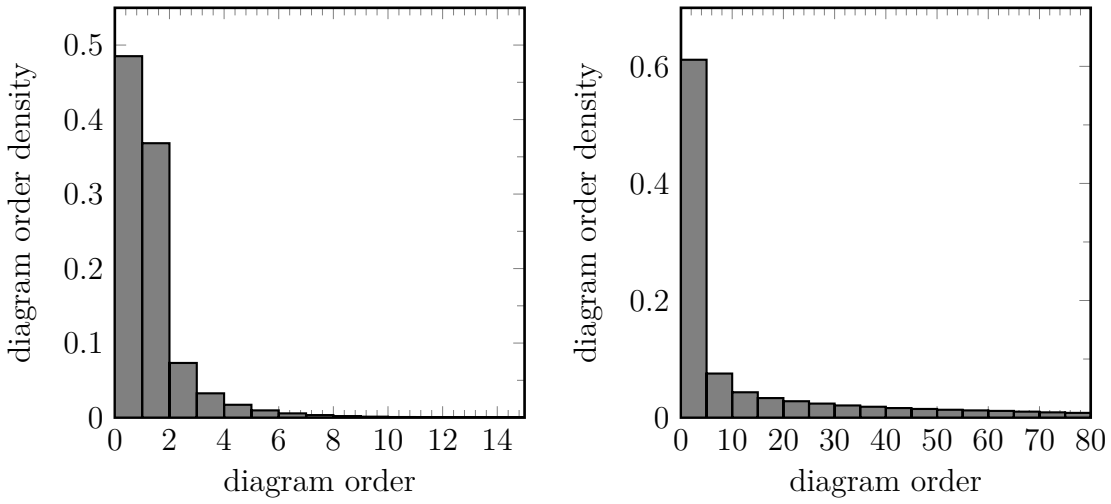

Figure 3.14: Diagram order distribution after a converged DMC run for $\alpha = 1$ (left) and $\alpha = 5$ (right). The increase in mean diagram order results in slower update speeds and, thus, slower convergence speeds in general.

3.8.2 Relations for E_0 and Z_0

For the ground state energy $E_0(k, \alpha)$ and the quasiparticle weight $Z_0(k, \alpha)$ a series of calculations needs to be carried out. For this, a Python wrapper has been implemented to automatically configure and execute all needed calculations for both the momentum and coupling strength relations. Input energies need to be in a certain vicinity around the exact value to obtain reliable results. In a first calibration run, we obtain the energies as described in Section 3.8.1—by fitting the Green's function—and use the result as input parameters for the direct estimators during the second run. In doing so we obtain good guesses for the energies of each run and can therefore reduce the energy spread Δ to increase the accuracy of the interpolation.

The dispersion relation has been calculated for $\alpha \in \{0, 1, 3, 5\}$, displayed in Fig. 3.15. Each data point in the plot refers to a single simulation, each of which has been run for $n_{\alpha=0} = 1.5 \times 10^8$, $n_{\alpha=1} = 1.5 \times 10^8$, $n_{\alpha=3} = 8.4 \times 10^{10}$ and $n_{\alpha=5} = 2.53 \times 10^{11}$ elementary MC steps. As can be seen in Fig. 3.16, the first and second-order perturbation expansions of the ground state energy agree for low k values with the obtained results. The polaron dispersion $E(k)$ is strictly increasing on $[0, k_c(\alpha)]$, where $k_c(\alpha)$ represents the critical momentum. For $k \to k_c(\alpha)$ the system goes over to the so-called continuum edge

$$E_c(\alpha) = E_0(0, \alpha) + \hbar\omega, \tag{3.137}$$

which, in our case of $\hbar = \omega = 1$, means that we have

$$E_c(\alpha) = E_0(0, \alpha) + 1 \tag{3.138}$$

and we can translate the energy dispersion by $E_0(0, \alpha)$ such that we only observe

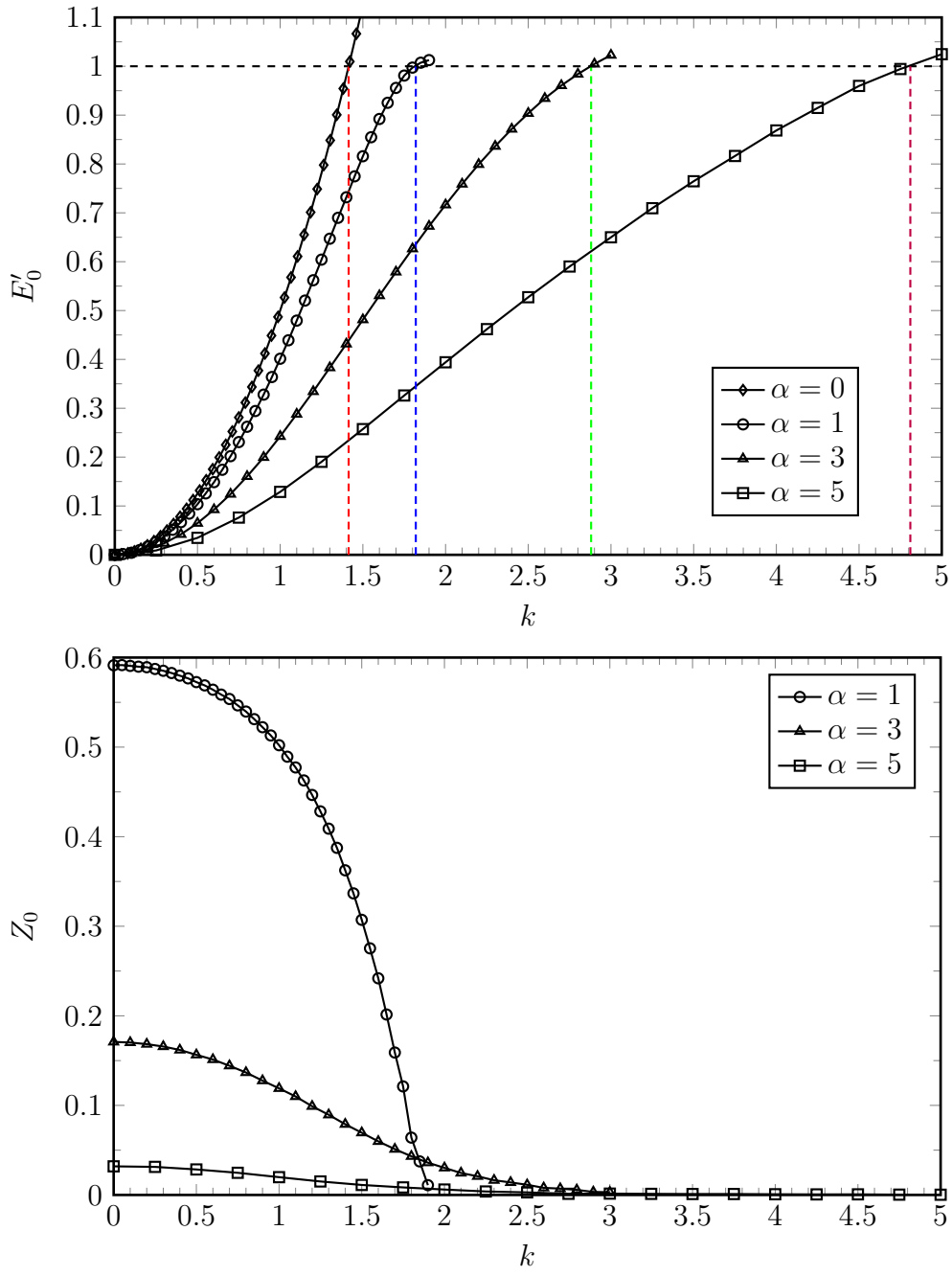

Figure 3.15: Continuum edge wave vector approximations for various values of α. The energy values have been shifted according to $E_0'(\alpha, k) = E_0(\alpha, k) - E_0(\alpha, 0)$. The horizontal dotted line represents the continuum edge while the vertical ones are the estimated values of $k_c(\alpha)$. Values for $Z_0(\alpha = 0, k)$ are not displayed since it is just unity for all values of k.

energy differences

$$\Delta E_0(k, \alpha) \equiv E_0(k, \alpha) - E_0(0, \alpha) \tag{3.139}$$

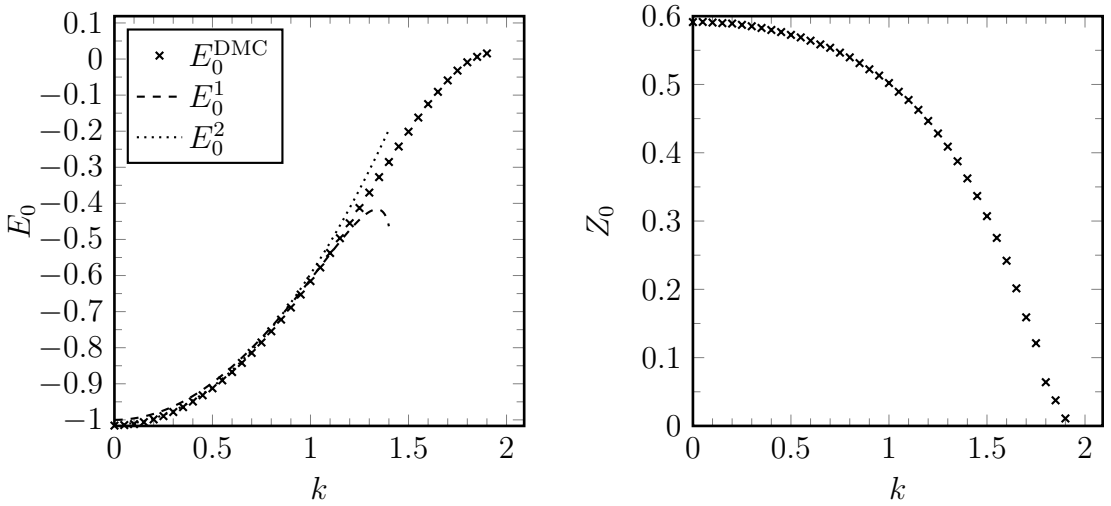

Figure 3.16: Ground state energy E_0 and quasiparticle weight Z_0 as a function of the momentum k. The dots are the data from the DMC calculations. The error bars are not visible due to the low uncertainty.

For the 3D case the dispersion curve crosses the continuum edge at a finite value, the critical wave vector $k_c(\alpha)$ [13]. From this we can estimate $k_c(\alpha)$ by finding the intersection of $\Delta E_0(k, \alpha)$ with $\hbar\omega$, as demonstrated in Fig. 3.15. The values obtained for the critical values are $k_c(0) \approx 1.4143, k_c(1) \approx 1.82, k_c(3) = 2.88$ and $k_c(5) = 4.81$. Our results agree to great extent with the values presented in [13]. The differences arise from the finite number of points that have been calculated and the fact that near the continuum edge our model begins to break down.

Up to the first order in α the critical wave vector can be approximated by

$$k_c(\alpha) = \sqrt{2} + \left(\frac{\pi}{2} - 1\right) \frac{\alpha}{\sqrt{2}} + O(\alpha^2) \tag{3.140}$$

which predicts a lower bound of

$$\lim_{\alpha \to 0} k_c(\alpha) = \sqrt{2}. \tag{3.141}$$

This agrees with the interaction free ($\alpha = 0, m_{\mathrm{eff}}$) case where

$$E_0(\alpha = 0, k_c) = \frac{k_c^2}{2} = 1. \tag{3.142}$$

It has to be noted that near the continuum edge the results of this model should only be taken as an estimate, especially for high α values. For $\alpha = 0$, we get a precise result of $\sqrt{2}$ up to the fourth decimal place.

The ground state energy E_0 and quasiparticle residue Z_0 in dependence of the coupling strength α have been calculated for values up to $\alpha = 8$. For higher values the Fröhlich, approximation without external phonons is not valid anymore. The obtained results are displayed in Fig. 3.17 and agree with values from [24].

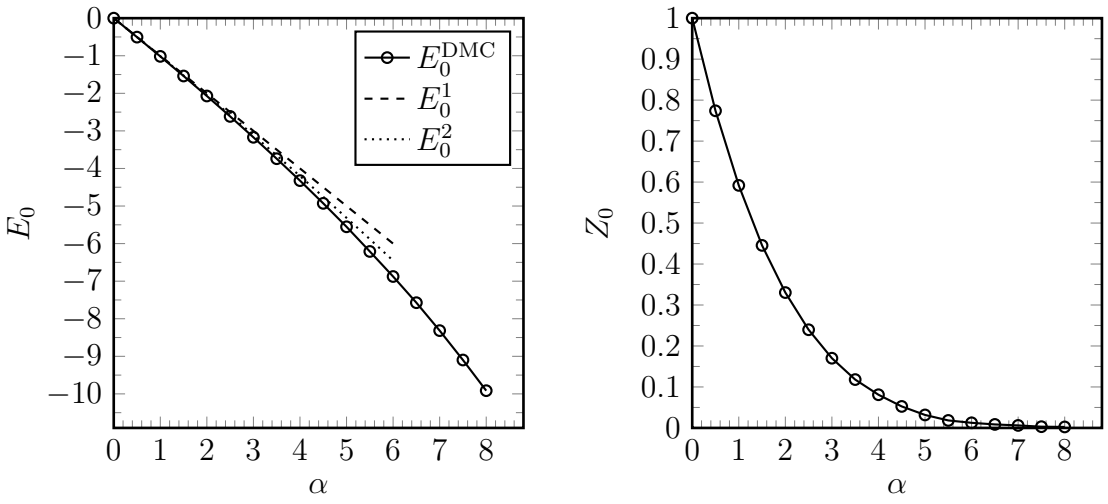

Figure 3.17: Ground state energy E_0 and quasiparticle weight Z_0 as a function of the coupling strength α. The dots are the data from the DMC calculations, which have been connected to aid in visibility. The dashed and dotted lines represent the first and second order approximations to the energy. The error bars are not visible due to the low uncertainty.

3.8.3 Effective mass

The simulations for the effective mass have been carried out on $\alpha \in [0, 8]$. In Fig. 3.18 the results are compared to the values of Feynman's analytical values [31]. For low

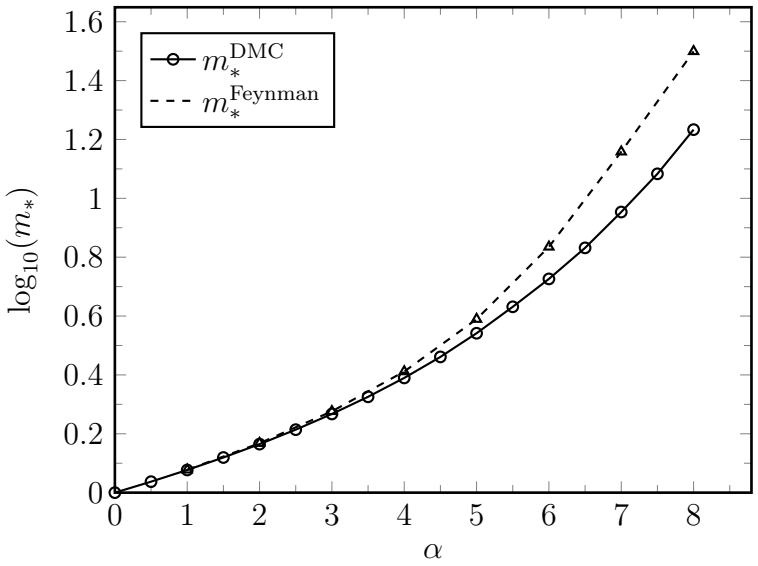

Figure 3.18: Effective mass as a function of the coupling strength. Feynman's approximation yields accurate results for low α but overestimates m_* for higher values of the coupling strength.

coupling strengths, Feynman's results are very good approximations. However, for $\alpha > 5$ it significantly overestimates the effective mass and the DMC approach should be used. Our findings have reproduced the results of [24] and [12] for values of $\alpha < 5.5$ to a good extent. As mentioned before, for higher coupling stengths our model lacks certain modifications to produce accurate results.

The effective mass estimator seems to be less susceptible to errors in the input energies than the energy or quasi-particle residue, see Fig. 3.19. However, this is

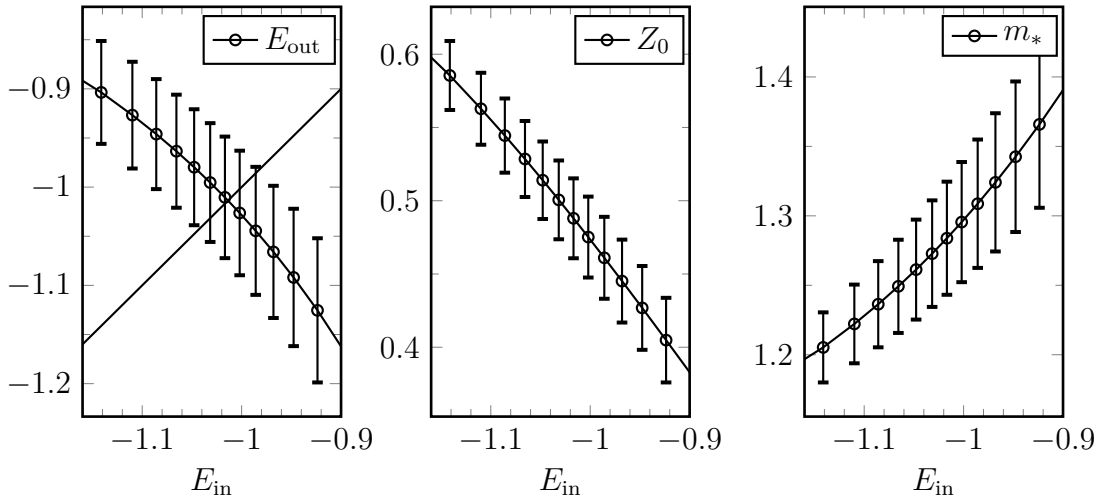

Figure 3.19: Comparison of the susceptibility of E_0, Z_0 and m_* with respect to the input energy estimates for $k = 0$, $\alpha = 1$. To make the errors visible only $M = 1000$ DMC measurements have been performed. With $E_0 = -1.014$, $Z_0 = 0.50$, $m_* = 1.29$ the results are—even with only 1000 measurements—already accurate to the second significant digit when compared to the converged results.

not correlated with convergence speed. It is not clear if any of the direct estimators converges faster than the others. Nevertheless, in Appendix B a convergence test is shown, where the dependency of these estimators is plotted against the allowed maximum order of the diagram. One must not mistake this for the time evolution of the estimators during the simulation.

3.8.4 Error estimation from direct estimators

We have mentioned that simple linear interpolation suffices for calculating the locus of the intersection of $E_{\text{out}}(E_{\text{in}})$ and the unity line. In Fig. 3.19 we can see that despite the smooth appearance of the output values, the error bars are significant, because the values of individual points are correlated [11]. This is supported by Fig. 3.20, which shows calculations for $\alpha \in \{3, 5, 6\}$, for values of μ close to the true energy and a somewhat more careful guess. The error has been propagated onto the intersection locus. The obtained values of the energy should be independent of the chosen value of μ. This statement is reinforced by the fact that the respective results lie within

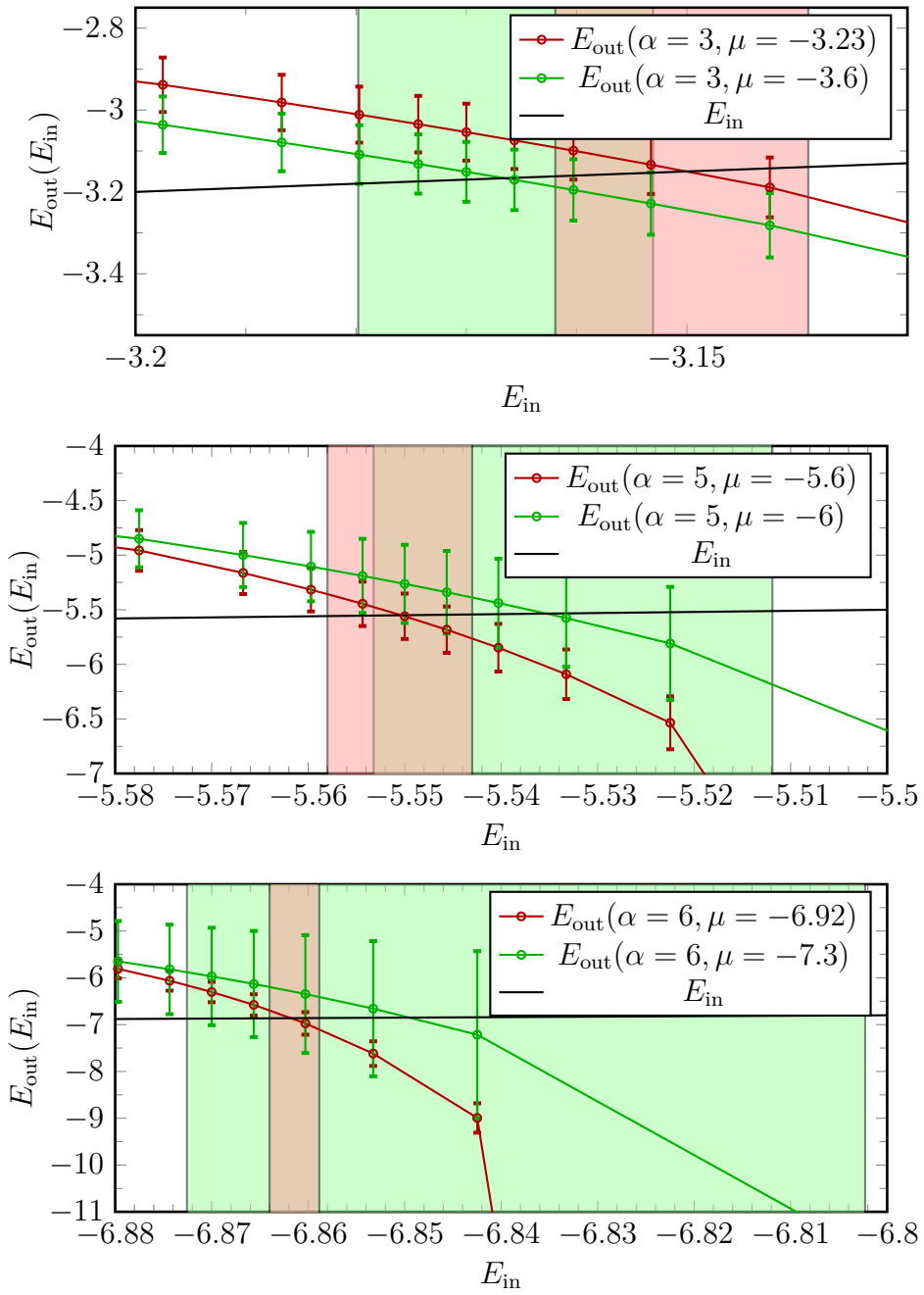

Figure 3.20: We compare runs of different coupling strengths and μ. The slower convergence for a lower μ is especially easy to notice for larger α values. For all calculations only a total of 2×10^4 measurements were performed to make the error bars visible. However, to sample the global average and not only some local states, between each measurement 2×10^4 elementary DMC updates were applied. The shaded regions are the propagated errors to the intersection point.

each others error margin. However, for values of μ far below the true ground state energy the error converges much slower than with more pricise guesses. This is due to the fact that longer τ values are sampled before the self-energy vanishes [11].

Chapter 4

Conclusion and Outlook

This thesis' goal was to investigate the properties of the Fröhlich polaron in its harmonic approximation. This was done by building a Diagrammatic Quantum Monte Carlo algorithm with which ground state energies, quasi-particle residues, self-energies and the reconstructed Green's functions can be calculated. The vanilla DMC code for the Fröhlich polaron was extended to the self-energy case, which significantly reduces the configuration space of the diagrams. This leads to faster convergence and increased efficiency of the updates. Using the outputs of the DMC program we set up simulations for calculating dispersion relations for various values of the coupling strength, the relations $E_0(\alpha)$ and $Z_0(\alpha)$ for $k = 0$, some convergence tests and estimations of the critical wave vector $k_c(\alpha)$ and the effective mass m_*.

A short introduction into quantum field theory and polaron physics—especially concentrating on the Fröhlich polaron—has been given, featuring the Green's function formalism and Wick's theorem. These prominent mechanisms enabled the translation of Green's functions to graphical diagrams. After the basic idea of Monte Carlo simulations had been laid out, both these tools were combined to form the basis of the Diagrammatic Quantum Monte Carlo formalism, where the self-energy diagram was revealed to be the object of interest. Focus has been set on detailed explanations of the DMC updates and derivations of acceptance rates and exact/direct estimators, to provide a guide on how to construct a DMC program. After the results had been presented and discussed, technical difficulties and implementation details were given.

Overall, the results obtained from this thesis coincide with previous work. Error estimation was done by employing jackknife resampling. However, the errors have converged surprisingly quickly for some calculations. The direct estimator for the effective mass of the self-energy formalism has been relatively new. Albeit most of the simulations have proven successful, some limits of the harmonic, one-electron Green's function approach have been discovered throughout this thesis. The results for low α values provide very accurate estimations with negligible systematic errors. For high values of the coupling strength—i.e. $\alpha > 5$—our approach breaks down and one has to modify the Fröhlich Hamiltonian to account for lattice effects. However, most materials fall into the $\alpha \in [0, 5]$ range, which renders high-coupling coupling simulations less relevant for the real world. This work is based on the theory of

the harmonic approximation of the Fröhlich polaron. Anharmonic terms, where the electron interacts with more than one phonon simultaneously, may further improve the accuracy of DMC calculations. The mentioned approximations also lead to uncontrollable errors near and after the continuum edge. Future work may build upon this thesis and improve the DMC algorithm by including higher order terms in the Hamiltonian.

Bibliography

[1] Jozef T. Devreese (auth.) Alexandre S. Alexandrov. *Advances in Polaron Physics*. 1st ed. Springer Series in Solid-State Sciences 159. Springer, 2010. ISBN: 9783642018954; 3642018955; 9783642018961; 3642018963.

[2] Alexander Altland and Ben D. Simons. *Condensed Matter Field Theory*. 2nd ed. Cambridge University Press, 2010. DOI: 10.1017/CBO9780511789984.

[3] Neil S. Ostlund Attila Szabo. *Modern Quantum Chemistry: Introduction to Advanced Electronic Structure Theory*. Dover Publications, 1996. ISBN: 9780486691862; 0486691861.

[4] Franco Bassani and Emmanuel Rashba. "Polarons". In: *Encyclopedia of condensed matter physics*. Elsevier, 2005, pp. 347–355.

[5] Emil Blomquist. "A Monte Carlo Approach to Feynman Diagrammatic Series and its Boldification". PhD thesis. 2017.

[6] Max Born. "Quantenmechanik der StoSSvorgänge". In: *Zeitschrift fur Physik* 38.11-12 (Nov. 1926), pp. 803–827. DOI: 10.1007/BF01397184.

[7] Alexander L. Fetter and John Dirk Walecka. *Quantum theory of many-particle systems*. Dover, 2003.

[8] M. Frigo and S.G. Johnson. "The Design and Implementation of FFTW3". In: *Proceedings of the IEEE* 93.2 (Feb. 2005), pp. 216–231. DOI: 10.1109/jproc.2004.840301. URL: https://doi.org/10.1109/jproc.2004.840301.

[9] H. Fröhlich. "Electrons in lattice fields". In: *Advances in Physics* 3.11 (1954), pp. 325–361. DOI: 10.1080/00018735400101213. eprint: https://doi.org/10.1080/00018735400101213. URL: https://doi.org/10.1080/00018735400101213.

[10] Murray Gell-Mann and Francis Low. "Bound States in Quantum Field Theory". In: *Physical Review* 84.2 (Oct. 1951), pp. 350–354. DOI: 10.1103/physrev.84.350. URL: https://doi.org/10.1103/physrev.84.350.

[11] Jonas Greitemann and Lode Pollet. "Lecture notes on Diagrammatic Monte Carlo for the Fröhlich polaron". In: (2017). DOI: 10.48550/ARXIV.1711.03044. URL: https://arxiv.org/abs/1711.03044.

[12] Thomas Hahn. "Diagrammatic Quantum Monte Carlo for the Fröhlich polaron". en. In: (2017). DOI: 10.25365/THESIS.49106. URL: https://othes.univie.ac.at/49106/.

[13] Thomas Hahn et al. "Diagrammatic Monte Carlo study of Fröhlich polaron dispersion in two and three dimensions". In: *Physical Review B* 97 (Apr. 2018). DOI: 10.1103/PhysRevB.97.134305.

[14] H Haken. *Quantenfeldtheorie des Festkörpers*. German. OCLC: 958576855. Vieweg+Teubner Verlag, 2013. ISBN: 9783322966940.

[15] W. K. Hastings. "Monte Carlo sampling methods using Markov chains and their applications". In: *Biometrika* 57.1 (1970), pp. 97–109. DOI: 10.1093/biomet/57.1.97.

[16] T Holstein. "Studies of polaron motion". en. In: *Annals of Physics* 8.3 (Nov. 1959), pp. 325–342. ISSN: 00034916. DOI: 10.1016/0003-4916(59)90002-8. URL: https://linkinghub.elsevier.com/retrieve/pii/0003491659900028 (visited on 05/24/2021).

[17] "IEEE Standard for Floating-Point Arithmetic". In: *IEEE Std 754-2019 (Revision of IEEE 754-2008)* (2019), pp. 1–84. DOI: 10.1109/IEEESTD.2019.8766229.

[18] Gerald D. Mahan. *Many-Particle Physics*. Springer US, 2000. DOI: 10.1007/978-1-4757-5714-9. URL: https://doi.org/10.1007/978-1-4757-5714-9.

[19] Dominic Marchand. "Polaron physics beyond the Holstein model". PhD thesis. University of British Columbia, 2011, pp. 7–13.

[20] Richard Martin. *Electronic Structure of Condensed Matter*. University Lecture. 2004. URL: https://courses.physics.illinois.edu/phys598SCM/fa2004/lecture_notes/lect18a-2ndQ.pdf.

[21] Richard D. Mattuck. *A guide to Feynman diagrams in the many-body problem*. Dover Publications, 2013.

[22] Nicholas Metropolis. "The Beginning of the Monte Carlo Method". In: *Los Alamos Science* 15 (1987), pp. 125–130.

[23] Nicholas Metropolis et al. "Equation of state calculations by Fast Computing Machines". In: (1953). DOI: 10.2172/4390578.

[24] A. S. Mishchenko et al. "Diagrammatic quantum Monte Carlo study of the Fröhlich polaron". In: *Phys. Rev. B* 62 (10 Sept. 2000), pp. 6317–6336. DOI: 10.1103/PhysRevB.62.6317. URL: https://link.aps.org/doi/10.1103/PhysRevB.62.6317.

[25] Yuli V. Nazarov and Jeroen Danon. *Advanced Quantum Mechanics: A Practical Guide*. Cambridge University Press, 2013. DOI: 10.1017/CBO9780511980428.

[26] Wolfgang Nolting. *Grundkurs theoretische Physik 7 Viel-Teilchen-Theorie*. Springer Berlin, 2016.

[27] Eva Pavarini et al. *Many-Body Methods for Real Materials.* Aug. 2019, pp. 421–448. ISBN: ISBN 978-3-95806-400-3.

[28] S. I. Pekar. *Research in Electron Theory of Crystals* -. U. S. Atomic Energy Commission, Division of Technical Information, 1963.

[29] N. V. Prokof'ev and B. V. Svistunov. "Bold diagrammatic Monte Carlo: A generic sign-problem tolerant technique for polaron models and possibly interacting many-body problems". In: *Phys. Rev. B* 77 (12 Mar. 2008), p. 125101. DOI: 10.1103/PhysRevB.77.125101. URL: https://link.aps.org/doi/10.1103/PhysRevB.77.125101.

[30] Nikolai V. Prokof'ev and Boris V. Svistunov. "Polaron Problem by Diagrammatic Quantum Monte Carlo". In: *Phys. Rev. Lett.* 81 (12 Sept. 1998), pp. 2514–2517. DOI: 10.1103/PhysRevLett.81.2514. URL: https://link.aps.org/doi/10.1103/PhysRevLett.81.2514.

[31] R. Rosenfelder and A.W. Schreiber. "On the best quadratic approximation in Feynman's path integral treatment of the polaron". In: *Physics Letters A* 284.2 (2001), pp. 63–71. ISSN: 0375-9601. DOI: https://doi.org/10.1016/S0375-9601(01)00287-0. URL: https://www.sciencedirect.com/science/article/pii/S0375960101002870.

[32] Jun Shao and Dongsheng Tu. *The jackknife and Bootstrap*. Springer, 1996.

[33] Andreas Tröster. *Lecture notes in Advanced Computational Physics*. 2022.

[34] Kris Van Houcke et al. "Diagrammatic Monte Carlo". In: *Physics Procedia* 6 (2010), pp. 95–105. DOI: 10.1016/j.phpro.2010.09.034.

Appendix A

Implementation Details

A.1 Data Structure

Some of the updates introduced in Section 3.6.3 and Section 3.6.4 modify the diagram only locally while others make changes to the whole diagram. For the latter kind, it is practically unnecessary to optimize the design of the diagram in memory since these updates scale as $\mathcal{O}(n)$ where n is the order of the diagram. For local updates, however, one needs to pay attention to the data structure of the diagram as it is crucial to the efficiency of these updates. Let's examine the *remove-phonon* update as an example. To calculate the mean momentum $\langle \boldsymbol{k} \rangle$ the diagram propagators/vertices need to be logically linked. This suggests that we choose a list-like structure for storing the vertices. However, selecting a vertex to remove might prove difficult as one needs random access to the diagram vertices. This property can be emulated by first proposing an index $i \in U(0, 2n-1)$ and iterating to the i-th vertex in the list. It should be clear that this procedure is highly inefficient for high n. Another well-known data structure that provides random access is a contiguously stored array, e.g. a vector. However, when removing vertices we end up with *holes* in memory where the removed vertices used to be. To get rid of these holes, one could periodically rebuild the vertex vector. Unfortunately, DMC algorithms are compute-bound and every minor overhead on the CPU slows down the simulation.

Thus, we need a data structure that enables us to achieve random access while retaining list-like behavior. The proposed solution is a combination of a doubly-linked list `std::list<vertex>`, which stores the actual vertex objects and a vector `std::vector<std::list<vertex>::iterator>` which holds list iterators of the objects in a non-ordered fashion. On top of that, each vertex also holds an iterator `std::vector <std::list<vertex>::iterator>::iterator` to the vector object to which it corresponds to. This way a bidirectional association is established. This approach is also described in [11]. The data structure is illustrated in Fig. A.1.

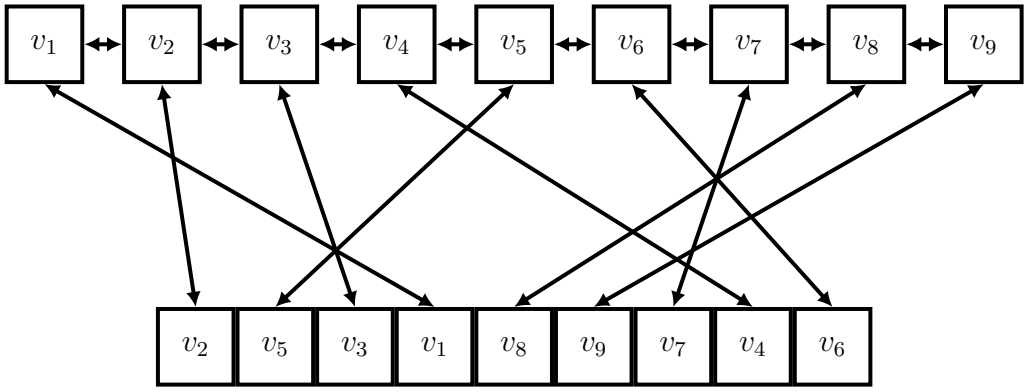

Figure A.1: Data structure for efficient DMC calculations. The top row represents the doubly-linked list of vertices while the bottom row depicts the vector of the same elements (albeit in non-deterministic order) to achieve random access. The entries in each data structure are linked to their corresponding counterparts in the other container.

A.2 Self-energy considerations

Conceptually, the Σ-DMC algorithm is the same as the bare version where the Green's function is sampled directly. However, there are still required changes for updates that need to be applied. First, the acceptance probabilities for some updates will change because of the slightly different probabilities of selecting a propagator at random. This has already been discussed for all affected updates.

A.2.1 Irreducibility

Secondly, when doing self-energy DMC simulations one must not forget to assert that the proposed diagram without the selected phonon propagator is irreducible. As already mentioned, this is possible by keeping count of the number of phonon propagators that span over each vertex $n_{\mathrm{ph},i}$. If a proposed update results in a diagram that contains a vertex with $n_{\mathrm{ph}_i} = 0$ the diagram is—by definition—one-particle reducible and the update is rejected. The only updates that may change this variable are the *remove-phonon*, *change-topology* and *add-phonon* updates. However, the *add-phonon* update can never propose a one-particle reducible diagram from an irreducible one, so this check is only necessary for the other two updates. This phonon count also aids in calculating the energy for each time interval for the *rescale-diagram* update.

Another option would be to store the momenta of the electron propagators in a hash table, which allows checking whether one of the new momenta $\boldsymbol{k}_i'$ is equal to the global momentum $\mathbf{k}$ in $\mathcal{O}(1)$. This is practically equivalent to saying that the diagram is irreducible by noting that no phonon propagator would cross over this time interval. This seems like the more efficient solution, though this introduces inaccuracy as the momenta are kept in memory in a floating-point representation

[17] which can not be compared safely without accepting a small margin of error.

Thence the former option has been implemented for this thesis, as integers can be stored accurately in memory and it provides additional benefits for other updates and statistics.

A.2.2 Fake Diagrams

In Section 3.3 we discussed how the diagrams can be normalized. However, in contrast to the direct sampling algorithm of the Green's function, self-energy DMC evaluates the self-energy, which lacks the zeroth order diagram. To keep the ability to normalize the self-energy as proposed in Section 3.3 we need to introduce so-called fake diagrams, which do not contribute to the sampling of the self-energy, but act as the discussed normalizing factor. When transitioning into a zeroth order diagram, the usual measurements (e.g. energy, Z-factor, effective mass) are not carried out. Instead, only the normalization counter is incremented. This assures that the algorithm still samples the correct distribution while retaining the aforementioned normalization method.

Appendix B

Convergence Tests for E_0 and Z_0

For the simulation, there are a few parameters that restrict the diagram space. These precautions are employed to prohibit the diagram to sample states that are the result of statistical outliers. However, these values must be chosen carefully to not introduce systematic errors. It has to be noted that the $n_{\max}$ needed for the convergence of E_0 and Z_0 does in general not guarantee the convergence of other properties. Nevertheless, we analyze the convergence of the ground state energy and the quasiparticle weight, since these are the most interesting properties for a DMC calculation.

The maximal order that may be assumed by the diagram is limited by $n_{\max}$. We carried out convergence tests for the maximal order for $\alpha = 1$, $\alpha = 3$ and $\alpha = 5$. In Fig. B.1, Fig. B.2 and Fig. B.3 the results have been visualized.

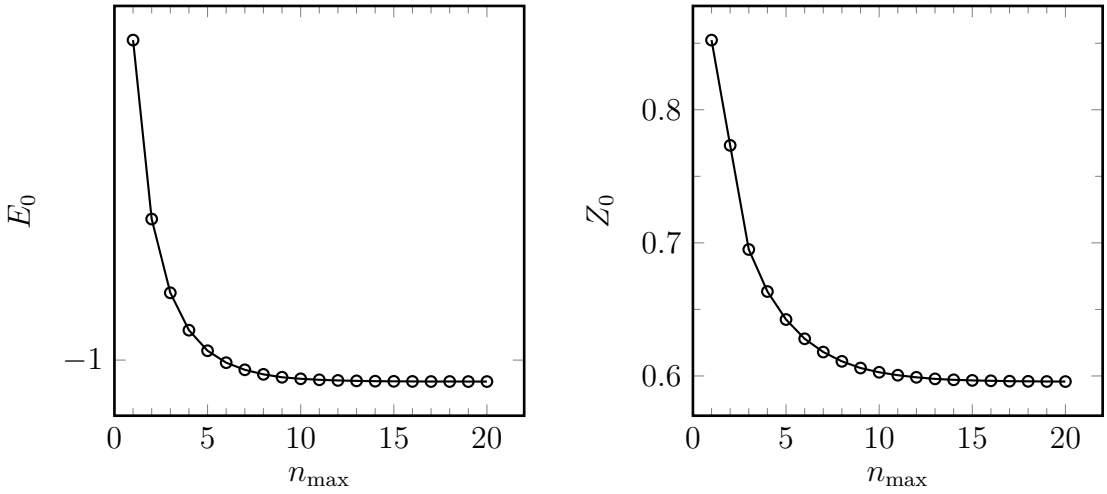

Figure B.1: Maximal order convergence test for $\alpha = 1$. The direct estimators are converged to a good approximation for $n_{\max} = 15$. Including higher order terms may only improve accuracy at the cost of additional computational resources.

For $\alpha = 1$ is is clear to see that $n_{\max} \approx 15$ already suffices to estimate the ground state energy and Z-factor accurately to a high degree. The simulation for $\alpha = 3$

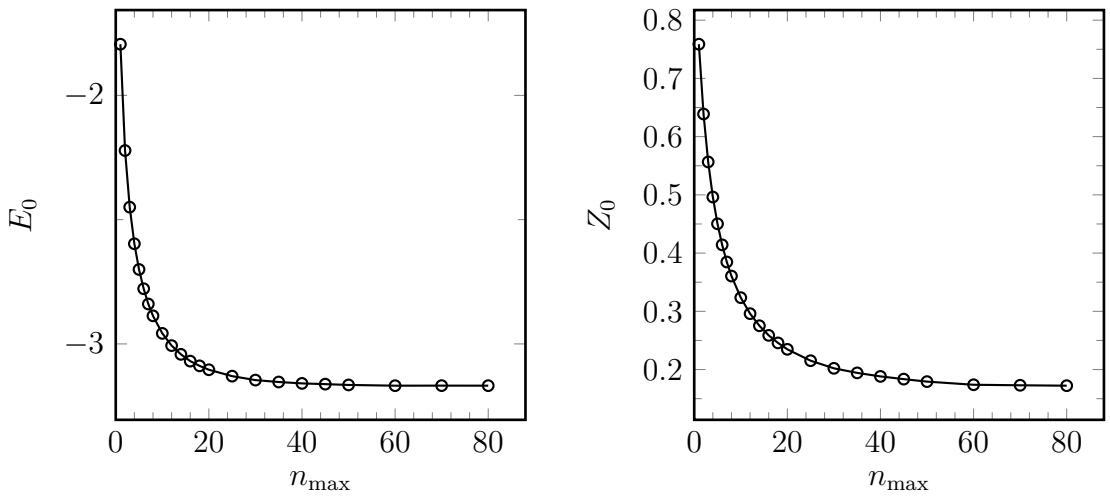

Figure B.2: Maximal order convergence test for $\alpha = 3$. We can see clearly that the estimator of the qusiparticle residue as a function of the maximum order converges slower than the energy.

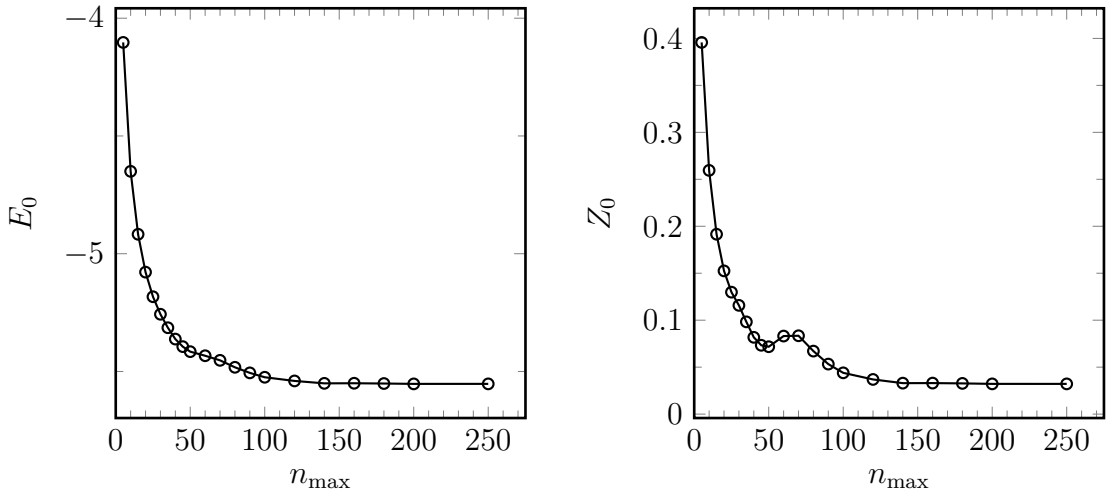

Figure B.3: Maximal order convergence test for $\alpha = 5$. The interesting local extremum at around $n_{\max} = 65$ is unexpected.

generates higher order diagrams more frequently and thus, we need at least $n_{\max} = 60$ to obtain viable results. This effect is even more pronounced for $\alpha = 5$, where we estimate $n_{\max} \approx 150$. Interestingly, we observe a local minimum of the quasi-particle residue at $n_{\max} \approx 65$.

Appendix C

Hardware

The simulations carried out in this thesis have been performed on a very modern `AMD Ryzen 9 5950X`, which features 16 cores operating at a base (boost) clock speed of 3.4 GHz (4.9 GHz) and a huge L3 cache of 64 MB, which enables that the program runs entirely on the CPU and its caches. Analyzing a run with `cachegrind`

```
==2493356== I   refs:      7,211,482,463
==2493356== I1  misses:       27,393,635
==2493356== LLi misses:           20,669
==2493356== I1  miss rate:          0.38%
==2493356== LLi miss rate:          0.00%
==2493356==
==2493356== D   refs:      2,829,551,296  (1,807,312,820 rd   + 1,022,238,476 wr)
==2493356== D1  misses:        7,974,011  (    6,117,896 rd   +     1,856,115 wr)
==2493356== LLd misses:          410,058  (       72,567 rd   +       337,491 wr)
==2493356== D1  miss rate:           0.3% (          0.3%     +           0.2%  )
==2493356== LLd miss rate:           0.0% (          0.0%     +           0.0%  )
==2493356==
==2493356== LL refs:          35,367,646  (   33,511,531 rd   +     1,856,115 wr)
==2493356== LL misses:           430,727  (       93,236 rd   +       337,491 wr)
==2493356== LL miss rate:            0.0% (          0.0%     +           0.0%  )
```

confirms that the miss rate of the first level cache is as low as 0.38 %, which means that almost the entire program can run without ever using the L2 or L3 cache. Unfortunately, `cachegrind` does not show information about the L2 cache on systems with 3 or more cache levels. It analyzes only the first and last level (LL). The L3 miss rate vanishes almost completely, with a miss rate of only 2.866×10^{-4} %. Such a level of performance is indispensable when developing HPC programs for scientific purposes and allows the simulations in this thesis to be run in minutes instead of days [5].